RICE UNIVERSITY

Methods of micromanipulating giant lipid vesicles for the studies of molecular interactions with membranes and membrane-membrane interactions

by

Yen Sun

A THESIS SUBMITTED

IN PARTIAL FULFILLMENT OF THE

REQUIREMENTS FOR THE DEGREE

Doctor of Philosophy

APPROVED, THESIS COMMITTEE

Huey W. Huang, Chair
Professor of Physics and Astronomy

Jason H. Hafner
Associate Professor
Physics and Astronomy and Chemistry

James McNew
Associate Professor
Biochemistry and Cell Biology

HOUSTON, TEXAS

APRIL 2011

Abstract

Methods of Micromanipulating Giant Lipid Vesicles for the Studies of Molecular Interactions with Membranes and Membrane-Membrane Interactions

by

Yen Sun

The lipid matrix of cell membranes is a natural binding site for amphipathic molecules. Consequently there are water-soluble, amphipathic peptides and proteins that exert their functions on membranes. Studies also showed that binding of amphipathic molecules (such as drugs) may change the functions of membrane proteins by altering the physical properties of the membrane. Thus, we want to understand how amphipathic molecules interact with membranes and find out the consequences of such membrane-molecule interactions. My thesis consists of development of new methods for studying the kinetics of molecular interactions with membranes and a series of comparative studies on different membrane-active molecules including peptides, proteins and drugs. My contribution to the methods for kinetics is to complement the equilibrium methods already developed in our lab for past twenty years. I established a micropipette aspiration system based on the system developed by Evan Evans in the 80's, but instead of measuring the elastic properties of membranes, we used it to study the dynamic interaction processes between amphipathic molecules and membranes.

In this thesis I performed four different experiments. In the first two experiments I studied the drug-membrane interactions for which biological effects have been widely reported but poorly understood. In the third experiment, we found that membrane binding may promote the formation of β-amyloid aggregates for certain peptides that might have significant implications to Alzheimer's disease and diabetes. These three systems were studied as a contrast to previous studies on antimicrobial peptides which formed transmebrane pores. The comparison of all these different membrane-binding molecules gave us a broad understanding of membrane-molecule interactions. In the fourth experiment, I modified our micropipette aspiration system to measure the free energies of adhesion and hemifusion of lipid bilayers. This method is capable of measuring the transition free energy for each step of lipid transformation during membrane fusion. This is relevant to current research on membrane fusion which focuses on how the proteins induce the lipid transformations.

Acknowledgments

I would like to thank my advisor Dr. Huey Huang for all his support and advice in these research projects. He gave me a lot of guidance during my journey through the research.

I would like to thank Dr. James McNew and Dr. Jason Hafner for agreeing to serve on my thesis committee.

I would like to thank my fellow graduate students Chang-Chun Lee, Wang-Chen Wang, Shuo Qian for their assistance and helpful discussions in the lab.

Finally, I would like to thank my husband Chang-Chun Lee and my parents for supporting me all the way.

Contents

List of Figures

List of Tables

Introduction

The goal of the thesis

Cell membranes, which separate the interior cell contents from the surrounding environment, are essential for the proper functioning and the integrity of the cell. It consists of the phospholipid bilayer with embedded proteins. Most phospholipids contain a hydrophilic phosphate head group and two hydrophobic fatty acid chains. When phospholipids are placed in water, they will self-assemble into a bilayer so that the hydrophobic chains are shielded by the hydrophilic head groups. Since each cell maintains its own organism-specific lipid compositions and each type of lipid has its own distinct physical property, there may be correlations between the physical properties of lipids and lipid-related functions. Indeed, there are concrete examples showing that a change of the physical state of the lipid bilayer can affect the functions of embedded proteins [1, 2]. All these observations indicate the importance of the physical properties of the membrane.

The lipid matrix of cell membrane is a natural binding site for amphipathic molecules which have separate hydrophobic and hydrophilic regions. The physical properties of the membrane may be altered by the binding of amphipathic

molecules, including proteins, and organic molecules such as drugs, detergents and others [3]. When amphipathic molecules interact with the membrane it may change the function of the cell by altering the physical properties of the membrane [1]. And the binding molecules may also undergo conformation transitions during the interaction process [4]. Thus, it is very important to understand the impact and the mechanism of the interaction between amphipathic molecules and membranes.

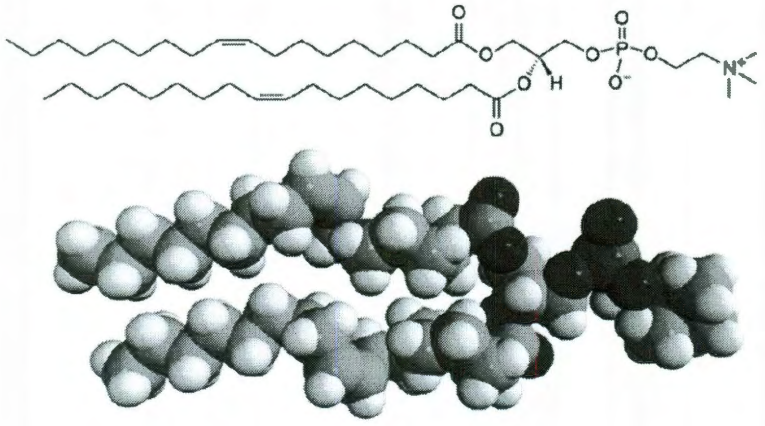

Figure I 1(top) The structure formula for 1,2-dioleoyl-*sn*-glycero-3-phosphocholine (DOPC) as an example of a single phospholipid molecule. (bottom) Space-filling model for the same phospholipid molecule.

The purpose of this thesis is an attempt to contribute to this understanding. My thesis consists of developing new methods for studying the kinetics of molecular interactions with membranes and comparative studies of a number of different membrane active molecules including peptides, proteins and drugs. In the past twenty years, our lab has developed various methods for investigating the structural properties of membrane-peptide interacting. These methods investigate the effects of peptides embedded in membranes in the equilibrium state, typically as a function

of the peptide concentration in membranes. My contribution to the methodology is to complement these static methods with kinetic observation. We established a micropipette aspiration system based on the system developed by Evan Evans in the 80's, but instead of measuring the basic physical properties of the membranes, we used it to study the dynamic interaction processes between amphipathic molecules and membranes. In the living biological systems, all interaction processes are kinetic. The results of kinetic experiments are usually complex, but with references to the equilibrium studies, the complex behavior can be analyzed. Thus the mechanism of the interactions between amphipathic molecules and membranes can be best understood by combining kinetic measurements with equilibrium measurements.

Until recently our lab has focused on the problem of antimicrobial peptides. In particular we have resolved the structures of the pores formed by antimicrobial peptides, and analyzed the energetics of peptide-membrane interactions. In my thesis, I studies a number of non-pore forming molecules. By these comparative studies, we now have a broader view and unified understanding how molecules, including proteins and drugs, interact with membranes. Most surprisingly we found that membrane binding may promote the formation of β-amyloid aggregates for certain peptides that might have significant implications to Alzheimer's disease and diabetes.

We also modified our micropipette aspiration system to measure the free energies of adhesion and hemifusion of lipid bilayers. We used two sets of micropipette aspiration systems to manipulate membrane-membrane interactions.

We then incorporated a third micropipette to inject mediators between two membranes. Our method was able to measure the energies of adhesion or hemifusion of lipid bilayers which varied over two orders of magnitude from -1 to -50×10^{-5} J/m^2. Most importantly, our method is capable of measuring the energy of transition in each step of lipid transformation during membrane fusion. This is relevant to current research on membrane fusion which focuses on how the proteins induce the lipid transformations.

The review of the methodology

Three independent methods, including x-ray diffraction, circular dichroism and micropipette aspiration method, were used in this thesis. X-ray diffraction was used to measure the membrane thinning effect by amphipathic molecules; circular dichroism spectrum was used to monitor the orientation transition of the amphipathic molecules bound to membrane; and the micropipette aspiration method was used to gauge the changes of surface area and volume of the giant unilamellar vesicles (GUV) as a result of interaction with amphipathic molecules. I found that the binding effect of amphipathic molecules on membrane can be best understood by the combination of these three methods. The following is a mini history of these three methods.

Our lab first developed the method of Oriented Circular Dichroism (OCD) to detect the orientation of peptides in membrane. Researchers previous in the lab used OCD to detect the orientation of helical peptides, alamethicin [5], magainins [6]

and melittin [7], bound in membranes. They found that all of those peptides exhibit two distinct orientations one corresponding to surface absorption with the helix parallel to the bilayer and the other with perpendicular transbilayer insertion. Heller et al. [8] and Weiss et al. [9] used the same method to discover the two distinct states of β-sheet antimicrobial peptide Protegrin-1 (PG-1) in lipid bilayers.

Wu et al.[10],Ludtke et al. [11], Heller et al. [12], and Chen et al. [13] used x-ray diffraction to measure the changes in the membrane thickness and found that at low concentrations the peptide in the surface state caused membrane thinning in direct proportion to the peptide concentration. However, if the concentration exceeded to a threshold value, the peptides began to insert into membranes and the thinning stopped [13]. The results indicated that the membrane thinning effect is a mechanism promoting the formation of peptide-induced pores.

To study the kinetics we adopted the micropipette aspiration method developed by Evans and collaborators about thirty years ago who measured the elastic moduli of lipid bilayers [14, 15]. A single GUV was aspirated and pressure was applied by a glass micropipette. To measure the area-tension relations, through which they calculated the elastic bending and area stretch moduli.

Evans and his collaborators also used a similar aspiration method to measure the Van der Waals force [16] and the adhesion energy [17, 18] between two vesicles. Two GUVs were aspirated by two micropipettes and brought into close contact. Adhesion was achieved by releasing the suction pressure on one GUV against another tensed GUV. The mechanical analysis of the shape transitions provided the

interfacial free energy density for the surface affinity. In this thesis I will describe how we modified this method for kinetic studies and also developed a new theory for measuring membrane-membrane interactions.

Four experiments

In this thesis I performed four different experiments. In the first two experiments I studied the drug-membrane interactions for which biological effects have been widely reported but poorly understood. The third was the kinetic process of β-Amyloid formation via membrane binding. These three systems were studied as a contrast to previous studies on antimicrobial peptides which formed transmebrane pores. The comparison of all these different membrane-binding molecules gave us a broad understanding of membrane-molecule interactions. In the fourth experiment, I extended the methods to study the problems related to membrane fusion. I will give a short introduction on each case. My preliminary experiments with pore-forming proteins are included in the appendices.

Interaction of Curcumin with lipid bilayers

Curcumin is an example of amphipathic drugs that bind to cell membranes[19, 20]. Interaction of curcumin with lipid bilayers is not well understood. A recent experiment showed that curcumin significantly affected the

single-channel lifetime of gramicidin in a 1,2-dioleoyl-sn-glycero-3-phosphocholine (DOPC) bilayer without affecting its single-channel conductance[1]. We describe dual measurements of membrane thickness change and membrane area change due to the binding of amphipathic drug curcumin. The combined results allowed us to analyze the binding states of a drug to lipid bilayers, one on the water-membrane interface and another in the hydrocarbon region of the bilayer. The transition between the two states is strongly affected by the elastic energy of membrane thinning (or equivalently area stretching) caused by interfacial binding. The data are well described by a two state model including this elastic energy. The binding of curcumin follows a common pattern of amphipathic peptides binding to membranes, suggesting that the binding states of curcumin are typical for amphipathic drugs.

Interaction of Tea catechin (-)-Epigallocatechin gallate with lipid bilayers

A major component of green tea extracts, catechin (—)-Epigallocatechin gallate (EGCg) has been reported to be biological active and interacting with membranes [21-30]. A recent paper reported drastic effects of EGCg on giant unilamellar vesicles (GUVs) [29]. In particular, EGCg above 30 μM caused GUVs to burst. We investigated the effect of EGCg on single GUVs at lower concentrations, believing that its molecular mechanism would be more clearly revealed. We used the micropipette aspiration method and x-ray diffraction to study the interaction of EGCg with membrane. To understand the property of EGCg, we also compared its effect with other membrane-active molecules, including pore-forming peptide

magainin [31], the turmeric (curry) extract curcumin [32, 33], and detergent Triton X100. We found the effect of EGCg somewhat unique. Although EGCg readily binds to lipid bilayers, its membrane area expansion effect is one order of magnitude smaller than curcumin. EGCg also solubilizes lipid molecules from lipid bilayers without forming pores, but its effect is different from Triton X100.

Kinetic process of β-Amyloid formation via membrane binding

Jarrett and Lansbury's [34] nucleation-dependent polymerization model describes the generic process of β-amyloid formation for a large number of diverse proteins and peptides. Here, we discuss a case of membrane-mediated nucleation that leads to β-aggregation. Like the prototype β-amyloid peptide Alzheimer's Aβ 1–40, penetratin is a random-coil monomer in solution but changes to α-helical or β-like conformations in the presence of anionic lipid membranes. Lee et al. [4] have studied thermodynamics of membrane-mediated β-amyloid formation in equilibrium experiments using penetratin-lipid mixtures. The results showed that penetratin bound to the membrane interface in the α-helical conformation when the peptide-to-lipid (P/L) ratios were below a lipid-dependent critical value P/L^*. When P/L reached P/L^*, small β-aggregates emerged, which served as the nuclei for large β-aggregates. Here we studied the corresponding kinetic process to understand the potential barriers for the membrane-mediated β-amyloid formation. We performed kinetic experiments using giant unilamellar vesicles (GUVs) made of 7:3 DOPC/DOPG. The observed time behavior of individual GUVs, although complex, exhibited the physical effects seen in equilibrium experiments. Most interestingly, a

potential barrier appeared to block penetratin from translocating across the bilayer. As a result, the kinetic value for the critical threshold P/L^* is roughly one-half of the value measured in equilibrium where peptides bind symmetrically on both sides of lipid bilayers.We also investigated the similarity and differences between the charged and neutral lipids in their interactions with penetratin. We reached an important conclusion that the bound states of peptides in lipid bilayers are largely independent of the charge on the lipid headgroups.

Method of measuring the free energy of adhesion and hemifusion

Some fundamental interactions between lipid bilayers are well known and have been extensively studied, such as van der Waals interactions [16, 35], electrostatic double-layer forces [35], short-range repulsive hydration forces [36], and undulation-induced steric repulsion [37]. These are the forces between two (flexible) surfaces. There are other possible interactions between lipid bilayers due to the fact that lipid bilayers possess internal structures as well as degrees of freedom, including the possibility of redistribution of multiple lipid components. This latter type of interactions are induced by molecular mediators and resulted in either adhesion or partial merging between bilayers. Partial merging, i.e., merging of the contacting leaflets but not the distal leaflets, is called hemifusion in the study of membrane fusion [38-43]. In the course of our studies with various membrane-active molecules we have encountered a number of such examples. Some of these adhesion or merging reactions occurred only at low pH. We believe that similar reactions could be significant to membrane fusion. They could also distort the

results of non-fusion vesicle experiments, if the possible vesicle-vesicle reactions are not understood. For illustration, we discuss three examples: spontaneous adhesion between phospholipid bilayers induced by low pH; polymer-induced osmotic depletion attraction between lipid bilayers; anionic lipid bilayers crossbridged by multi-cationic peptides. Our purpose here is to describe a general method for studying such interactions. We used giant unilamellar vesicles, each aspirated in a micropipette so that the tension of the membrane and the membrane area changes could be monitored during the bilayer-bilayer interaction. In particular we devise a general method for measuring the free energy of adhesion or hemifusion. The results show that the energies of adhesion or hemifusion of lipid bilayers can vary over two orders of magnitude from -1 to -50×10^{-5} J/m^2 in these examples alone. Our method is capable of measuring the energy of transition in each step of lipid transformation during membrane fusion. This is relevant to current research on membrane fusion which focuses on how the proteins induce the lipid transformations.

Chapter 1

Micropipette aspiration method

In this chapter, I will first introduce the giant unilamellar vesicles (GUVs), the the micropipette aspiration method, and also the protocols of preparing them. Then I will discuss the instrument setup of the aspiration system in our lab. Finally, I will talk about the experiment setup for studying the interaction between amphipathic molecules with membranes and also the setup for measuring the free energies of adhesion and hemifusion.

1.1. Giant unilamellar vesicles (GUVs)

Bilayer vesicles self-assemble in solution from phospholipids. Vesicles can be prepared by different methods, resulting in a great variety of sizes from nanometers to hundreds of microns. Small unilamellar vesicles (SUVs) have the smallest

diameter around 20-50nm. Large unilamellar vesicles (LUVs) are 100-1000nm in diameter while giant unilamellar vesicles (GUVs) range in size from 1-100μm. In this study we use GUVs as a model system for cell membrane since they have similar size and composition. GUVs are distinguished from LUVs because their size allows them to be directly observed under microscope. As a result, it allows a variety of experiments to be conducted at the level of the single vesicle. Many vesicles experiments have been carried out on a suspension of many small vesicles such as LUVs and SUVs using fluorescence spectroscopy, light scattering, and x-ray scattering.

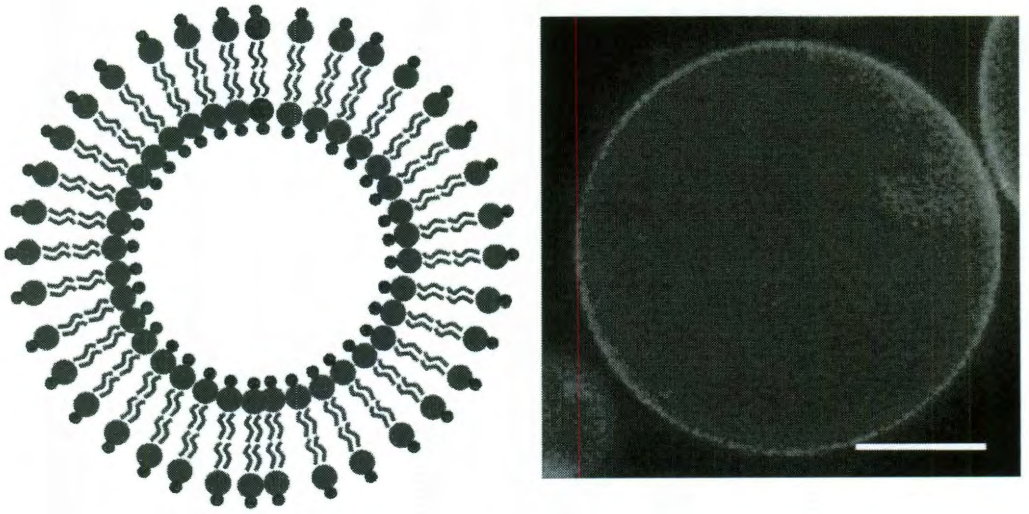

Figure 1-1 (left) Schematic of giant unilamellar vesicles (GUV). Rhodamine B (red) was labeled on the head group of 1,2-dioleoyl-*sn*-glycero-3-phosphoethanolamine (DOPE, purple). (right) Fluorescent image of a single GUV labeled with 0.4% molar ratio of Rh-DOPE under 20X objective. (bar=10μm)

Under this condition, what has been observed is the average behavior of a large number of vesicles, while the information of the individual vesicle cannot be

gathered. By contrast, the study of a single GUV allows us to get information on the structure and physical properties of individual vesicle in real time [44]. It has been used for investigations of the physical and biological properties of lipid membranes such as elasticity and shape change [14].

1.2. Sample preparation

GUVs were produced in 200 mM sucrose solution by the electroformation method [45]. Lipid and 0.4% molar ratio of a headgroup-fluorescent lipid were co-dissolved in chloroform. (A fluorescent lipid was added to enhance the contrast of the GUV boundary. We found no difference between the two fluorescent lipids, Rh-DOPE and DiO.) The lipid solution (~0.07 mg lipid) was deposited onto two ITO coated glass cover slips. After drying under vacuum, an o-ring was sandwiched between two ITO slips and the gap was filled with 200 mM sucrose solution (Figure 1.2). 3 V AC at 10 Hz was applied between the two ITO electrodes for 1 h. Subsequently the frequency was adjusted to 5 Hz for 20 mins and followed by 0.5 Hz for 30 mins. This electroformation method has been shown to produce unilamellar large vesicles [45]. The vesicle suspension was then gently collected in a glass vial. The vesicles were used within 24 hours of production.

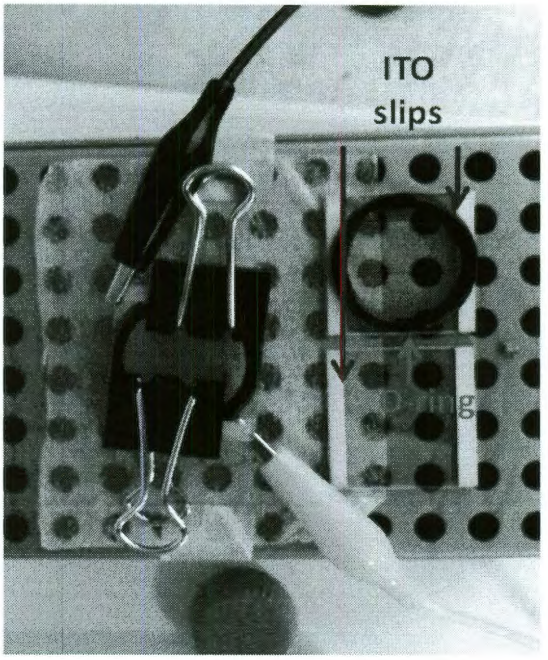

Figure 1-2 ITO slips chamber was used to produce GUVs. An o-ring was sandwiched between two ITO slips to create a solution chamber. Two binder clips was used to seal the chamber. The chamber was connected to an AC power supply by two alligator clips. Each ITO slip was reused for several times after intensive cleaning with ethanol.

1.3. Aspiration system setup

The aspiration system includes four parts: the Ti-U inverted fluorescent microscope, the pressure control system, the humidifier, and the microinjection system.

1.3.1. Ti-U inverted fluorescent microscope

Epifluorescence microscopy is a method of fluorescence microscopy that is widely used in life sciences. The excitatory light from the mercury lamp, Nikon C-

HGFIE, first passed through the dichroic/filter set cube, then focused on the specimen by objective. Dichroic/filter set cube was used to select the excitation and emission wavelengths to match the characteristics of the fluorophore used to label the specimen. Generally speaking, green light was selected to excite the red fluorophore while blue light to excite the green fluorophore. The emission light from the specimen was collected by the objective, then passed through the Dichroic/filter set cube again to filter out the remaining excitation light, and finally was recorded by a CCD camera, Nikon coolSNAP HQ2. The objective we used was a 20X NA0.45 long working distance objective with a built-in phase plate to obtain phase contrast image of the specimen.

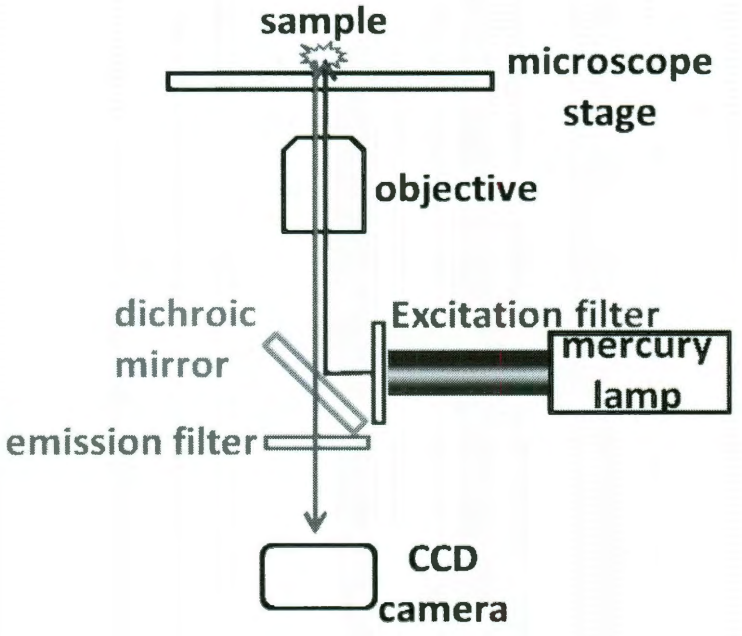

Figure 1-3 Schematic of an epifluorescence fluorescence microscope

1.3.2. Pressure control system

Two methods were used to provide the aspiration pressure. In the first method, we used a micro syringe to control the aspiration pressure. Micropipettes were made by a micropipette puller, Sutter Instrument Company P-97 (Novato, CA) and refined by a microforge, Narishige MF-900 (East Meadow, NY). The tail end of the aspiration pipette was connected to a pressure control system constructed similarly to a setup described by Fygenson et al. [46]. A syringe was used to create a negative pressure inside the micropipette, which was referenced to the atmospheric pressure by a water-filled U tube. The syringe was mounted on a mcroinjector holder. The aspiration pressure was precisely controlled by turning the knob on the microinjector to decompress the solution in the syringe. Full rotation of the knob on the microinjector was approximately 40μl. The value of the negative pressure was monitored via a manometer MKS Baratron 223 (Andover, MA) and recorded for post-experimental inspections. The main disadvantage of this system was the existence of many connecting joints among different parts of the system which led to the need for them to be well-sealed in order to maintain a stable pressure.

A height-adjustable water reservoir was used to provide the aspiration pressure in the second method. Micropipette was held by a pipette holder (Narishige, East Meadow, NY) which was connected to a water reservoir by a Teflon tube. The aspirating negative pressure was produced by this height-adjustable water reservoir which was mounted on a motorized mechanical slider (Robocylinder, Torrance, CA). The height of the water reservoir could be controlled by the software

with a 0.01mm resolution. The "zero pressure" position was defined as the water reservoir position where no water flowed (neither inflow nor outflow) through the micropipette tip when the tip was in the solution chamber. The aspiration pressure was generated by lowering the water reservoir to a new position. From the distance between this "new position" and the "zero pressure position", the aspiration pressure was calculated by a simple equation$\Delta P = \rho g \Delta h$, where ρ is the density of the water, g is the gravitational constant, and Δh is the distance between this two positions.

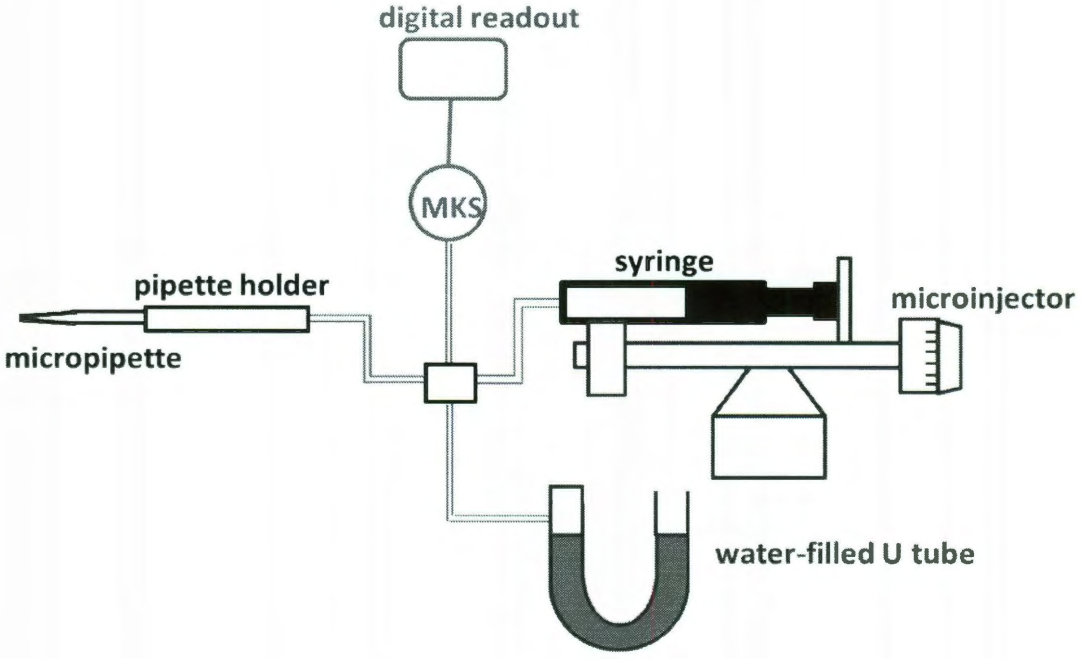

Figure 1-4 Schematic of the micro syringe pressure system. The micropipette was mounted in a three axis hydraulic micromanipulator. Syringe and a thumbwheel-driven microinjector were used to create a negative aspiration pressure. A Labview program was used to control the MKS manometer and also used to read out and record the pressure value from it.

When compare to the micro syringe method, the water reservoir method has a relatively simple setup by directly connecting the micropipette holder to the water reservoir. Furthermore, instead of using a manometer to monitor the pressure, the pressure can be directly calculated using the difference in heights between two points. Base on my experience, the water reservoir method provides a relatively stable and well-controlled pressure when compared to the other method.

1.3.3. Ultrasonic humidifier

Ultrasonic humidifier was used to prevent water evaporation from the solution chamber by providing water vapor around the chamber. It is well known that the volume of the GUV remains constant only when the osmotic balance is maintained between the inside and the outside of the GUV. Water evaporation from the solution chamber will increase the osmolarity outside the GUV and thereby the volume of the GUV will decrease. In order to calculate the change in surface area of the GUV, the volume needs to maintain constant (detail see 3.2.3 and 4.3.1). For this reason, we used ultrasonic humidifier to maintain a stable osmolarity of the solution inside the chamber.

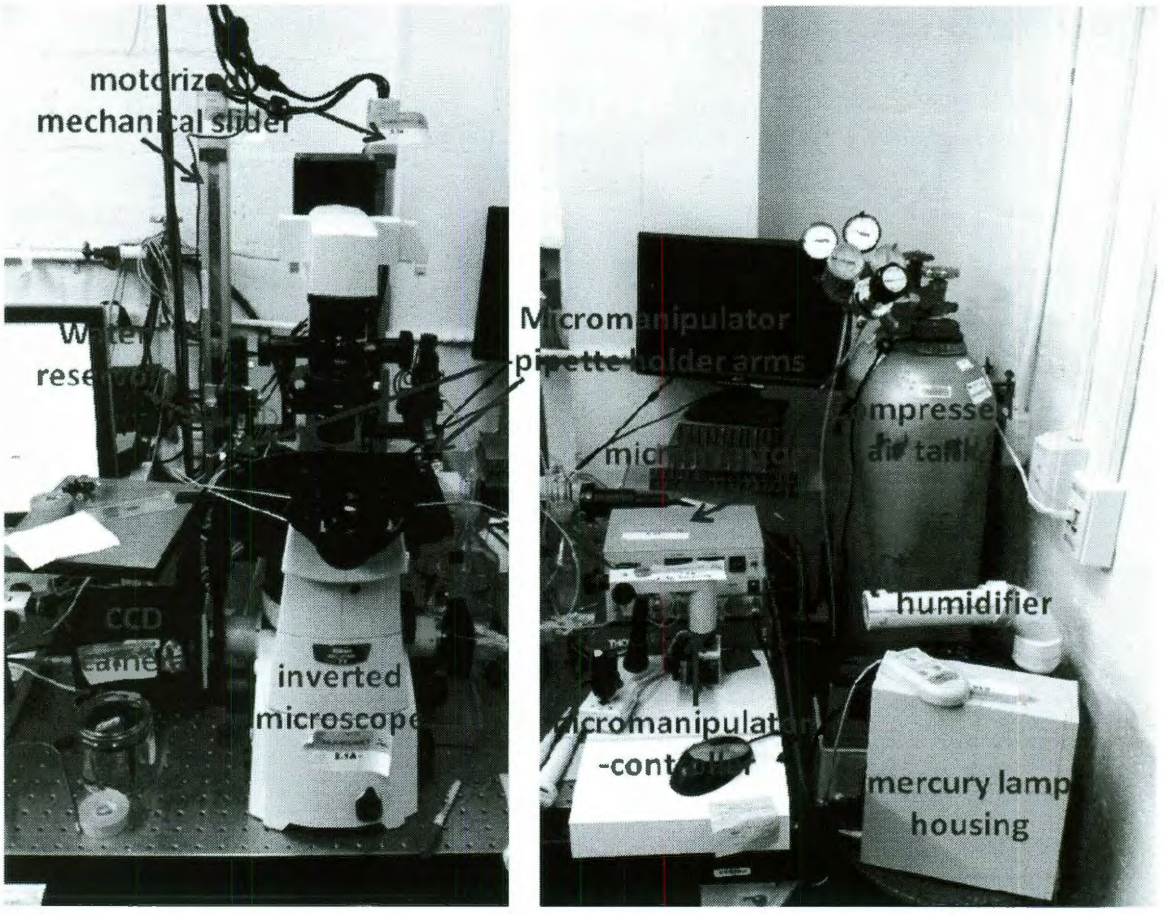

Figure 1-5 The aspiration system in our lab

1.3.4. Microinjection system

In some of the experiments, we used a third micropipette to inject mediators to induce adhesion or hemifusion. This microinjection system can also be used to inject peptides or drugs toward the GUVs to study the effect caused by peptides-membrane (or drugs-membrane) interaction. An electrical microinjector, Narishige IM-31 (East Meadow, NY) was used to control the injection pressure. The

microinjector was connected to a compressed nitrogen gas tank which provided a positive pressure. The injection pressure was adjusted by turning the valve on the microinjector. The "balance pressure" used before and after the injection was controlled by a balance valve. We set this "balance pressure" to be a small negative pressure so that no solution in the injection pipette was leaked while not injected. A foot switch connected to the microinjector was used to trigger the injection.

1.4. Narishige MF-900 microforge

A MF-900 microforge was used to refine micropipette tips. It incorporated a heater unit into a microscope unit. The heater unit contained a heating source, a heater manipulator and a 150 μm platinum wire heating element. The heater manipulator was used to hold and position the platinum wire heating element. Before fabricating the micropipette, a glass bean which allowed fabrication of a thin micropipette by making use of the surface tension of the glass was formed on the platinum wire. The micropipette was held by another manipulator from the opposite side of the heater manipulator. By adjusting the manipulator, the micropipette was brought over the glass bead at the desired thickness to be cut. After the micropipette was bought into contact with the glass bead, heat was switched on by depressing the foot switch and was gradually increased by turning the heat adjustment knob until the micropipette was melted onto the glass bead. The heat was suddenly cut off by releasing the foot switch once the micropipette was melted into the glass bead. The micropipette was cut at the contacted point

with the glass bead. The micropipette tip was fire-polished by moving the tip to a position parallel to the glass bead and then heat was applied to slightly melt the tip opening.

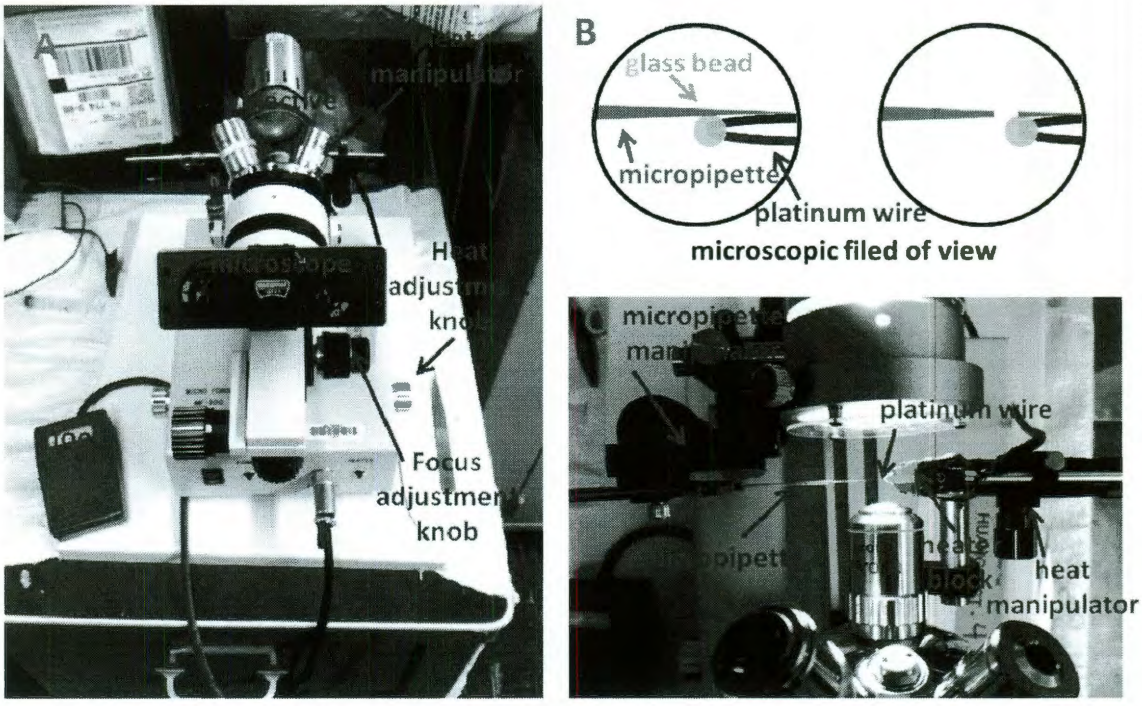

Figure 1-6 (A) Narishige MF-900 microforge (B) Microscopic file of view of producing a holding micropipette. (left) Micropipette was in point contact with a glass bead which was heated up by a platinum wire (right) By switching off the heating power, the glass bead cooled down and the micropipette was cut from the contact point. (C) A closer view of the heat manipulator and the micropipette manipulator

1.5. Study of amphipathic molecules interacting with membrane

1.5.1. Experiment setup

To perform the GUV experiment, the vesicles were first transferred to a control chamber containing a ~190 mM glucose and 10 mM HEPES solution. The osmolality of every solution used in the GUV experiment was measured by a Wescor Model 5520 dew-point Osmometer (Wescor, Logan, UT). The osmolality of the solution in the control chamber was the same as 200 mM sucrose solution inside the GUVs. A micropipette (of inner radius 8-10μm) was used to hold a single chosen GUV (of 25-35μm in radius) by aspiration at a constant negative pressure (which created a membrane tension 0.5 dyn/cm-1 dyn/cm). Before use, the micropipette was coated with 0.5% bovine serum albumin in order to neutralize the charge on the bare glass surface [47] and washed extensively by 200mM sucrose solution. Micropipette was held by a motor-driven micromanipulator Narishige MM-188NE (East Meadow, NY) and connected to a micrometer-positioned water (or oil) manometer.

The single GUV aspiration experiment was performed by transferring the aspirated GUV to an observation chamber that contained a target peptide (or drug)/glucose/HEPES solution (see schematic in Figure 1.7). The observation chamber was set side-by-side with the control chamber, separated by ~1cm. A transfer pipette (inner diameter 0.75mm), filled with the control solution, was

inserted from the opposite side of the aspiration pipette through the observation chamber into the control chamber. The aspiration pipette and the transfer pipette were held separately by motor-driven micromanipulators Narishige MM-188NE (East Meadow, NY). The aspirated GUV was inserted ~0.7mm into the transfer pipette in the control chamber. By moving the microscope stage, the aspirated GUV in the transfer pipette was moved from the control chamber to the observation chamber. Then the transfer pipette was swiftly moved away, so that the GUV was exposed to the target peptide (or drug)/glucose/HEPES solution (marked as t=0).

If the observation chamber contained a glucose/HEPES (without target peptide (or drug)) solution isotonic to 200 mM sucrose solution, the GUV remained unchanged, as expected. When target peptide (or drug) was present in the solution of the observation chamber, the vesicle projection in the micropipette will change in real time due to the interaction between the target peptide (or drug) and the GUV membrane. The video image of the process was captured by a Nikon coolSNAP HQ2 camera.

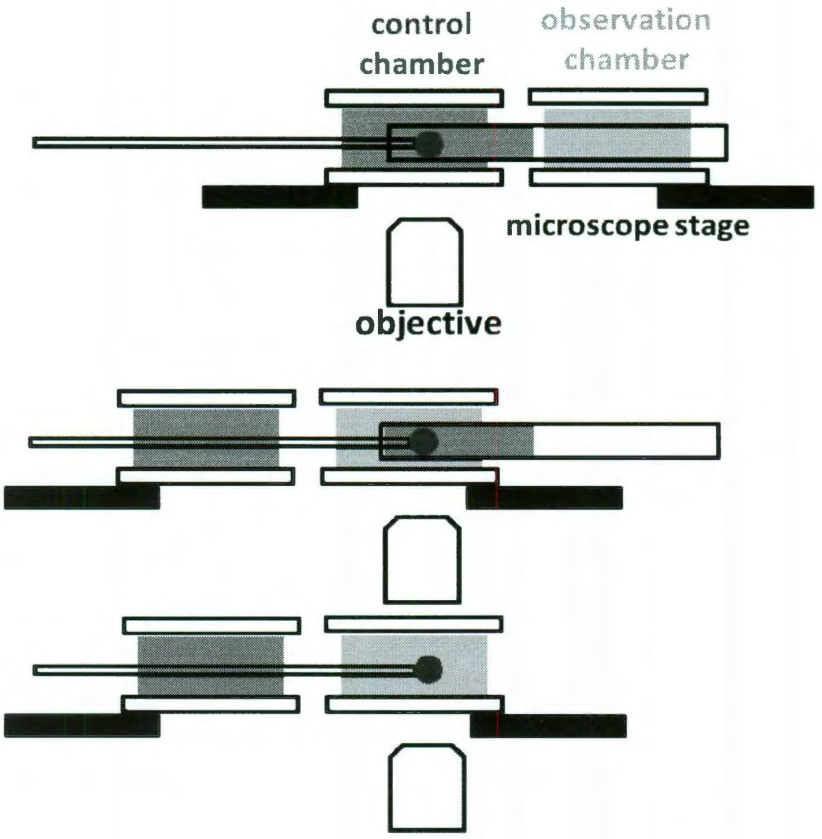

Figure 1-7 Schematic of the GUV experiment. An aspirated GUV was inserted ~0.7mm into the transfer pipette in the control chamber. 2. The aspirated GUV in the transfer pipette was moved from the control chamber to the observation chamber. 3. Then the transfer pipette was swiftly moved away, so that the GUV was exposed to the solution in observation chamber (marked as t=0).

1.5.2. Data analysis

An aspirated GUV consisted of a cylindrical protrusion (length L_p) in the micropipette (radius R_p) connected to the spherical vesicle (radius R_v) at the tip of the micropipette (see Figure 1.8). The protrusion length would change if there was a change in the surface area A and/or the volume V of the GUV, as a result of

interaction with peptide or drug. From the geometry of an aspirated GUV, the change of the surface area A is related to the changes of L_p and the GUV radius R_v (see Figure 1.8) by $\Delta A = 2\pi R_p \Delta L_p + 8\pi R_v \Delta R_v$, and the change of the GUV volume V by $\Delta V = \pi R_p^2 \Delta L_p + 4\pi R_v^2 \Delta R_v$. In general the changes of GUV radius ΔR_v were too small to be measured accurately. When inside and outside of the GUVs were isotonic, the change of volume should be zero. Under the condition ΔV=0, ΔL_p is directly proportional to ΔA: $\Delta A = 2\pi R_p\left(1 - L_p/R_v\right)\Delta L_p$.

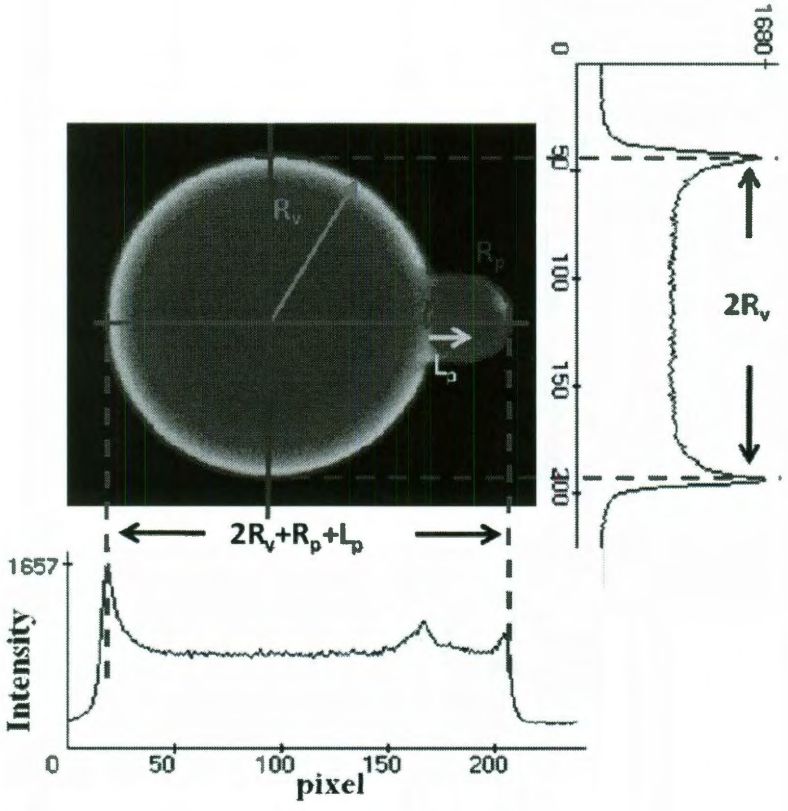

Figure 1-8 Schematic of how to analysis GUV image. R_v was calculated by half of the distance between two peaks of the intensity profile cut through the center of the GUV (red line). R_p was calculated by the best circular fitting curve (purple circle) of the curved segment inside the micropipette. The distance between two peaks (D_{ptp}) of the intensity profile cut through the center of the

GUV and the center of the micropipette (blue line) equaled to $2R_v+R_p+L_p$. From this relation, L_p could be calculated as $D_{ptp}-2R_v-R_p$.

Under other conditions, such as peptide forming pores and osmolarity unbalance between inside and outside of the GUVs, the volume of the GUVs may change due to influx or outflux of the solution while the area keeps constant. When $\Delta A=0$, $\Delta V = -\pi R_p(R_v - R_p)\Delta L_p$. From the recorded video images, we measure ΔL_p as a function of time by using the Nikon NIS-Elements BR 2.30 software. Then we can calculate the area or volume change with time from the geometry. Figure 1.8 shows one example how to determine the R_v, L_p and R_p.

1.6. Experiment setup for measuring the free energy of adhesion and hemifusion

1.6.1. Weak Adhesion experiment

We used a similar experiment set-up as described in previous section except adding in another set of micropipette aspiration system and aspirated two GUVs at the same time. Since the aspiration pressures of two GUVs were controlled by two individual systems, the aspiration pressure can be adjusted separately.

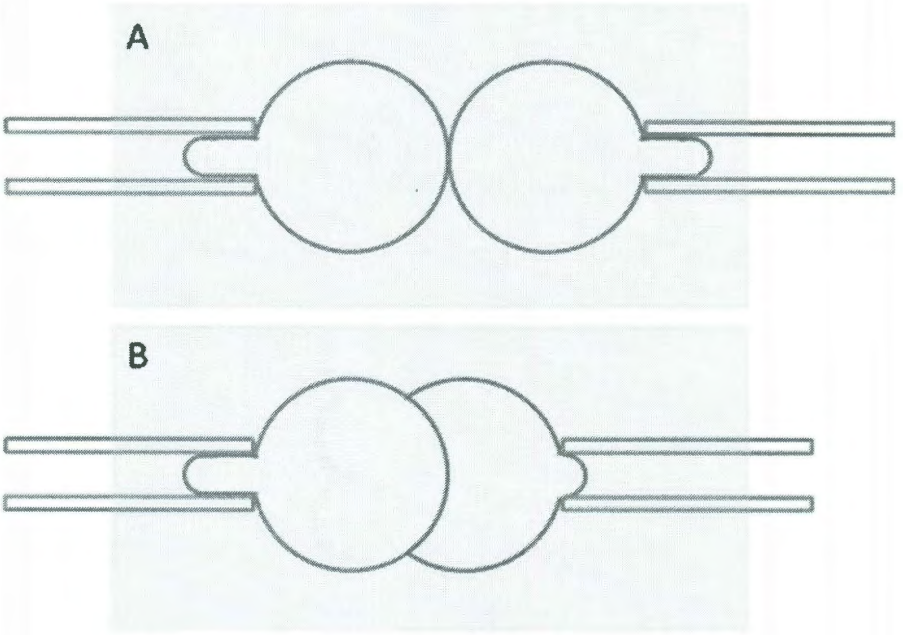

Figure 1-9 Schematic of weak adhesion experiment setup. (A) Two tensed GUVs were aspirated by two micropipettes and brought into slightly contact. (B) Stepwise (0.5 mm-oil/step) released the aspiration pressure on the right hand side GUV and allowed it to adhere onto the left hand side GUV

GUV suspension (at 200 mM osmolality) from the production chamber was transferred to an observation chamber that contained glucose solution with higher osmolality. The GUV rapidly deflated to a smaller volume. During the adhesion experiment, one tensed GUV was held at the constant suction pressure and the second GUV was aspirated by another micropipette with an initial suction pressure equivalent to ~20 mm water. After these two GUVs were brought to have slightly contact with each other, the suction pressure in the second pipette was decreased stepwise by lowering the water reservoir. Adhesion of two GUVs occurred during this process. In reversal, the adhered GUV was dissociated from the tensed GUV by

stepwise increases in suction pressure, so the reversibility of the adhesion process could be evaluated (Figure 1.9).

1.6.2. Adhesion induced by a transient presence of mediators

In this part of the study, we used two individual aspiration systems to aspirate two GUVs and in addition to previous setup we added a third injection pipette to inject a small amount of mediators between two tensed GUVs. For this experiment, the osmolality of the glucose solution in the observation chamber was kept the same as the sucrose solution in the production chamber. Two GUVs were aspirated by two separate micropipettes (diameter 8-16 μm), each to a membrane tension about 0.7 dyn/cm, and were then positioned to slightly in contact with each other. From a distance ~200 μm, a third pipette (diameter ~15 μm) was used to inject isotonic PEG or TAT solution toward the vicinity of the two contacting GUVs. The injection micropipette was connected to an electrical microinjector, Narishige IM-31 (East Meadow, NY), which was driven by a compressed gas. A small negative pressure was maintained before and after injection so as to ensure that no solution in the injection pipette was leaked. The injection was triggered by a foot switch connected electrical microinjector set at ~ 1 kPa. The injection rate was calculated to be 0.015 μL per sec (Figure 1.10).

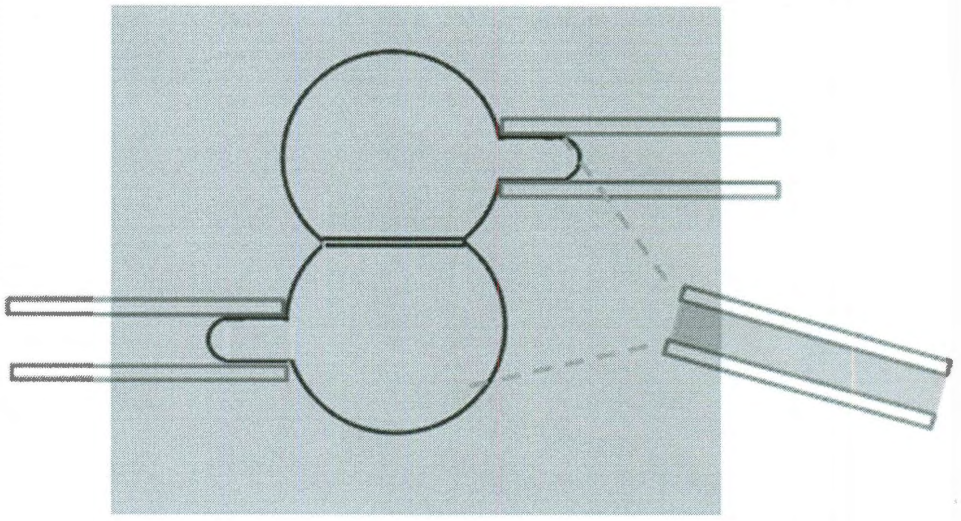

Figure 1-10 Schematic of strong adhesion experiment setup

Chapter 2

Other Techniques

In this chapter I will first give a brief introduction on the x-ray lamellar diffraction method which includes the basic principle of x-ray lamellar diffraction, the sample preparation protocols, experiment setup and data reduction. Then I will shortly discuss the basic principle and the experiment setup of circular dichroism.

2.1. X-ray lamellar diffraction

2.1.1. Lamellar x-ray diffraction on multilayers

When lipids were dried on the substrate, multilayers which lay parallel to the substrate will be formed automatically. The periodic bilayers stack up along z direction and extend horizontally on the surface of the substrate. Suppose there are

N bilayers of repeat distance D in this multilamellar sample, the electron density of the sample can described as,

$$\rho(z + nD) = \rho(z) \text{for } n = 0,1,2, \ldots . N - 1$$

When the multilamellar is in fluidic phase, we only need to integrate over the z-direction since the electron density distribution is uniform throughout the x-y plane. Then the scattering intensity can be written as:

$$I(q) = I_e \left| \int_0^{ND} \rho\,(z) e^{-iqz} dz \right|^2$$

Where I_e is the unit scattering intensity from a single electron. With periodicity condition,

$$I(q) = I_e \left| \sum_{n=0}^{N-1} e^{iqnD} \int_0^D \rho(z) e^{-iqz} dz \right|^2 = I_e \left| e^{-iq(N-1)D/2} \frac{\sin(\frac{NqD}{2})}{\sin(\frac{qD}{2})} \int_0^D \rho(z) e^{-iqz} dz \right|^2$$

Notice that for large values of N, the sine term will have a sharp maximum when the denominator is approaching zero. This will occur when

$$\frac{qD}{2} = n\pi \text{ for } n = 0. \pm 1, \pm 2 \ldots ..$$

Thus, the diffraction intensity for the multilamellar sample in directions with q satisfying Bragg conditions is

$$I(q) \propto N^2 \left| \int_0^D \rho(z) e^{-iqz} dz \right|^2 \text{ where } q = \frac{2\pi n}{D} \text{and } n = 0, \pm 1, \pm 2, \ldots .$$

Once the phases of the diffraction orders have been determined by the swelling method, the electron density profile can be reconstructed by using a inverse Fourier transform of the discrete structure factor $F\left(\frac{2\pi n}{D}\right)$. We can use a cosine transfer since the bilayer is symmetrical. Then the electron density profile along the z direction can be written as

$$\rho(z) = \sum_{n=1}^{m} F\left(\frac{2\pi n}{D}\right) \cos\left(\frac{2\pi n z}{D}\right)$$

2.1.2. Sample preparation

Peptide (or drug) was first dissolved in tetrafluoroethylene. Appropriate amounts of Peptide (or drug) and lipid of chosen peptide/lipid molar ratio, P/L, were mixed in 1:1 (v/v) chloroform and tetrafluoroethylene, and deposited on a thoroughly cleaned flat substrate (0.3 mg of lipid on 1 cm^2 of silicon wafer). After the solvent was removed in vacuum, the samples were hydrated by saturated water vapor at 35°C overnight.

The results were well-aligned, parallel, hydrated bilayers as proven by x-ray diffraction. The samples were kept in a temperature humidity chamber during the measurement. All experiments were performed at 25°C.

2.1.3. X-ray diffraction setup

The ω-2θ diffraction was collected on a Diffractus 581 (Enraf-Nonius, Delft, The Netherlands) and a four-circle goniometer (Huber Diffraktionstechnik, Rimsting, Germany),with a linefocused Cu K_α source (λ=1.542 Å) operating at 35 kV and 15–

30mA. The incident beam was collimated by a horizontal soller slit and two vertical slits on the front and the back sides of the soller slit. The horizontal and vertical divergences of the incident beam were 0.23° and 0.3°, respectively. The sample rotated with angle ω while the detector recorded the diffraction intensity at 2θ angle, following the reflection condition ω=2θ. The diffracted beam first passed through a vertical slit and then was discriminated by a bent graphite monochromator before entering a scintillation detector, which was biased to discriminate against higher harmonics and fluorescence. This diffractometer was designed to minimize the background signal, which in turn allowed the measurement of high diffraction orders. The experimental setup is shown in Figure 2.1 .

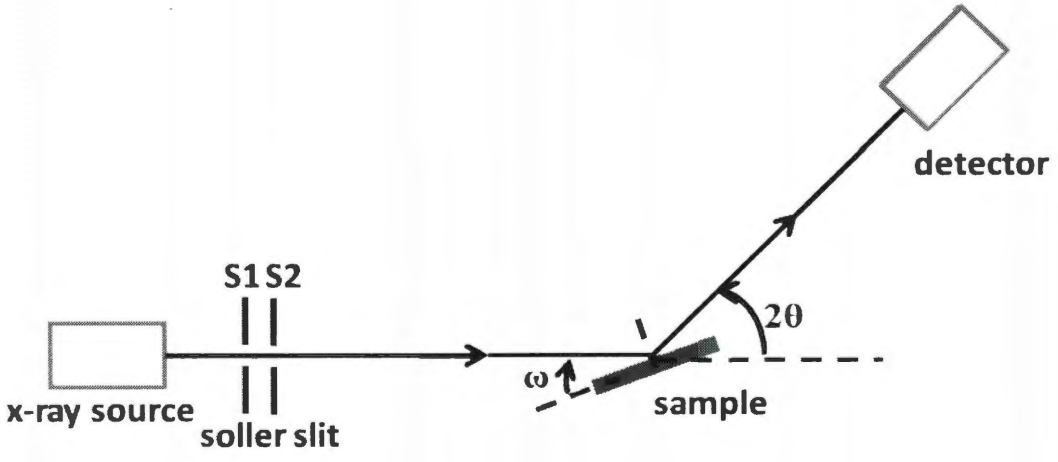

Figure 2-1 The experimental setup for ω-2θ diffraction. The incident beam was almost parallel to the substrate; i.e ω and 2θ are small. After diffracting by the sample, the beam was collected by the detector.

An attenuator was used to prevent the first-order Bragg peak from saturating the detector. Each ω-2θ scan was performed from ω=0.5° to ω=6.5° with a step size of Δω=0.01° (for details see [48]). The scan was repeated 3–5 times for each hydration level and then averaged for data analysis. The raw data of the recorded diffraction pattern was shown in Figure 2.2 as an example.

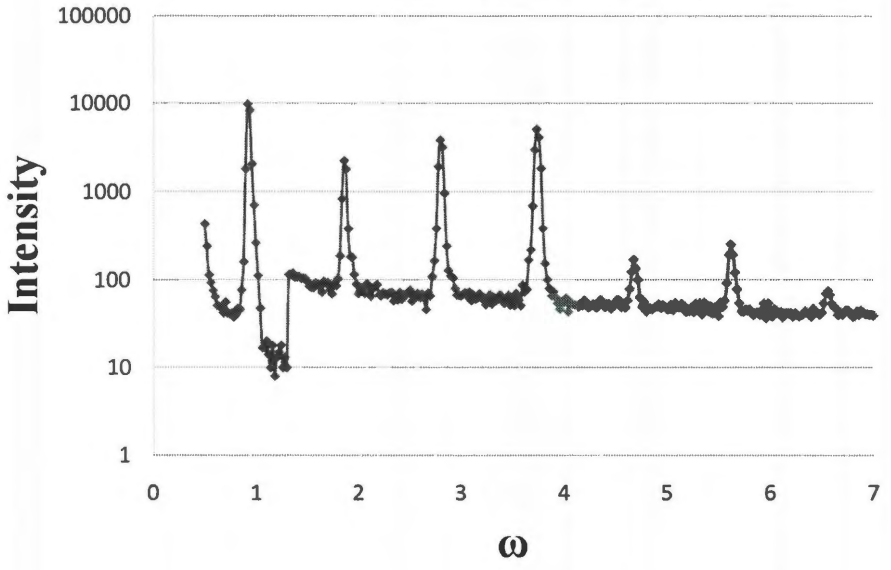

Figure 2-2 X-ray diffraction pattern averaged over 5 scans for DPhPC.

2.1.4. Swelling Method

The swelling method was used to solve the phasing problem when reconstructing the electron density profile [49]. This method was an application based on the Shannon Sampling Theorem. Accordingly, each sample was scanned at several different hydration levels from 90%RH to 98%RH. The temperature and the relative humidity were controlled by a homemade controller box. We assumed that

only the water layer thickness would change with the relative humidity, and then we could rescale the diffraction amplitudes at different hydration level. By going through a single structure factor curve, the phases of the diffraction amplitudes could thus be determined.

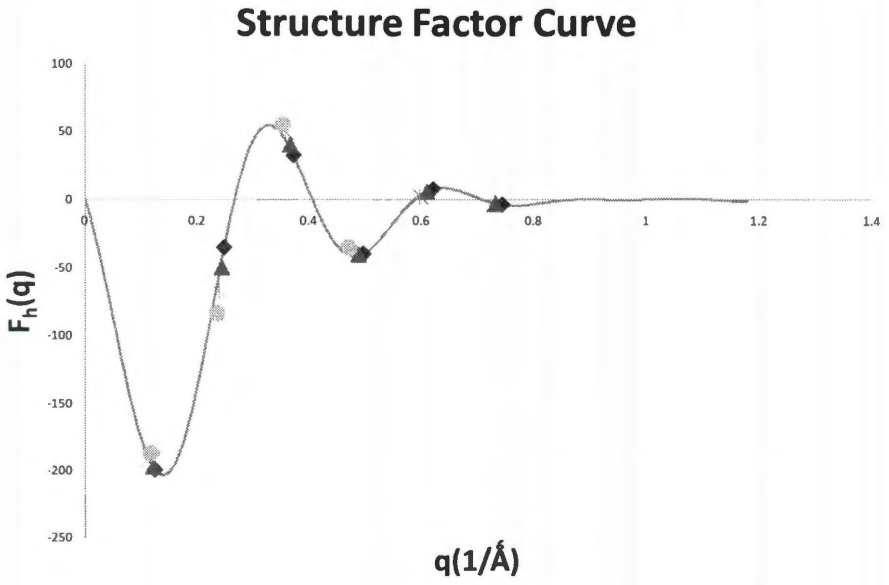

Figure 2-3 The swelling phase diagram of the lipid bilayers for DPhPC. The discreet points corresponded to the diffraction amplitudes obtained by experiment. The continuous line was the calculated form factor by using Shannon sampling theorem.

2.1.5. Data reduction

The procedure of data reduction was described in many of our previous works [48, 50]. Briefly, the measured diffraction intensity was first corrected for the attenuator absorption and for the detector's dead-time factor. After removing the background, data was corrected for sample absorption and diffraction volume. The

integrated peak intensities were then corrected for the polarization and the Lorentz factors. The relative magnitude of the diffraction amplitude was the square-root of the integrated intensity. The phases were determined by the swelling method [49, 50].

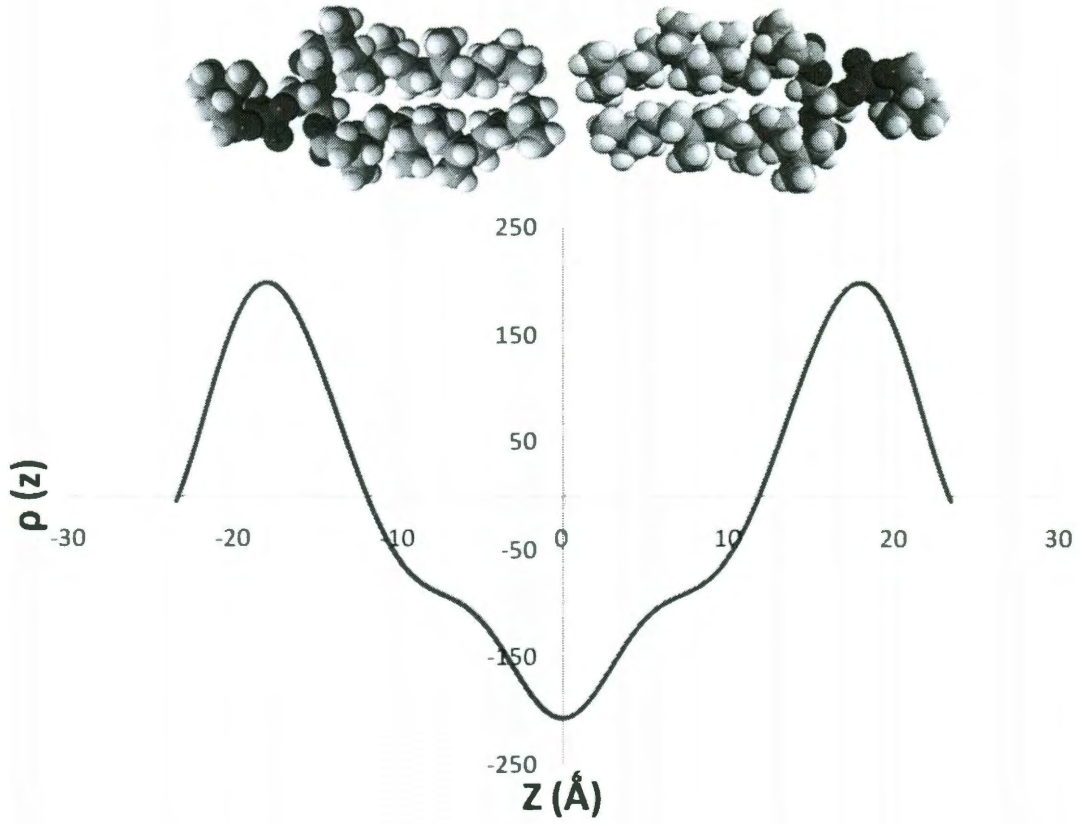

Figure 2-4 Reconstructed electron density profile of lipid bilayers. The peaks of the profile are the positions of the phosphate groups on the surface of the bilayers.

With their phases determined, the diffraction amplitudes can be used to reconstruct the electron density profile of the bilayer. Figure 2.4 shows an example

of reconstructed electron density profile of lipid bilayers. The peaks of the profile are the positions of the phosphate groups on the surface of the bilayers. Hence the peak-to-peak (PtP) distance across the bilayer is a good measure of the bilayer thickness.

2.2. Circular Dichroism

2.2.1. Basic principle of circular dichroism

Circular dichroism (CD) measures the differential absorption of left and right circularly polarized light which arise due to structural asymmetry. Secondary structure of the protein or peptide can be determined by CD spectrum in the far-UV region (190-250 nm). Alpha-helix, beta-sheet, and random coil structures has its own characteristic shape of CD spectrum (see figure 2.5). Wu et al. [5] developed a new method of oriented circular dichroism (OCD) to determine the orientation of α-helices relative to the plane of the membrane. They directly mixed the peptide with lipid and made uniformly-aligned multilayers of peptide embedded membrane. By using this method, not only the conformation but also the orientation of the peptide can be determined as the result of binding to the lipid membrane.

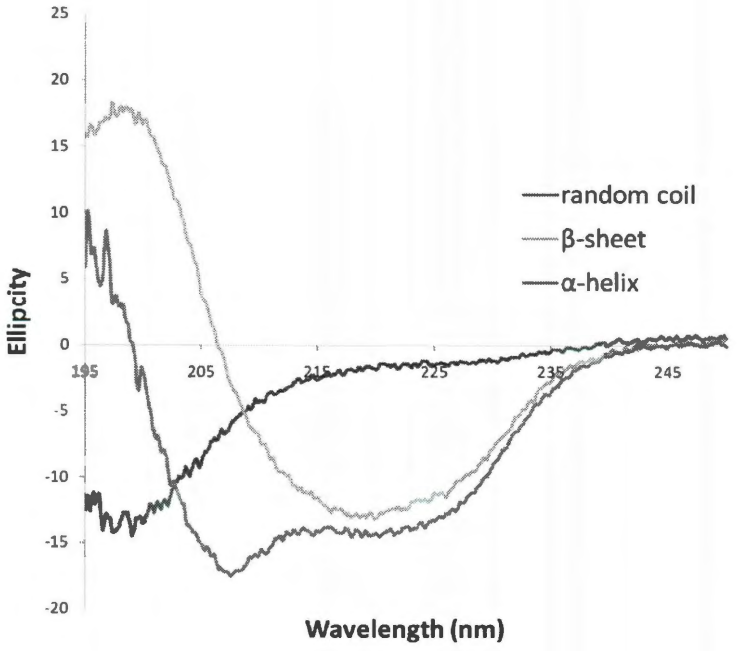

Figure 2-5 CD spectra for secondary structures of peptides

2.2.2. Sample preparation and experiment setup

Sample preparation of CD followed exactly the same protocol as x-ray sample, except the substrates were changed to quartz plates instead of silicon wafers. CD samples also had less lipid when amount compared to x-ray samples, since lipid absorbed the incident light significantly below ~200 nm and thus increased the noise.

Spectra were measured in a Jasco (Tokyo, Japan) J-810 spectropolarimeter. The substrates were mounted perpendicular to the incident light in a humidity-temperature controlled chamber. The spectra from 190 nm to 250 nm were measured at different temperature or humidity. The background spectrum for each

sample was the spectrum for the same amount of lipid on the same substrate. After the background correction, the spectra of different P/L were normalized by the concentration of peptide in each sample.

Chapter 3

The bound states of amphipathic drugs in lipid bilayers: study of curcumin

3.1. Introduction

The lipid matrix, or the lipid bilayer, of cell membranes is a natural binding site for amphipathic molecules, including proteins, organic molecules such as drugs, detergents and others. However the biological effect of drug-membrane interactions [51] is unclear. For example, if drugs must diffuse through membranes in order to bind to specific protein targets, then binding to the membrane may cause a secondary effect distinct from that of the drug-protein interaction. Whether the membrane-binding produces desirable or undesirable effects, it is important to understand the effect of drug binding to lipid bilayers, since there are concrete examples that a change of the physical state of the lipid bilayer can affect the

functions of embedded proteins[1, 2]. It is well recognized that amphipathic molecules can bind to the membrane-water interface or intercalate into the nonpolar chain region[51]. As far as we know, the energetics of these two binding states of drugs and their effects on lipid bilayers have not been analyzed. In this paper we show that the dual measurements of both the membrane thickness and the membrane area changes due to drug binding allow such analyses.

Curcumin is an example of amphipathic drugs that bind to cell membranes[19, 20]. This yellow spice has long been reported to be biologically active, most often as having anti-inflammatory, anti-angiogenic, antioxidant, wound healing and anti-cancer effects[47, 52]. However its efficacy has been a subject of controversy[53], and its mechanism of action remains obscure. In particular, curcumin modulates the function and expression of a wide range of structurally and functionally unrelated membrane proteins, which suggests a possibility that curcumin might alter membrane protein function by modulating the properties of the host lipid bilayer[1]. In a recent paper we reported a nonlinear thinning effect on lipid bilayers caused by curcumin binding[33]. This was found by an X-ray diffraction measurement of the bilayer thickness as a function of curcumin content. The thinning result allowed us to explain the effect of curcumin on the lifetime of the gramicidin single channel[1, 33]. To gain a more complete understanding of the curcumin-membrane interactions, here we report a systematic measurement of the responses of individual giant unilamellar vesicles (GUVs) to the binding of curcumin from solution. The GUV experiment measured the change of the membrane area due to curcumin binding, to be compared with the corresponding membrane

thinning. From these two results we are able to deduce the binding states of curcumin in lipid bilayers. We construct a simple two-state model assuming that there are two distinct bound states for curcumin; one at the interface and another in the hydrocarbon chain region. The energy of the interfacial binding state includes the elastic energy of the membrane thinning. This simple model reproduces the experimental data.

The choice of the two experimental methods was in part motivated by the desire to answer these questions: Is an effect on membranes measured in a multilamellar preparation, as used in X-ray diffraction experiment, reproducible by a measurement on a single membrane in solution, as in GUV experiment? Are the two measurements quantitatively compatible? These questions are affirmatively answered by the agreement between the membrane thinning measured in multilamellae and the membrane area increase measured in GUVs. The quantitative analysis of these two sets of data provides an example for applying similar analyses to other membrane-binding molecules.

We found the binding behavior of curcumin following the same pattern shown by more hydrophilic amphipathic peptides. This implies that the binding states of curcumin are typical of amphipathic drugs.

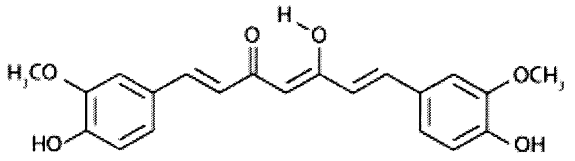

Figure 3-1 Chemical structure of curcumin

3.2. Material and Methods

3.2.1. Materials

1,2-dioleoyl-*sn*-glycero-3-phosphocholine (DOPC) and 1,2-dioleoyl-sn-glycero-3-phosphoethanolamine-N-(lissamine rhodamine B sulfonyl) (abbreviated as Rh-DOPE) were purchased from Avanti Polar Lipids (Alabaster, AL). 3,3'-dioctadecyloxacarbocyanine perchlorate (abbreviated as DiO) was from Invitrogen (Carlsbad, CA). Curcumin (product number 28260), HEPES (product number H3375), bovine serum albumin (BSA) (product number A9418) and dimethyl sulfoxide (DMSO) were from Sigma-Aldrich (St. Louis, MO). All materials were used as delivered.

3.2.2. Sample Preparation

Curcumin (Figure 3.1) can be dissolved in water by first dissolving in DMSO. But the water solubility and the molecular stability of curcumin is strongly pH-dependent. The aqueous solubility decreases as pH decreases below 7, but the molecule degrades as pH increases above 7 [54]. Therefore a buffer solution of 20

mM HEPES was used to maintain the solution at pH 7. Optical spectroscopy was employed to calibrate the curcumin concentration and to monitor its molecular integrity [54]. In our previous study[33], we showed that at pH 7 the solubility limit for curcumin is about 25 μM. Curcumin was first dissolved in DMSO at 19 mM and then diluted with sucrose/HEPES solution to desired concentrations (<25 μM). Almost all previous GUV studies by the aspiration method were performed in 100-200 mM sucrose solutions [15, 55]. The curcumin solutions were kept in the dark as much as possible because curcumin is sensitive to light [56]. Also, curcumin adsorbed to the walls of containers, often 5-20%, depending on the material and the surface to volume ratio of the container. The loss of curcumin to the container wall at each step of solution transfer was carefully monitored by a spectral measurement [33]. We also took into account the fraction of curcumin adhered to the wall of the experimental chamber. We estimated the uncertainty of the curcumin concentration in the experimental chamber to be ~±10%.

3.2.3. GUV Experiment

We used two chamber method described in chapter 1.5. If the observation chamber contained a sucrose/HEPES (without curcumin) solution isotonic to 200 mM sucrose solution, the GUV remained unchanged, as expected. When curcumin was present in the solution of the observation chamber, the vesicle projection in the micropipette immediately increased its length and reached an equilibrium length within ~100s. Thereafter the projection length remained unchanged. The video image of the process was captured by a Nikon NS-5 MC camera (Figure 3.2). The

response of GUVs indicated that the outer and inner leaflets of the bilayers changed their areas together, implying that the same amount of curcumin bound to both leaflets; otherwise there would be an areal imbalance between the outer and inner leaflets which was not observed. On a number of runs, we used glucose instead of sucrose in the observation chamber in order to measure the phase contrast between the inside and outside of the GUV, and detected no change in the contrast during the entire process. This implied that there was no content exchange between the inside and outside of the GUV. We assumed that there was no change in the vesicle volume during curcumin binding. Then the increase of the vesicle projection in the micropipette can be translated to an increase in the membrane area by the geometric relation[57] $\Delta A = 2\pi R_p(1 - R_p / R_v)\Delta L_p$, where R_p and R_v are radii of the pipette and vesicle; L_p is the projection length (Figure 3.2). All the values of R_p, R_v and L_p were carefully measured and analyzed by using the Nikon NIS-Elements BR 2.30 software. To normalize the area changes for vesicles of different sizes, ΔL_p was converted to the fractional change of vesicle area $\Delta A/A$ plotted as a function of time (see below). To minimize the osmolality change due to evaporation, solutions in the chambers were changed frequently (~every 15 min).

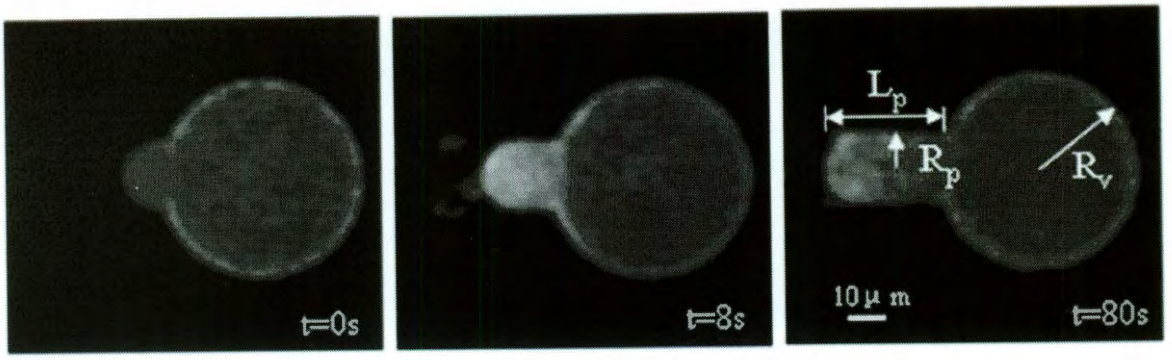

Figure 3-2 Sequential videomicrographs of a GUV held under a small constant pressure exposed to 8.96 μM curcumin solution. L_p, R_p and R_v are indicated

Effect of DMSO. DMSO was used to solubilize curcumin in an aqueous solution of pH 7. The amount of DMSO used was proportional to the curcumin concentration. The highest curcumin concentration in our experiment was 13.5 μM (after the calibration for the losses to the container walls mentioned above) and its corresponding DMSO content was 0.16% (or 20 mM). DMSO has been shown to have no effect on lipid bilayer properties at such low concentrations. Longo et al. [55] showed that in the presence of 0.5% DMSO, the rupture tensions for lipid vesicles were the same as without DMSO. Hwang et al. [58] showed that DMSO at 0.8% did not affect the single channel lifetime of gramicidin. However we found that DMSO presented a problem for the osmotic balance in a GUV experiment. For example when we used a solution of sucrose/HEPES and 0.16% DMSO in the observation chamber that was measured to have the same osmolality as the 200 mM sucrose solution inside the GUV, we found the vesicle projection length diminished and the GUV burst, indicating an tonicity imbalance. Apparently the GUV swelled, since, at constant vesicle surface area, the vesicle volume change ΔV is related to the

projection length change by $\Delta V = -\pi R_p (R_v - R_p)\Delta L_p$. The most reasonable explanation is that the lipid bilayer is permeable to DMSO; therefore DMSO did not contribute to the tonicity (the effective osmolality with respect to the membrane). This made the osmotic pressure outside the GUV lower than inside, hence swelling. However, if we added 0.16% DMSO to a sucrose/HEPES solution which was already isotonic to 200 mM sucrose solution inside the GUV, and used it in the observation chamber, the vesicle projection length would increase slightly, indicating an outflow of water from the GUV. Apparently DMSO contributed slightly to the tonicity, not entirely consistent with DMSO being a permeant solute. This was also observed by Longo et al [55].

Curcumin experiment. Since the interaction between DMSO and curcumin might alter the tonicity contribution by DMSO, we were not confident that the effect of DMSO is correctable by a background subtraction [55]. Therefore, we performed the curcumin experiment in two ways to measure the upper and lower limits of the curcumin effect on the lipid bilayer. In the first experiment, the observation chamber contained sucrose/HEPES/curcumin/DMSO solution of various curcumin concentrations. Each solution was measured to have the same osmolality as 200 mM sucrose solution. The GUV response was recorded and plotted as $\Delta A/A$ vs. time in Figure 3.3. In this case, the vesicle volume would somewhat increase and make the ΔL_p somewhat smaller than the pure curcumin effect. Therefore the measurement represented a lower limit of the curcumin effect.

In the second experiment, the observation chamber contained a sucrose/HEPES solution that was measured to have the same osmolality as 200 mM sucrose solution. Then the appropriate amount of curcumin/DMSO was added to obtain the desired curcumin concentration. The GUV response was recorded and plotted as $\Delta A/A$ vs. time in Figure 3.3. In this case, the vesicle volume would somewhat decrease and make the ΔL_p somewhat longer than the pure curcumin effect. Therefore the measurement represented an upper limit of the curcumin effect.

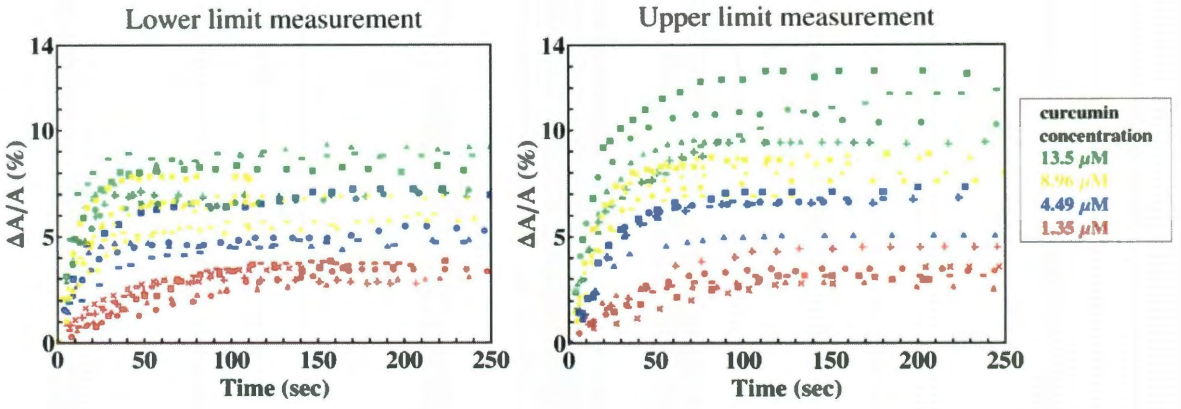

Figure 3-33 Time sequence of fractional area changes of individual DOPC GUVs exposed to various concentrations of curcumin: 13.5 μM (green), 8.96 μM (yellow), 4.49 μM (blue), 1.35 μM (red). Different symbols represent different runs. (Left) For each run, the osmolality of the solution in the observation chamber, including curcumin/DMSO, was made the same as the 200 mM sucrose solution inside the GUV. (Right) For each run, the curcumin/DMSO solution was added to a sucrose/HEPES solution that had the same osmolality as the 200 mM sucrose solution inside the GUV.

3.3. Analysis and Discussion

A lipid bilayer responds to molecular binding by changing its thickness and its surface area. If an amphipathic molecule binds to the water-membrane interface, it necessarily inserts between lipid headgroups and causes an interfacial area expansion. An interfacial area expansion will cause membrane thinning, due to the very small volume compressibility of hydrocarbon chains [59]. The relation between the thickness change and the area change due to an interfacial molecular binding is simply $-\Delta h / h = \Delta A / A$, where h is the thickness of the hydrocarbon region and A the surface area of the lipid bilayer. On the other hand, if a molecule intercalates into the hydrocarbon chain region, it would certainly expand the membrane area, but it might not affect the membrane thickness.

(1) Membrane Thinning

The thickness of a phospholipid bilayer can be measured by its phosphate-to-phosphate distance (*PtP*) across the bilayer. The *PtP* of DOPC bilayers was previously measured by X-ray diffraction as a function of its curcumin content [33] and is reproduced in Figure 3.4. The data shows that the initial binding of curcumin has a large thinning effect up to the bound curcumin to lipid ratio ~ 0.032, but the effect becomes considerably smaller upon further binding. Qualitatively, this indicates that there is one low-energy binding state that causes thinning, and a higher energy binding state that has little thinning effect.

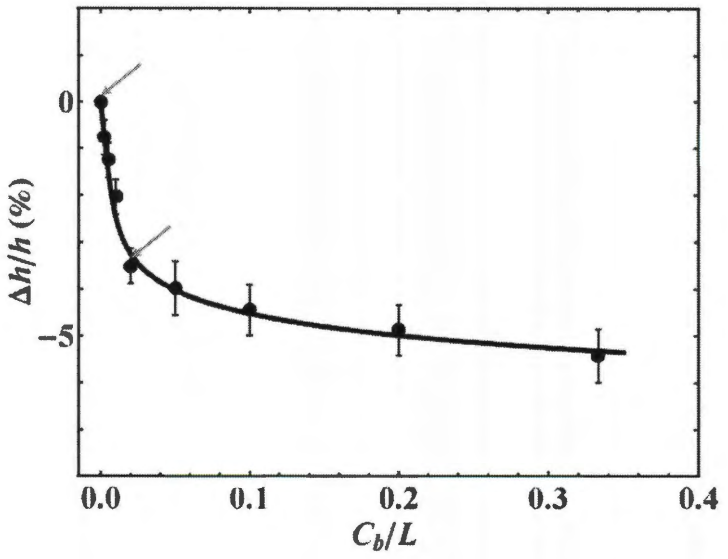

Figure 3-4 Fractional thickness change of DOPC bilayer as a function of curcumin content, expressed as bound curcumin to lipid molar ratio C_b/L. The data are from Hung et al.[33]. Two arrows indicate the points that were used to determine two constants *a* and *b* in the model equation Eq. (3.3). The solid curve is the model prediction $\Delta h/h$ (Eq. 3.4) from the solution of Eq. (3.3).

We consider the low energy state first. To the first few amphipathic molecules approaching a lipid bilayer, the interface, rather than the non-polar chain region, is expected to be the lowest energy binding site. This has been proven for amphipathic peptides (mostly antimicrobial peptides [60]) which in all cases initially bind to the interface of lipid bilayers [8, 61-63] by hydrophobic interactions [64]. We will call this interfacial binding the S state and denote the area expansion per molecule by A_S. We know that to a very good approximation, the thickness of the hydrocarbon region is $h \approx PtP - 10\,\text{Å}$, or *PtP* minus twice the length of the glycerol region (from the phosphate to the first methylene of the hydrocarbon chains), for

pure lipid bilayers as well as for bilayers containing bound molecules[33]. Let C_b be the total number of curcumin molecules bound to a bilayer of L lipid molecules. If the number of curcumin molecules in the S state is $N(S)$, then we have the membrane thinning due to the curcumin molecules bound to the S state:

$$-\Delta h/h = \Delta A/A = A_S N(S)/A_L L, \tag{3.1}$$

where A_L is the cross section area for each lipid molecule in the bilayer.

Another possible binding site is the interior of the hydrocarbon chain region, into which a curcumin may insert and stay bound. We assume that this is the higher energy state (the I state) for curcumin. We assume that the I state will cause a membrane area expansion, A_I per molecule, but will not cause membrane thinning. Then the membrane thinning by curcumin binding is given by Eq. (3.1).

To express $N(S)/L$ in terms of the curcumin-lipid ratio C_b/L, we will need to know the energy difference between the S state and the I state. And we believe that the crucial idea is that the elastic energy of membrane thinning must be included in the energy level of the S state. This energy can be derived as follows[65]: A fractional area expansion $\Delta A/A$ is a strain whose corresponding stress is the monolayer tension $\sigma = (K_a/2)\Delta A/A$, where K_a is the bilayer stretch coefficient[15]. The binding of $N(S)$ curcumin molecules, causes a change in the energy $\delta E = -\varepsilon_S^o \delta N(S) + \sigma A_S \delta N(S)$, where the first term is the intrinsic binding energy, $-\varepsilon_S^o$, presumably due to hydrophobic interaction, and the second term is the

elasticity energy of area stretching (or membrane thinning). Combining this relation with Eq. (3.1), we obtain the energy level for the S state[65]

$$E_S = -\varepsilon_S^o + (K_a/2)(A_S^2/A_L)N(S)/L \tag{3.2}$$

The simplest choice for the energy level of the I state is a constant $E_I = -\varepsilon_I^o$. Then the ratio of the numbers of curcumin molecules in the S state and in the I state is $N(S)/N(I) = \exp[-\beta(E_S - E_I)]$, with $\beta^{-1} = k_B T$, the Boltzmann constant times the temperature. From this we obtain the equation for the ratio of curcumin molecules in the S state to all curcumin molecules associated with the membrane, $\alpha \equiv N(S)/C_b$ or for $x \equiv \alpha(C_b/L)$:

$$\alpha = \frac{1}{2}\left[1 - \tanh\left(b\frac{C_b}{L}\alpha - a\right)\right] \text{ or } \frac{x}{C_b/L} = \frac{1}{2}[1 - \tanh(bx - a)] \tag{3.3}$$

Where we have introduce $C_b = N(S) + N(I)$, $a = \beta(\varepsilon_S^o - \varepsilon_I^o)/2$ and $b = \beta K_a(A_S^2/A_L)/4$. Note that the only unknown in b is A_S. $K_a \cong 243$mN/m has been measured[15]. $A_L = 73.4$ Å^2 is calculated from the h of pure DOPC (26.8 Å obtained from *PtP=36.8* Å[33]) and its chain volume per lipid (984 Å^3[66]).

The membrane thinning data $\Delta h/h$ vs. C_b/L is interpreted as x vs. C_b/L by rewriting Eq. (3.1) as

$$-\Delta h/h = (A_S/A_L)(C_b/L)\alpha = (A_S/A_L)x. \tag{3.4}$$

Thus we can directly compare the solution of our model, Eq. (3.3), with the data. We first select two points in the data to determine the two unknown constants *a* and *b*. We assume that the initial binding is to the S state, i.e., $\alpha \to 1$ as $C_b / L \to 0$. So the initial slope of *h/h* vs. C_b/L equals to A_S / A_L (this required a continuous curve fitting to the data). This gives $A_S = 240 Å^2$, and $b = 233$. Next we find the point of intersection between the line $x = (1/2) C_b / L$ and the data curve *x* vs. C_b/L. At this point of intersection, called $x_{1/2}$, the relation $b x_{1/2} = a$ is satisfied (see Eq. 3). From the value of intersection $x_{1/2}$ = 0.01 and the value of *b*, we obtained $a = 2.3$.

With *a* and *b* determined, we then solved Eq. (3.3) for α or *x*, and used Eq. (3.4) to reproduce $\Delta h/h$ as a function of C_b/L. The solution is compared with the data in Figure 3.4--the agreement of the model with data is excellent.

We note that if we were to assume that E_S is a constant, not including the elastic energy of membrane thinning, then α would be a constant and *x* would be proportional to C_b/L. Then by Eq (4), $\Delta h/h$ vs. C_b/L would be a straight line, strongly disagreeing with the data.

(2) Membrane Area Expansion

Our model also predicts what to expect from the membrane area expansion experiment. Since the initial membrane thinning was due to curcumin initially bound mostly to the S state, the area expansion should be $\Delta A / A \sim -\Delta h / h$ for the low C_b/L region. As the binding to the I state increased, the area expansion $\Delta A / A$ should

become larger than $-\Delta h/h$. This is because in our model we assume that curcumin in the I state would cause area expansion but no thickness change.

In each of our GUV experiments, the vesicle projection inside the micropipette was observed to reach an equilibrium length. From this equilibrium length we calculated the final fractional area expansion $\Delta A/A$ as a function of curcumin concentration in solution. To compare with the membrane thinning measurement, we will need to know the amount of curcumin bound to the GUV at each curcumin concentration. This was achieved by using the partition coefficient from solution to lipid bilayers measured previously by isothermal titration calorimetry[33]: $C_b / L = KC_f$, K = 2.4 × 10^4 M^{-1}, where C_f is the curcumin concentration in solution. In Figure 3.5, $\Delta A/A$ was plotted as a function of C_b/L for the upper and lower limit measurements. The bottom curve shows the equivalent fractional area expansion $(\Delta A/A)_{\Delta h/h} = -\Delta h/h$ from the fractional thinning data shown in Figure 3.4. Since $(\Delta A/A)_{\Delta h/h}$ does not include the area expansion due to the curcumins in the I state, it is smaller than the total area expansion that falls somewhere between the upper and lower limits.

Note that the curcumin to lipid ratios C_b/L of the X-ray data (the bottom curve of Figure 3.5) were accurate because the curcumin concentrations in the experimental samples for X-ray diffraction were directly measured spectroscopically[33]. In contrast the C_b/L for the GUV experiment had an uncertainty of ~ ±10% (due to curcumin's tendency to adsorb to the containers' walls; see sample preparation). This uncertainty in concentration made the GUV

experiment unsuitable in low C_b/L region (<0.03) (due to the very large slope in $\Delta A/A$ vs. C_b/L). Nevertheless the GUV results presented in Figure 3.5 unambiguously confirmed the two-state model described in the last section.

The fractional area expansion by the two-state model is given by

$$\begin{aligned}\Delta A/A &= (A_S/A_L)(C_b/L)\alpha + (A_I/A_L)(C_b/L)(1-\alpha) \\ &= (\Delta A/A)_{\Delta h/h} + (A_I/A_L)(C_b/L)(1-\alpha)\end{aligned} \tag{3.5}$$

Since α is already determined by Eq. (3.3), the model allows only one undetermined parameter A_I for the GUV results. In Figure 3.5, we used Eq. (3.5) and different values of A_I (12 Å^2 and 7 Å^2, respectively) to fit the upper and lower limits of the curcumin effect (the top two curves). The real effect is in between these two limits. It is clear that the measured membrane area expansion by curcumin binding is consistent with the two-state model. Eq. (3.5) predicted that at small values of C_b/L where α is close to 1 (e.g., C_b/L= 0.032), the fractional area expansion of GUV should be close to the value of $(\Delta A/A)_{\Delta h/h}$ and at larger values of C_b/L (> 0.032) where α is significantly smaller than 1, the fractional area expansion of GUV should be larger than the value of $(\Delta A/A)_{\Delta h/h}$. Both features were born out by the GUV experiment. The agreement also strongly supports the proposed sites for the two states, one on the interface and another inserted in the hydrocarbon region. The interfacial binding both thins the membrane and expands the area, while the insertion among the chains expands the area but has little thinning effect.

The membrane area expansion per curcumin is A_S ~ 330 Å^2 for the S state, and A_I between 6 Å^2 and 12 Å^2 for the I state. These values are not to be interpreted

as the physical dimensions of curcumin molecule. (The largest and smallest cross sections of curcumin molecular crystal are roughly 122 Å^2 and 22 Å^2, respectively [67].) A lipid bilayer is not an inert matrix to which a molecule binds. Rather it is a complex assembly of flexible lipid molecules and water molecules. When a molecule binds to the lipid bilayer, the molecule might bring in additional water molecules or release some water molecules associated with the bilayer before binding. Such a redistribution of water molecules would affect of the value of area expansion by molecular binding. For example, the helical lengthwise cross section of melittin is about 400 Å^2, but the measured A_S for melittin is only 175-246 Å^2 depending on the lipid compositions [65].

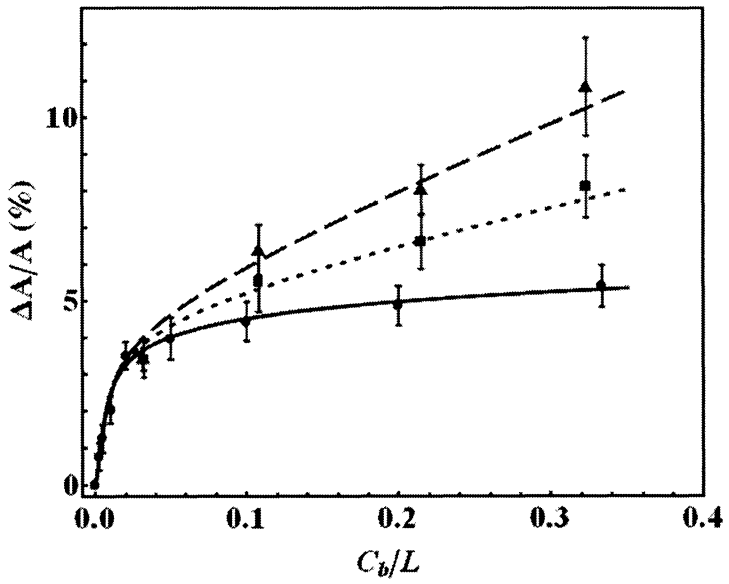

Figure 3-5 Fractional area expansion measured by GUV experiments (squares and triangles) compared with the values corresponding to the membrane thinning measurement by X-ray (solid circles). The square and triangle data

are the asymptotic values $\Delta A/A$ taken from the lower and upper limit measurements in Figure 3, respectively; the error bars represent the standard deviations. The real area expansion effect of curcumin falls between the upper and lower limits. The curves are the results from the model as explained in the text.

Chapter 4

Interaction of Tea Catechin (–)-Epigallocatechin Gallate with Lipid Bilayers

4.1. Introduction

Like ginseng and curry, green tea is popularly believed to have health benefits. Great tea extracts, particularly catechins have been reported to have a wide variety of biological activities (see references in [68]). Because many of these activities seemed to affect membrane-dependent cellular processes [21], such as cell signaling, cell cycle, arachidonic acid metabolism and mitochondrial functionality, there have been a long series of reports on catechin-membrane interactions[21-30]. Earlier investigations [21-28] emonstrated that tea catechins bound to lipid bilayers, caused aggregation of lipid vesicles, and leaked contents from a suspension of

vesicles. A more extensive study was done recently by Tamba et al. [29] who concentrated on a major catechin from tea extract, (—)-Epigallocatechin gallate (EGCg). Noting that in an earlier study with magainin [69] they had demonstrated the advantage of observing individual giant unilamellar vesicles (GUVs) over measuring collective responses from a suspension of vesicles, Tamba et al. observed the effect of EGCg on individual GUVs in several ways. They found that EGCg had the effects of 1) causing shape change of GUVs, 2) inducing aggregation of vesicles, and 3) causing GUVs to burst through a large hole. They suggested that the bursting effect is a possible mechanism for catchins' antibacterial activity. They attributed all these activities to the binding of EGCg exclusively to the outer leaflet of the GUV membranes.

The methods used by Tamba et al. required relatively high concentrations of EGCg. Below 30 μM, EGCg showed the effect of shape change and aggregation of GUVs, but no leakage. The bursting effect was seen only for concentrations above 30 μM. It is difficult to discern the molecular mechanism of EGCg from such drastic effects on membranes. Here we will study the effect of EGCg on membranes by using a different GUV method which is more sensitive than the methods used by Tamba et al. and can measure the effect at lower EGCg concentrations. We believe that low concentration phenomena are more likely to reveal the molecular mechanism.

We used the micropipette aspiration method [57] to monitor the area and volume change of a GUV exposed to EGCg in solution. We also measured the effect of EGCg on the thickness of lipid bilayers by x-ray diffraction. We have previously used

the combination of these methods to study other membrane-active molecules [31, 32]. We found that the molecular effect of EGCg on membranes is best understood by comparing its action with membrane-active molecules whose actions are understood, such as pore-forming peptides [31], the turmeric (curry) extract curcumin [32, 33], and detergents. The comparative studies led us to conclude that EGCg has a mild detergent-like effect. At concentrations below 10 μM, it binds to lipid bilayers but also slowly dissolves the lipid molecules from the bilayer without making pores. We did not observe any effect indicating that EGCg binds exclusively to the outer leaflet of GUV membranes. Thus the effect of EGCg on membranes is somewhat unique. Its binding effect (i.e., the membrane area expansion effect) is one order of magnitude smaller than curcumin, and its lipid-solubilization effect is also different from detergents.

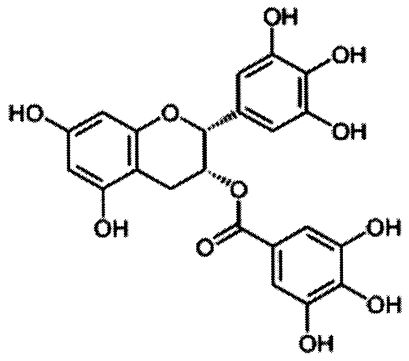

Figure 4-1 Chemical structure of EGCg.

4.2. Material and Methods

4.2.1. Materials

( )-Epigallocatechin gallate (EGCg) (product number E4143), HEPES (product number H3375), Triton X100 (product number T8787) and bovine serum albumin (BSA) (product number A9418) were purchased from Sigma-Aldrich (St. Louis, MO). 1,2-dieicosenoyl-*sn*-glycero-3-phosphocholine (Di 20:1PC), 1,2-dioleoyl-*sn*-glycero-3-phosphocholine (DOPC), 1-palmitoyl-2-oleoyl-*sn*-glycero-3-phosphocholine (POPC), chicken egg L-α-phosphatidylcholine 95% (EggPC) and 1,2-dioleoyl-sn-glycero-3-phosphoethanolamine-N-(Lissamine Rhodamine B Sulfonyl) (Rh-DOPE) were purchased from Avanti Polar Lipids (Alabaster, AL). Magainin 2-amide was purchased from GenScript Corporation (Piscataway, NJ). Polyethylene glycol (PEG400) was purchased from Merk Co. (Hohenfrunn, Germany). All materials were used as delivered.

4.2.2. X-ray lamellar diffraction

We followed the same procedure described in chapter 2 to perform the x-ray diffraction data.

4.2.3. Isothermal titration calorimetry (ITC).

EGCg was first dissolved in a buffer solution of 20mM HEPES (pH7.4) and 150mM NaCl. Monodispersed large unilamellar vesicles (LUVs) of DOPC with diameter ~ 100nm were made by an extruder. ITC was performed by injecting a series of aliquots (volume10 μL) from an LUV suspension into an EGCg solution of concentration E_t at 25° C. The heat flow for EGCg binding to the vesicles was measured by a high-sensitivity ITC instrument (MicroCal LLC, Northampton, MA) with a reaction cell volume of 1.4144 ml. Prior to ITC experiment, the EGCg solution was put in a vacuum degas system (provide by MicroCal) to remove the possible air bubbles. The data of heat flow were acquired by computer software developed by MicroCal. The solution in the reaction cell was continually stirred during the measurement. The reaction heat for each injection was determined by integration of the heat flow tracing. In a control experiment, the corresponding LUVs were injected into a buffer solution in reaction cell. The resultant heat (usually called dilution heat) for each injection was subtracted from the corresponding reaction heat of LUVs injected into the EGCg solution. The reaction heat per injection thus obtained was that for EGCg binding to lipid vesicles. We have performed the following ITC measurements. EGCg solutions of concentration (E_t) 10, 50, 100 and 300 μM were each titrated by DOPC LUVs of 4mM lipid concentration. The data reduction described below was similar to that employed in Hung et al.[33] , but with a small modification.

Denote the reaction heat for the i^{th} injection as h_i. The cumulative heat up to the k^{th} injection is defined as,

$$h^{(k)} = \sum_{i=1}^{k} h_i \tag{4.1}$$

The cumulative heat will be saturated once all the EGCg molecules in the reaction cell are bound to lipid vesicles. Denote the saturated cumulative heat as $h^{(sat)}$ and the initial molar concentration of EGCg molecules in the reaction cell as E_t, then the molar fraction of the vesicle-bound EGCg up to the k[th] injection is,

$$E^{(k)}/(\eta^{(k)}E_t) = h^{(k)}/h^{(sat)} \tag{4.2}$$

where the dilution factor $\eta^{(k)}$ is defined as follows. The injection of each LUV aliquot increased the volume by δv. The volume of the solution in the reaction cell up to the k[th] injection is $V_{cell}^{(k)} = V_{cell}^{o} + k\delta v$, where V_{cell}^{o} is the original volume of solution in the reaction cell. The dilution factor is $\eta^{(k)} = V_{cell}^{o}/V_{cell}^{(k)}$. The lipid concentration in the reaction cell up to the k[th] injection is

$$L^{(k)} = L_o(k\delta v/V_{cell}^{(k)}) \tag{4.3}$$

where L_o is the molar concentration of lipid injected into the reaction cell. Then the partition coefficient K is defined by

$$E^{(k)}/(\eta^{(k)}E_t) = KL^{(k)}/(1+KL^{(k)}) \text{ or } E^{(k)}/L^{(k)} = KE_f^{(k)} \tag{4.4}$$

where $E_f^{(k)} = \eta^{(k)}E_t - E^{(k)}$ is the concentration of EGCg dissolved in solution at the end of k[th] injection. Combining Eqs.(4.2) and (4.4), one obtains

$$h^{(k)} = h^{(sat)} KL^{(k)} / (1 + KL^{(k)}) \tag{4.5}$$

We used Eq.(5) to fit the data of $h^{(k)}$ vs $L^{(k)}$, from which K and $h^{(sat)}$ were obtained. The binding enthalpy per mole of EGCg can be obtained by

$$\Delta H = h^{(sat)} / (E_t V^o_{cell}). \tag{4.6}$$

4.2.4. GUV experiment

EGCg was first dissolved in 10mM HEPES (pH 7.4) at 10mM and then diluted with a HEPES/sucrose solution to desired concentrations.Triton X100 and magainin2 were first dissolved in distilled water at 10mM and then diluted with sucrose solution to desired concentration.

GUVs were produced by following the protocol in chapter 1.2. GUV experiments were performed in a setup described in chapter 1.5.

An aspirated GUV consisted of a cylindrical protrusion (length L_p) in the micropipette (radius R_p) connected to the spherical vesicle (radius R_v) at the tip of the micropipette (see Figure 4.2). The protrusion length would change if there was a change in the surface area A and/or the volume V of the GUV, as a result of interaction with EGCg.

Control experiment was performed with the observation chamber filled with 190mM sucrose and 10mM HEPES solution which was isotonic to the sucrose solution in the control chamber. After the GUV was transferred to the observation

chamber, the length of the aspirated protrusion reminded unchanged for 6 minutes, as expected. In order to minimize the osmolality change due to evaporation, each run of the experiment were kept within 6 minutes and the solutions were changed after each run.

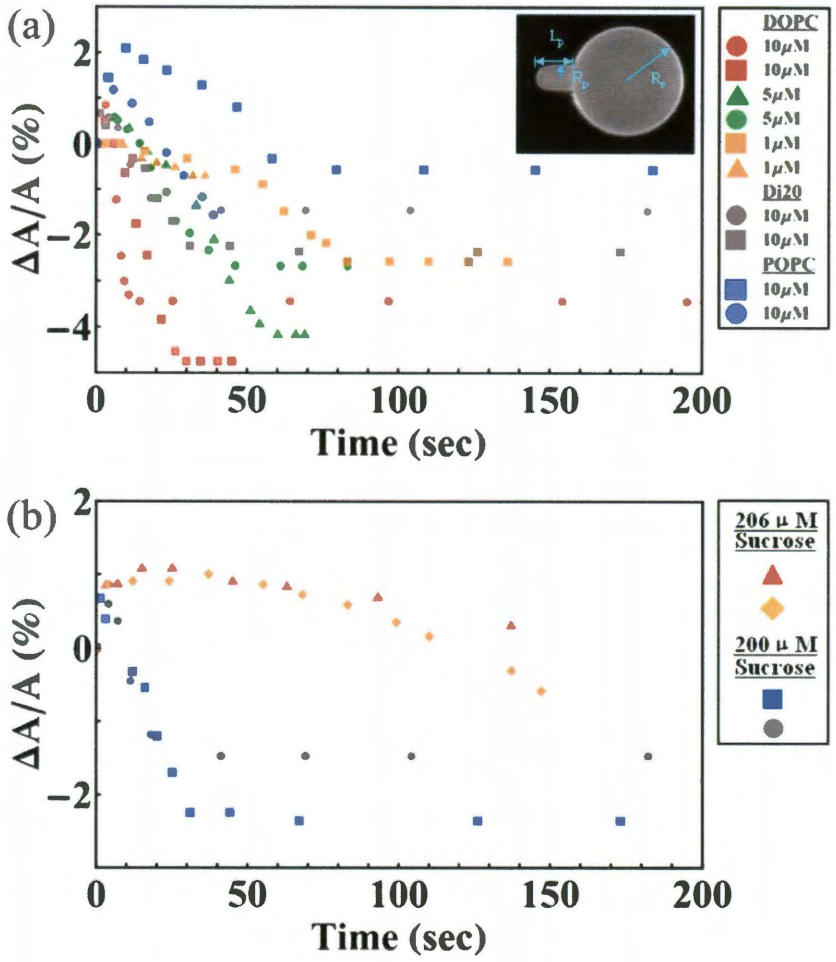

Figure 4-2 (a) Time sequence of fractional area changes *ΔA/A* of individual GUVs exposed to various concentrations of EGCg. Different symbols represent different runs: the lipid of GUV and the EGCg concentration are given in the side panel. For each run, the osmolality of the solution in the observation chamber, including the buffer and EGCg, was made the same as the 200 mM sucrose solution inside the GUV. (b) Comparison of runs when the solution in the observation chamber had osmolality 206 mM and the corresponding runs

when the osmolality was 200 mM. The lipid was di20:1PC, EGCg was 10 μM, and the sucrose solution inside the GUV was 200 mM. Inset in (a) shows the definitions for L_p, R_p and R_v.

4.2.5. Turbidity measurement

A suspension of lipid vesicles was prepared for turbidity measurement. From a stock solution of DOPC (25mg of lipid in 1ml chloroform), 2.5mg of DOPC was placed in a glass vial and blow-dried with nitrogen for 30 minutes. Three samples were prepared by adding 4ml of HEPES or EGCg and HEPES or Triton X-100 solutions into a glass vial, making the lipid's final concentration 8mM, and the concentration of EGCg or Triton 10mM. The glass vial was put in a sonicator for 10 min to form vesicles. The vesicle suspension was immediately transferred to a cuvette for a spectrophotometer (Shimadzu UV-2101PC). For background subtraction, the same solution without lipid was used for each sample.

4.3. RESULT

4.3.1. GUV experiment

The general response of a GUV exposed to an isotonic EGCg/HEPES/sucrose solution was that the protrusion length L_p initially increased slightly and then within seconds decreased until diminished. In about 50% of the cases, the GUV ruptured after the protrusion diminished. The rupture was not correlated with the concentration of EGCg. From the geometry of an aspirated GUV, the change of the

surface area A is related to the changes of L_p and the GUV radius R_v (see Figure 4.2) by $\Delta A = 2\pi R_p \Delta L_p + 8\pi R_v \Delta R_v$, and the change of the GUV volume V by $\Delta V = \pi R_p^2 \Delta L_p + 4\pi R_v^2 \Delta R_v$ [57]. In general the changes of GUV radius ΔR_v were too small to be measured accurately. However since the inside and outside of the GUVs were always isotonic, the change of volume should be zero. This will be further demonstrated by comparative GUV experiments with other types of membrane-active molecules below. Under the condition $\Delta V = 0$, ΔL_p is directly proportional to ΔA: $\Delta A = 2\pi R_p(1 - L_p/R_v)\Delta L_p$. From the recorded video images, we measure ΔL_p as a function of time by using the Nikon NIS-Elements BR 2.30 software. The responses of GUVs of different sizes can be compared by their $\Delta A/A$ as a function of time, as shown in Figure 4.2A. The data include GUVs of DOPC, POPC, and Di20:1PC exposed to EGCg of concentrations ranging from 1 to 10 μM.

4.3.2. X-ray diffraction

Lipid-EGCg mixtures formed excellent bilayers as shown by their X-ray lamellar diffraction patterns and their reconstructed electron density profiles. The example of EGCg-DOPC mixtures in a series of mixing molar ratios (E/L) is shown in Figure 4.3. The results of EGCg-POPC, and EGCg-EggPC mixtures were similar in quality. In such bilayers, EGCg was in its equilibrium bound state. The peaks of the electron density profile are the positions of the phosphate groups on the surfaces of the bilayer. Hence the peak-to-peak distance (PtP) across the bilayer is a good measure of the bilayer thickness. The presence of EGCg apparently caused

membrane thinning. The thinning is linearly proportional to the *E/L* for all three lipids measured here (Figure 4.4).

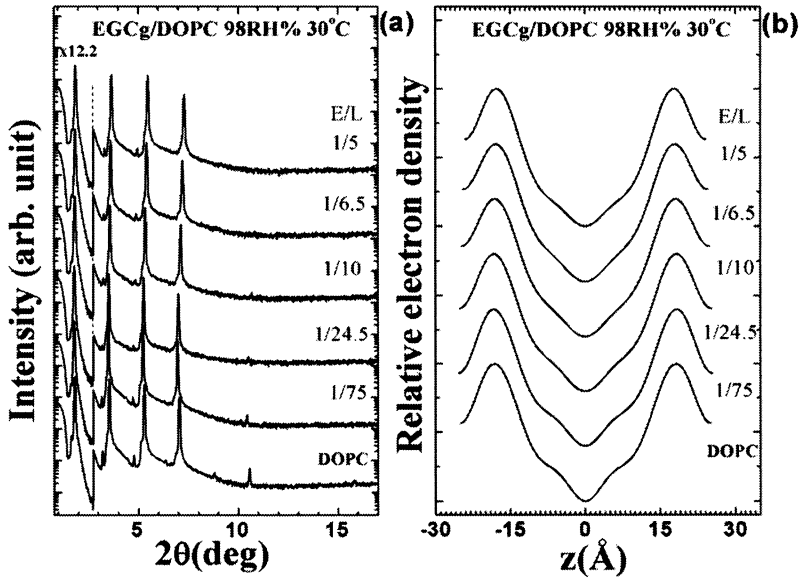

Figure 4-3 (a) X-ray diffraction patterns for a series of EGCg-DOPC mixtures of molar ratios *E/L* in aligned multiple bilayers. An attenuator was used to prevent the first order Bragg peak from saturating the detector. The patterns are displaced for clarity. (b) Electron density profiles for DOPC bilayers containing EGCg at different *E/L*, all at 30°C and 98%RH.

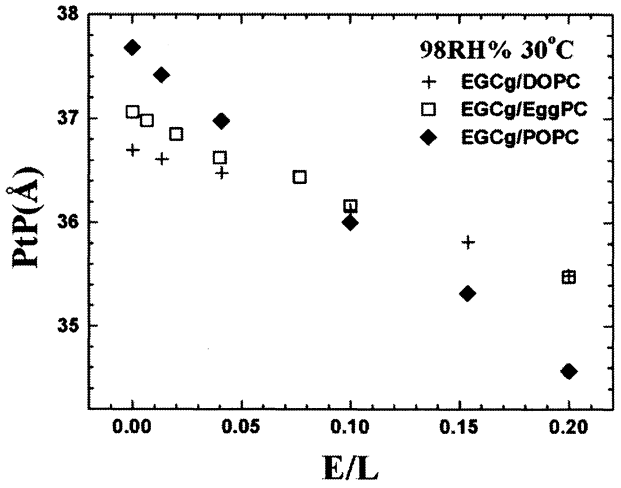

Figure 4-4 The peak-to-peak distance (*PtP*) of the electron density profiles plotted as a function of *E/L*. The profiles were obtained from X-ray diffraction of EGCg/DOPC (Figure 4.3), EGCg/POPC and EGCg/EggPC mixtures.

4.3.3. ITC

ITC measurement was performed by injecting lipid vesicles into a EGCg solution of concentration E_t. The measured cumulative reaction heat as a function of injected lipid concentration is shown in Figure 4.5 for four values of E_t. Eq. 4.5 was used to fit the data, from which K and $h^{(sat)}$ were obtained. The binding enthalpy per mole of EGCg, ΔH, was obtained from Eq. 6. The results were K=1.8 x 10^4 M^{-1}, ΔH= -4.3 kcal/mol for E_t=10μM; K=7.0 x 10^3 M^{-1}, ΔH= -3.3 kcal/mol for E_t=50μM; K=4.3 x 10^3 M^{-1}, ΔH = -5.1 kcal/mol for E_t=100μM; K=1.8 x 10^3 M^{-1}, ΔH= -3.7 kcal/mol for E_t= 300μM. It is clear that the measured apparent partition coefficients decrease with increasing EGCg concentration, whereas the measured binding enthalpy remains within a narrow range of value. We attribute this result to the effect of vesicle

aggregation caused by bound EGCg (see 4.4 DISCUSSION). Aggregation reduces the amount of vesicle's lipids available for EGCg binding. The effect of aggregation is greater at higher EGCg concentration, that makes the apparent partition coefficient decreases with EGCg concentration.

We have also performed ITC on several other lipids including POPC, DOPC/DOPG(9:1) and DOPC/DOPG(1:1). We obtained similar results, namely, the measured apparent binding coefficients decreased with increasing EGCg concentration whereas the binding enthalpy remained within a narrow range of value.

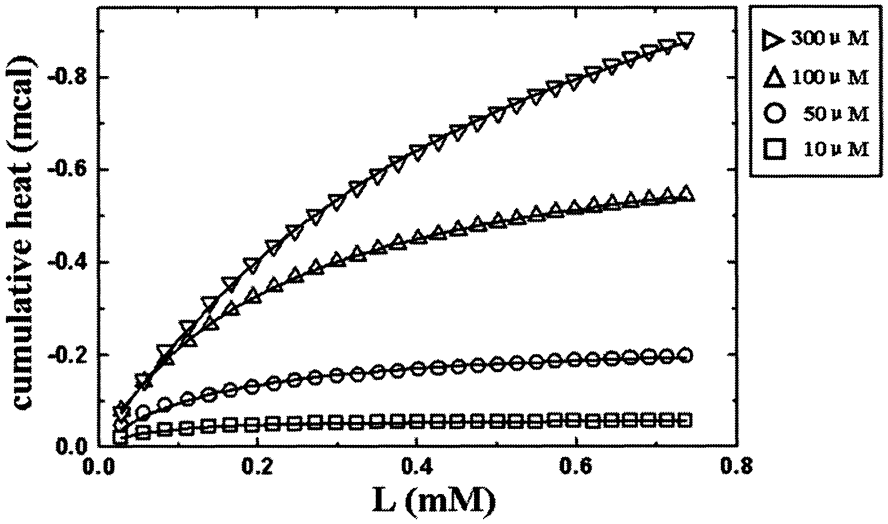

Figure 4-5 ITC measurement of EGCg solution titrated by DOPC vesicles, the cumulative heat $h^{(k)}$ vs. lipid concentration $L^{(k)}$. The series of data points represent different k. The symbols are square for the initial EGCg concentration E_t=10μM; circle for 50μM; triangle for 100μM; inverted triangle for 300μM. The solid curves are the fittings by Eq. 5, from which K and $h^{(sat)}$ were obtained.

4.3.4. Comparative experiments

To understand the effect of EGCg on membranes, we compared EGCg with other membrane-active molecules whose behaviors are to a large degree understood, including the turmeric (curry) extract curcumin, detergent Triton X100, and pore-forming peptide magainin.

(1) Comparison with curcumin

Experiment with curcumin was previously performed [32] exactly as for EGCg described above. In all concentrations of curcumin from 1.35 to 13.5 μM, the vesicle protrusion invariably lengthened to an equilibrium value (Figure 4.6). X-ray diffraction of curcumin-lipid mixtures showed a non-linear membrane thinning effect by curcumin. The data showed that the initial binding of curcumin had a large thinning effect, but above C/L~0.032 (C stands for curcumin) the thinning effect became considerably smaller. These results indicate that at low concentrations, curcumin mainly adsorbs to the water-lipid chain interface where the adsorption expands the interfacial area. But as C/L increases, the energy cost of the area expansion elevates the energy level of interfacial adsorption, so curcumin binding shifts to a second bound state inside the hydrocarbon region. This makes the membrane area expansion per curcurmin and the corresponding thinning effect much smaller at high C/Ls > 0.032 [32].

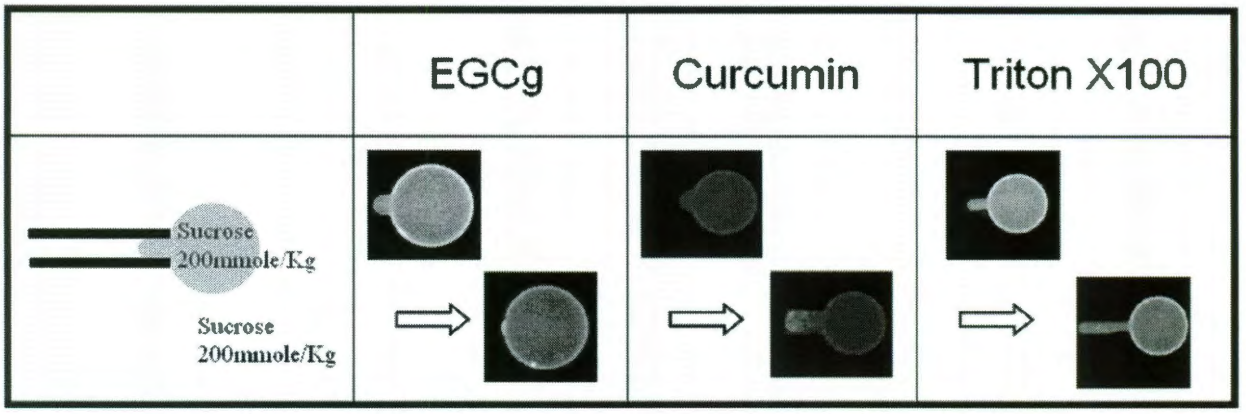

Figure 4-6 Comparative studies of EGCg with curcumin and Triton X100. The inside and outside solutions of GUVs were isotonic. In the presence of EGCg, the protrusion length initially increased and then decreased until diminished. In the presence of curcumin, the protrusion length steadily increased to an equilibrium length (data from). In the presence of Triton X100, the protrusion length steadily increased at a decelerating rate during the entire six minutes of observation time.

(2) Comparison with Triton X100

Experiment with Triton X100 was performed exactly as for EGCg described above at Triton concentration 10 μM. The GUV protrusion length continuously increased, with a decelerating growth rate, to a length corresponding to $\Delta A/A$~10% at the end of the observation period of six minutes (Figure 4.6). The effect of Triton X100 on lipid vesicles has been studied previously. Two independent studies [70, 71] found no bilayer solubilization at Triton concentrations below its critical micelle concentration (CMC) which was estimated to be 0.22-0.24 mM. Thus in the GUV experiment with 10 μM Triton, Triton molecules appeared to incorporate into the bilayer and expanded the GUV surface area.

(3) Comparison with magainin

Magainin is a well-understood pore-forming peptide [11, 69, 72]. Like many other well studied antimicrobial peptides [60, 73], magainin spontaneously binds to lipid bilayers; at low concentrations the binding expands the bilayer area without changing its permeability; but above a lipid-dependent critical concentration, magainin induces finite-sized stable pores in the membranes [6, 11] —the vesicles remain intact under this condition [31, 69]. This description of molecular action is in complete agreement with the extensive results obtained by Tamba et al. [69] who, among many experiments, observed the responses of individual GUVs to the introduction of magainin into the vicinity.

To find out if EGCg induces pores in membranes, we performed same experiments with EGCg and magainin. Systematic pore-forming experiments with an aspirated GUV have been performed with another pore-forming peptide melittin [31]. Therefore we could predict the response of a GUV if pores were formed in the bilayer. As a control, we repeated the melittin experiment with magainin. The observation chamber was filled with 200 mM glucose solution and 10 μM magainin. We observed the protrusion length initially increased and then decreased (due to the formation of pores when the $\Delta A/A$ exceeded a threshold), exactly the same reaction as in the melittin experiment [31, 55]. The decrease of the protrusion length was due to the finite-size of the peptide-induced pores that allowed the permeation of the smaller glucose more than the permeation of the larger sucrose;

and the resulted osmolality imbalance induced a net water influx [31, 55]. Thus the response of GUVs in this control experiment was similar to the EGCg experiments reported above. To test if EGCg formed pores in membranes, we designed experiments in which the protrusion length should grow if pores were formed.

In the first comparative experiment, we used a 206 mM sucrose solution in the observation chamber, slightly higher in osmolality than the 200 mM sucrose solution inside the GUV. If pores were formed in the membrane of the GUV, the osmolality imbalance would cause a rapid efflux of water from the GUV and reduce its volume. Under the circumstance the GUV surface area would not change, because area changing is a high energy process [15] and also it has been experimentally shown that membrane area is constant once the pores are formed [31, 65]. Then the relation between ΔL_p and ΔV is $\Delta V = -\pi R_p(R_v - R_p)\Delta L_p$, i.e., the GUV protrusion in the micropipette would grow. This was exactly what happened when the observation chamber included 3 μM magainin (Figure 4.7). On the contrary the response of a GUV to 10 μM EGCg was similar to the response when the observation chamber contained 200 mM sucrose solution, i.e., the protrusion length initially increased slightly and then decreased. However due to the osmolality imbalance, there was a slow water efflux from the GUV through the lipid bilayer; therefore there was a larger initial increase of L_p compared with the 200 mM sucrose solution experiment. To make a comparison between the experiments of 206 mM and 200 mM sucrose solutions, we used the formula $\Delta A = 2\pi R_p(1 - L_p/R_v)\Delta L_p$ to translate ΔL_p to ΔA in Figure 4.2b, even though part of ΔL_p in the case of 206 mM was due to

volume decrease. The point is that the effect of EGCg in reducing the GUV protrusion (negative ΔL_p) was stronger than the positive ΔL_p from the volume decrease due to the slow water efflux through the membrane.

In the second experiment, we produced GUVs in 200 mM glucose solution, and used an isotonic 200 mM sucrose solution in the observation chamber. This was the reversal of the control experiment for magainin described above. Therefore if magainin were in the observation chamber and formed pores in the GUV, the GUV protrusion would lengthen. This was exactly what we observed when we introduced 10 μM magainin in the observation chamber (Figure 4.7). On the contrary, in the presence of 10 μM EGCg, the protrusion length initially increased slightly and then decreased, exactly the same as when 200 mM sucrose solution was inside the GUV.

These comparisons clearly showed that EGCg did not induced pores or altered the permeability of the membranes. EGCg clearly reduced the GUV surface area, after a small initial expansion due to the EGCg binding.

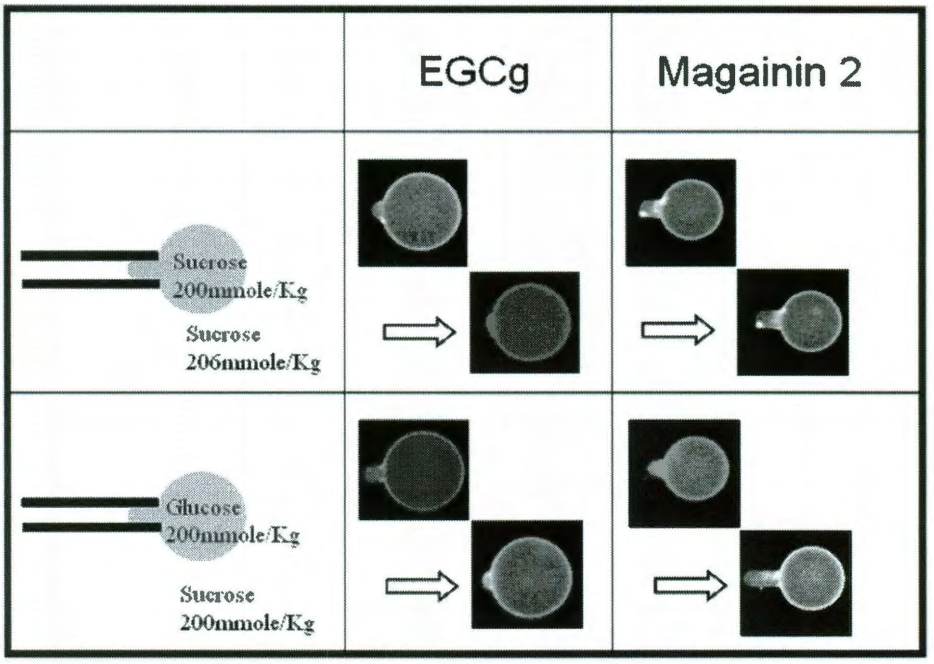

Figure 4-7 Comparative studies of EGCg with magainin to detect the formation of pores in GUVs. In case 1, the outside solution had a slightly higher osmolality. Magainin induced pores made the protrusion length increased before the GUV ruptured. On the contrary, the presence of EGCg made the protrusion length decrease after an initial increase, despite the water outflow by the osmolality imbalance that favored the protrusion length increase. In case 2, an isotonic glucose solution was inside the GUVs. Since the magainin-induced pores were of finite size, the permeation of the smaller glucose from inside was faster than the permeation of the larger sucrose from outside, there was a net outflow of water as in case 1 for magainin. On the other hand, the replacement of sucrose to glucose inside GUV did not affect the response of GUV to EGCg.

4.4. DISCUSSION

4.4.1. EGCg binds to the bilayer interface

All molecular binding to a membrane expands the membrane area, as we saw in the above examples. The membrane expansion can be correlated with the membrane thinning. If the molecules bind to the water-lipid chain interface, the interfacial area expansion will stretch the hydrocarbon region, making its thickness thinner. Due to the very small volume compressibility of the hydrocarbon chains [59], the fractional area increase is closely equal to the fractional thickness decrease of the hydrocarbon region: $\Delta A/A \approx -\Delta h/h$ where h is the thickness of the hydrocarbon region. This relation is valid only for interfacial binding; it does not hold for molecules binding in the hydrocarbon region [32]. Until now all water-soluble membrane-active molecules we have studied, including many antimicrobial peptides [74] and curcumin [32], exhibited a non-linear thinning effect as a function of the bound molecule-to-lipid ratio (M_B/L). At low M_B/L's, the initial thinning rate is large and linear, but at high M_B/L's the thinning rate diminishes. The energetic reason for this non-linear thinning effect has been explained [32, 65].

The effect of membrane thinning by EGCg is shown in Figure 4.4 in *PtP*. The thickness of the hydrocarbon region is $h \approx PtP - 10\,\text{Å}$, or *PtP* minus twice the length of the glycerol region (from the phosphate to the first methylene of the hydrocarbon chains). It is important to point out that this relation is valid not only for pure lipid bilayers [33, 75, 76] but also for bilayers with bound molecules [33]. Note that the

electron density profile of the glycerol region did not change with the EGCg concentration E/L in Figure 4.3-- the main changes occurred in the central chain region. Also in numerous measurements on lipid bilayers containing antimicrobial peptides [13, 65, 77], the *PtP* initially thinned by an amount ranging from 0.5 to 2 Å and then became almost constant with increasing concentrations of peptides, indicating no significant effect on the glycerol configuration by high concentrations of peptide binding. This means that the length of the glycerol region (~5 Å) is approximately a constant even when there are bound molecules in the bilayer. Thus the linear thinning in *PtP* (Figure 4.4) indicates a linear thinning in the hydrocarbon region h. This implies that, at least up to E/L=0.2, all EGCg molecules are bound to the interface.

From the slope of Δh vs. E/L, and the relation $\Delta A/A \approx -\Delta h/h$, one can calculate the area expansion by the binding of one EGCg molecule, A_S: $-\Delta h/h = A_S E/A_L L$ [33]. From Figure 4.4, we obtained h of pure lipid (26.7, 27.7. 27.1 Å for DOPC, POPC, EggPC), and from the volume of chains [66] divided by h we obtained the cross sectional area per lipid A_L (73.0, 67.7, 67.7 Å^2 for DOPC, POPC, EggPC). The results are: A_S = 16.2 Å^2, 37.4 Å^2, and 19.6 Å^2 for DOPC, POPC and EggPC, respectively. The larger A_S for POPC is reflected in the larger initial protrusion growth in the GUV experiment (Figure 4.2a). But compared with the similar size curcumin, which has $A_S \sim 240$Å^2 [32], the membrane expansion effect of EGCg is very small. Note that these values are not to be interpreted as the physical dimensions of the bound molecule. (The molecular weights of EGCg and curcumin

are, respectively, 458 and 368.) When a molecule binds to a lipid bilayer, the molecule might bring in additional water molecules or release some water molecules associated with the bilayer before binding. Such a redistribution of water molecules would affect the value of area expansion by molecular binding. In the study of curcumin interaction with membranes [32], we showed that the energy level of the interfacial binding state contained a term proportional to $A_S^2(M_B/L)$ due to the energy cost of membrane thinning (Eq. 2 of ref. 14). It was this term that made the transition of curcumin binding from the interfacial state to another bound state embedded in the hydrocarbon region at high M_B/L's. But for EGCg, the values of A_S is so small that energy level of the interfacial state remains sufficiently low (at least up to E/L~0.2) compared with the energy level of a potential binding state in the hydrocarbon region. That is why EGCg bound only to the interface and did not show any non-linear thinning effect.

However, there was no indication in our GUV experiments that EGCg bound exclusively to the outer leaflet of the GUV bilayer, as proposed by Tamba et al. [29]. For example, in the experiment with POPC (Figure 4.2a), the initial $\Delta A/A$ reached ~+2%. If there were a 2% area difference between the outer leaflet and inner leaflet, we would have seen an obvious shape change to the GUV [78, 79]. Yet all the GUVs subject to EGCg binding remained a sphere plus a protrusion during experiment. Many experiments [31, 55, 80] have demonstrated that molecules bound to the outer leaflet of a GUV [29] redistributed rapidly to the inner leaflet due to the high energy of asymmetric distribution. Tamba et al. proposed that the surface pressure

from the asymmetric binding caused the shape changes of the GUVs, for example, from sphere to prolate to dumbbell or pearls. But it is well known that such shape changes can also be explained by a change in the area to volume ratio due to the membrane area expansion by the EGCg binding, without invoking bilayer asymmetry [81, 82].

4.4.2. EGCg solubilizes lipid molecules from a bilayer but does not form pores

The binding of EGCg to a GUV caused an initial growth of the protrusion length due to the area increase of the vesicle. But within seconds, the protrusion length began to decrease, contrary to the curcumin binding to lipid bilayers. There are two possible reasons for the decrease of the protrusion length: either due to a decrease of the GUV surface area and/or due to an increase of the GUV volume. Because we kept the solutions inside and outside of the GUV isotonic, it could not be the volume change. Thus it was the GUV's surface area that had decreased. This implies that EGCg solubilized the lipid molecules from the lipid bilayer of GUVs. By the comparative studies with pore-forming peptide magainin, we also showed that the solubilization effect of EGCg did not create pores in the bilayer.

The solubilization effect apparently increased with EGCg concentration, as Figure 4.2a shows that the decrease of the protrusion length was faster with higher concentrations of EGCg. However the rupture of the GUV after the protrusion diminished appeared to be stochastic, not correlated with the concentration of EGCg.

It has been shown that the event of GUV rupture is initiated by nucleation of precursor defects in the lipid bilayer, therefore it is a stochastic happening [83, 84].

The solubilization effect of EGCg is compared with Triton X100 by their capacities of reducing the turbidity of a vesicle suspension. Figure 4.8 shows the attenuation of light passing through three samples, each containing 8 mM of DOPC: a lipid vesicle suspension, and the same suspension with 10mM of EGCg or Triton added. Triton almost completely diminished the attenuation, while EGCg reduced the attenuation by one order of magnitude.

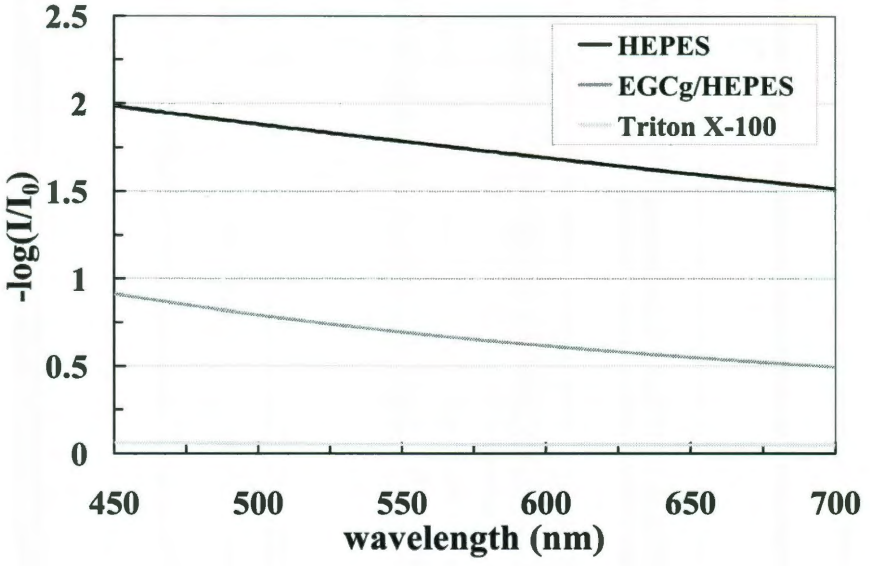

Figure 4-8 Attenuation of light passing three samples: A vesicle suspension of 8 mM DOPC, the same suspension with 10 mM EGCg added, and the same suspension with 10 mM Triton X100 added.

It is not clear what caused bursting of GUVs observed by Tamba et al. at EGCg concentrations above 30 μM. It could be due to the initial rapid GUV area expansion

at high EGCg concentrations or due to the solubilization effect or the combination of both. As observed by Tamba et al.[29], the bursting was a stochastic event—its time of occurrence was not predictable from the time EGCg was introduced.

Partition coefficient. Partition coefficient of EGCg to lipid bilayers has been reported in many prior publications [25, 26, 29] and were used to correlate with biological activities [27, 28]. Initially our intention was to quantitatively compare the membrane thinning effect measured by X-ray diffraction with the changes of membrane area measured by GUVs, as we did for curcumin binding [32]. For that purpose we would need to know the amount of EGCg bound to the GUV that would be calculated by the partition coefficient.

Although the ITC measurement of the partition coefficient looked normal for each EGCg concentration (Figure 4.5). The measured partition coefficients showed a strong dependence on the EGCg concentration. This makes the very concept of partition coefficient invalid. We believe that this was due to aggregation of vesicles in the presence of EGCg. The same conclusion was reached by Tamba et al. [29]. This calls into question all the previously reported partition coefficients [25, 26, 29].

Chapter 5

Kinetic Process of β-Amyloid Formation via Membrane Binding

5.1. Introduction

In their seminal paper that laid the fundamental concept for β-amyloid formation, Jarrett and Lansbury [34] pointed out that the state of proteins often reflects a kinetic effect rather than that of true thermodynamic equilibrium. In a previous study [4], we used penetratin as a model to study the membrane-mediated version of nucleation-dependent amyloid formation. Using peptide-lipid mixtures, we measured the peptide conformation as a function of the peptide-to-lipid ratio P/L and found a well-defined α to β conformation transition as P/L approaches a critical value P/L^*. The conformation transition correlated with peptide's effect on

membrane thinning. The peptide thinned the membrane in its α-helix conformation but reversed the thinning effect when it began to form β-aggregates. Will the kinetic process of membrane-mediated amyloid formation follow the same *P/L* dependence? Will the potential barriers of the kinetic process obscure the energy levels of peptide conformations seen in equilibrium? This question is relevant to the studies of membrane-active peptides in general, where disagreements between kinetic and equilibrium measurements are often the source of confusion. To answer these questions, we observed the kinetic transition of penetratin from its monomeric solution state to β-amyloid via its binding to a giant unilamellar vesicle (GUV). The results of kinetic experiments are usually complex, but with the reference to the equilibrium studies, the complex behavior can be made comprehensible. In particular the difference on the *P/L* dependence between the kinetic and the equilibrium results reveals an important potential barrier for peptide translocation across the lipid bilayer.

As far as we know, there have not been many direct comparisons between kinetic experiments and corresponding equilibrium experiments in peptide-membrane interactions. To do so, a common quantity must be measured in both. The fractional membrane thickness changes that can be measured in equilibrium by X-ray diffraction and the fractional membrane area changes that can be measured in kinetics by GUV experiment are directly related. It is by this relation we were able to make a direct comparison between the kinetic and equilibrium measurements.

The peptide penetratin [85] and β-amyloid protein 1-40 (Aβ 1-40), the major component of Alzheimer's disease amyloid plaque [34, 86] exhibited the same membrane mediated conformation changes. Both peptides are random coils in solution but change to α-helical or β-like conformations in the presence of negatively charged lipid membranes. Both peptides change from α to β conformations as the lipid charge increases or as the peptide concentration increases [86-91]. However kinetic experiments with Aβ 1-40 are difficult due to two intrinsic properties of Aβ 1-40. The first is its small effective net charge [86], that makes its apparent partition coefficient to anionic lipids three orders of magnitude smaller than that of penetratin [86, 92]. The second is its relatively low critical concentration in solution, about 25 μM [87]. As a result, the experimental concentration of Aβ 1-40 has to be kept below 25 μM. The combination of these two factors made the number of Aβ 1-40 bound to a GUV too small to have observable effect. In contrast, there is no apparent critical concentration for penetratin in solution, which makes the peptide convenient for performing GUV experiments. Because of their similar conformation changes induced by membrane binding, penetratin is a good representative for studying the membrane-mediated amyloid formation of Aβ 1-40.

Penetratin has long been studied as a cell-penetrating peptide [93-96]. We found interesting contrast between the kinetic behavior of this cell-penetrating peptide and that of antimicrobial peptide melittin [31].

5.2. Material and Methods

5.2.1. Materials

1,2-dioleoyl-*sn*-glycero-3-phosphocholine (DOPC), 1,2-dioleoyl-*sn*-glycero-3-phospho-(1'-*rac*-glycerol) (DOPG) and 1,2-dioleoyl-sn-glycero-3-phospho-ethanolamine-N-(Lissamine Rhodamine B Sulfonyl) (Rh-DOPE) were purchased from Avanti Polar Lipids (Alabaster, AL). Penetratin (acetyl-RQIKI WFQNR RMKWK K-amide) was synthesized by GenScript Corp (Piscataway, NJ) to >95% purity. All materials were used as delivered.

5.2.2. Sample preparation for X-ray diffraction and circular dichroism (CD)

We used the same protocol which was described in chapter 2.1.2 to make the x-ray diffraction and CD sample.

5.2.3. X-ray Lamellar Diffraction

We followed the same procedure described in chapter 2.1 to perform the x-ray diffraction data. One thing we should notice here is that unlike neutral lipids, charged lipids tend to absorb excessive water. Pure DOPC/DOPG 7:3 became fully hydrated at 96% relative humidity (RH). At higher RH, the diffraction pattern showed broaden peaks and diminished high Bragg orders, indicating undulation

fluctuations of bilayers as in excessive water [97]. For samples of *P/L* =1/50 and 1/30, the full hydration was reached at 96% RH; *P/L* =1/20 at 92% RH.

5.2.4. CD

Spectra were measured in a Jasco J-810 Spectropolarimeter (Tokyo, Japan). The substrates were oriented normal to the incident light as for the measurement of oriented circular dichroism [5]; however no change of peptide orientation was detected during the changes of temperature or humidity. The background spectrum for each sample was the spectrum for the same amount of lipid on the same substrate. After the background correction, the spectra of different *P/L* were normalized by the concentration of penetratin in each sample.

5.2.5. GUV experiment

The experiments were performed as described in chapter 1.5. Briefly GUVs of chosen lipid composition (7:3 DOPC/DOPG or pure DOPC) plus 0.5 mole % Rh-DOPE were produced in 210 mM sucrose solution by electroformation [32], and were transferred to a control chamber containing 200 mM glucose and 10 mM HEPES (pH 7.0). A GUV was aspirated by a micropipette with a small constant sucking pressure (~100 Pa producing a membrane tension ~0.4 mN/m) in the control chamber and then transferred, via a transfer pipette, to the observation chamber containing 200 mM glucose, 10 mM HEPES and penetratin at specified concentrations. The phase contrast between the sucrose solution inside the GUV and

the glucose solution outside was inspected during many randomly chosen runs to ensure that no change occurred.

Each GUV was observed for ~ 10 mins after the transfer to the observation chamber, unless it was ruptured. However the GUV response was analyzed only for the first 5 minutes, because the osmolality balance could not be guaranteed after ~5 minutes due to water evaporation.

5.3. RESULTS

5.3.1. Aggregations in multilayers

In previous experiments [4], the peptides aggregates in neutral lipid multilayers were not visible under microscope. The β-aggregates were inferred by the CD spectra [4]. In contrast, the aggregates in the multilayers of anionic lipid mixture DOPC/DOPG 7:3 were visible, at first under microscope (Fig. 5.1, top) and then, as their size grew bigger, by naked eyes. The aggregates appeared only in samples of P/L above the critical concentration $P/L^* \sim 1/20$. No aggregates were seen in the samples with $P/L \leq 1/20$. One sample of P/L=1/15 showed aggregations but another did not.

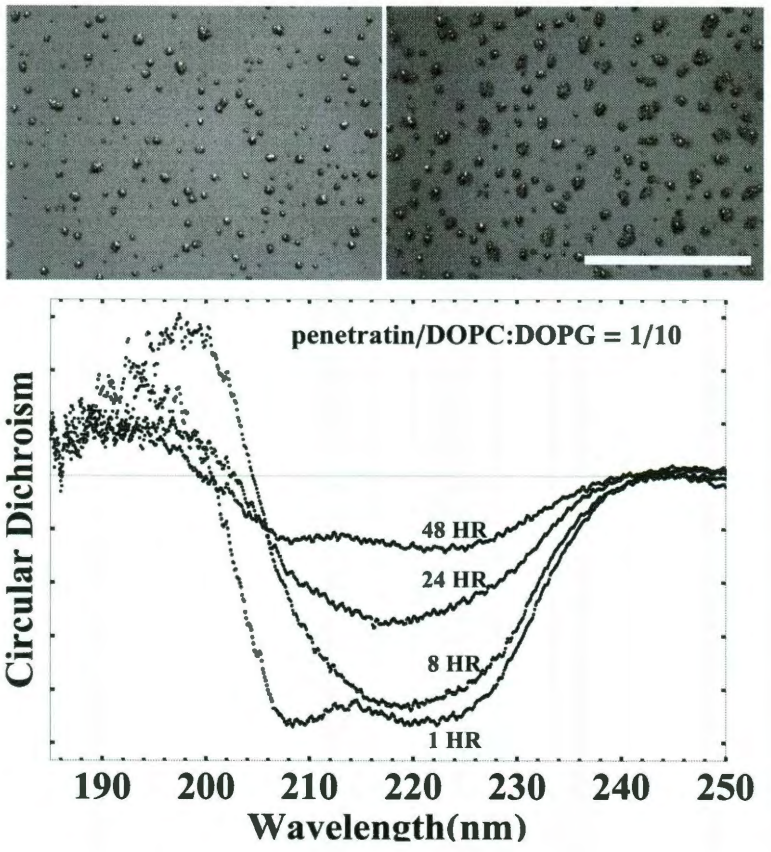

Figure 5-1 (Top) Microscopic (white light) images of DOPC/DOPG 7:3 multilayers containing penetratin at *P/L* = 1/12 (left) and at *P/L* = 1/10 (right). The images were taken two days after sample preparation. The scale bar = 1000 μm. (Bottom) The CD spectra of *P/L*=1/10 changed with time.

Interestingly the aggregations in anionic lipid multilayers progressed slowly. Small aggregates began to appear a few hours after the sample preparation, and grew larger with time. The CD spectrum of one sample was recorded continuously for two days (Fig. 5.1, bottom). At first the spectrum was α-helical and no aggregates were seen. After a few hours, the spectrum changed to β-like and aggregates were visible under microscope. Within the next day the β-like spectrum kept losing its

intensity and aggregates became bigger. Finally the CD reappeared as an α spectrum but its intensity was much smaller than the initial α-helical spectrum. Different samples changed at different time-rate and the aggregation size also varied, but the pattern of change remained the same as described. The samples seemed to stop changing after 2-3 days when the aggregates were spatially separated by an average distance larger than the size of the aggregates.

5.3.2. CD spectra

CD spectra for one series of DOPC/DOPG 7:3 with *P/L*= 1/50, 1/30, 1/20, 1/15, 1/12, 1/10 are shown in Fig. 5.2 (top). The spectra were measured 2 days after the sample preparation. The aggregation patterns of *P/L*=1/12 and 1/10 are shown in Fig. 5.1. This *P/L*=1/15 sample (whose CD is shown in Fig. 5.2) did not show visible aggregations; but another *P/L*=1/15 sample showed visible aggregations. All other samples did not show aggregations. The CD spectra were all α-helical like. In view of the evidence shown in Fig. 5.1, this indicated that β-aggregates did not contribute to the measured CD due to either light absorption or scattering by the aggregates [5]. The intensities of the CD shown in Fig. 5.2 were normalized by the peptide concentration in each sample.

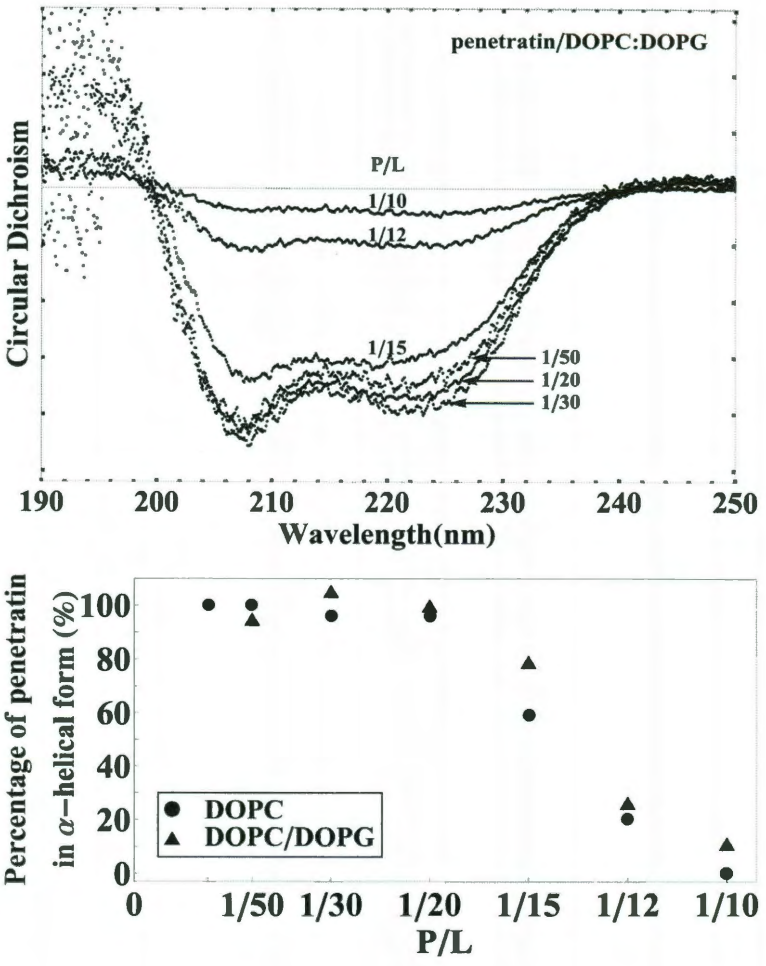

Figure 5-2 (Top) CD spectra for one series of DOPC/DOPG 7:3 with *P/L*= 1/50, 1/30, 1/20, 1/15, 1/12, 1/10, measured 2 days after the sample preparation. After the removal of lipid background, spectra were normalized according to the peptide density. (Bottom) The fraction of penetratin in the α-helical conformation as a function of *P/L*. The peptides in β-aggregates did not contribute to the CD spectra due to the uv absorption or scattering by the aggregates. The average spectrum of *P/L*= 1/50, 1/30, and 1/20 spectra was taken as the 100% spectrum. The percentage was defined by the ratio of the spectral intensity relative to this 100% spectrum. The data for DOPC were reproduced from Lee et al. [4] for comparison

Within the experimental error for CD intensity (~ 10%, mainly due to the sample thickness variations), the spectra of penetratin for *P/L*s below 1/20 are essentially the same, i.e., the peptides in these samples were all in the α-helical conformation. In *P/L*=1/12 and 1/10, only a small fraction of the peptides were in the α-helical conformation, as indicated by their diminished intensities; the rest of the peptides formed β-aggregates that did not contribute to the CD. *P/L*=1/15 might have small, invisible β-aggregates, hence somewhat smaller α-helical CD compared with $P/L \leq 1/20$. In Fig. 5.2 (bottom) the *P/L* dependence of the penetratin conformation in DOPC/DOPG 7:3 is compared to that in pure DOPC [4]. They are the same within measurement errors.

5.3.3. X-ray diffraction

The electron density profiles constructed from X-ray diffraction are shown in Fig. 5.3 (top). Each profile peaks at the position of the phosphate group on each side of the bilayer, even if peptides are embedded in the bilayer. This is because diffraction originates from electron density correlations. The interface-bound peptides are poorly correlated in position from layer to layer, therefore do not contribute to the measured electron density profile [4]. Thus the peak-to-peak distance (*PtP*) corresponds to the phosphate to phosphate distance across the bilayer, which is used as a measure of the bilayer thickness. Fig. 5.3 (bottom) shows the *PtP* for *P/L* from 0 to 1/20. We did not measure X-ray diffraction for $P/L \geq 1/15$, because once samples developed aggregates, they were no longer well defined for X-

ray analysis [98]. The error for *PtP* was estimated to be ~ ±0.1 Å from reproducibility using multiple samples.

The bilayer of DOPC/DOPG 7:3 (*PtP* =37.8 Å) is thicker than pure DOPC bilayer (*PtP* =37.0 Å). The degree of thinning per peptide in the former is somewhat smaller than that in the latter (Fig. 5.3). However the overall thinning pattern is similar in both cases.

The changes of bilayer thickness occur in the chain region (between the two interfaces of the bilayer). The thickness of the chain region h is obtained from *PtP* by $h \approx PtP - 10\text{Å}$ (see [99] for detailed discussions on this relation). Because the volumetric compressibility of lipids is exceedingly small ($\sim 5 \times 10^{-5}\ atm^{-1}$[59]), the fractional thickness decrease $\Delta h/h$ is effectively equal to the fractional membrane area expansion $\Delta A/A$. This relation will be used to relate the membrane thinning to the area expansion measured in the GUV experiment.

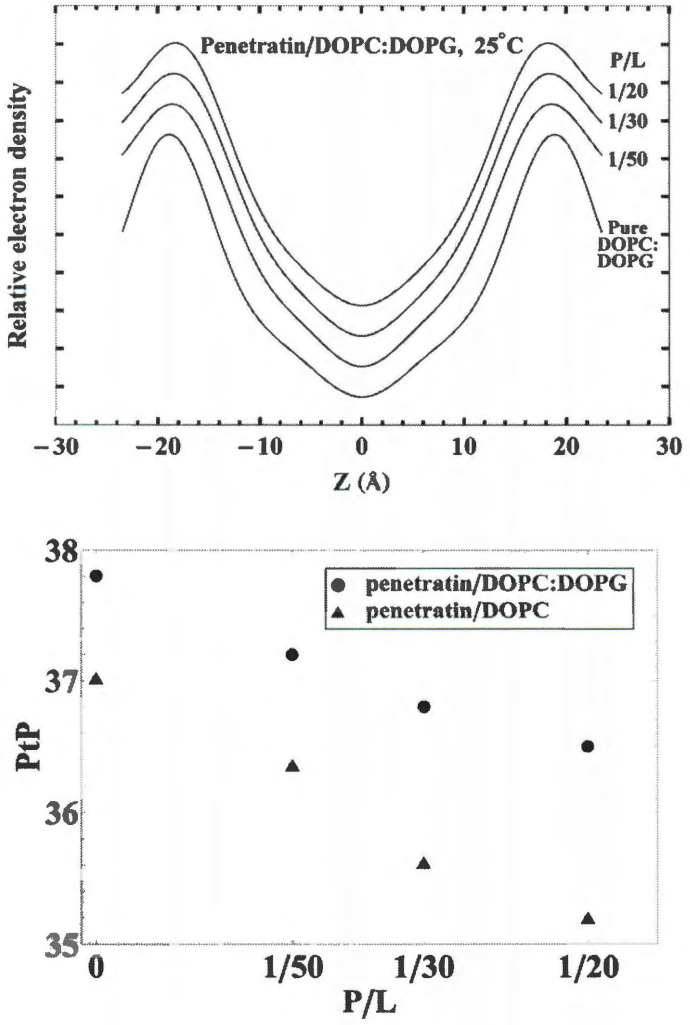

Figure 5-3 (Top) Electron density profiles across one unit cell obtained from X-ray diffraction for DOPC/DOPG 7:3 with *P/L*= 0, 1/50, 1/30, and 1/20. (Bottom) The peak-to-peak (*PtP*) distance of the electron density profile as a function of *P/L*. The data for DOPC were reproduced from for comparison.

5.3.4. GUV experiments

The aspiration experiment was designed so that a change of the area-to-volume ratio in the GUV could be measured by the change of the protrusion length

in the micropipette. A GUV was initially aspirated by a micropipette at a tension about 0.4 mN/m. It was then transferred to the observation chamber and exposed to the penetration solution when the transfer pipe was removed [32]. As penetratin diffused and bound to the GUV, we observed the response of the GUV as *P/L* increased in time. There were two definitive types of response for high and low penetratin concentrations, respectively.

For low penetration concentrations ≤ 0.08 μM, the protrusion length in the micropipette simply increased with time and reached a plateau ~200-300 s after the exposure to peptide solution (Fig. 5.4). The GUVs were observed for another 5 minutes. In all cases the protrusion length did not decrease and no aggregations occurred. For high penetration concentrations ≥ 0.6 μM, the protrusion length first increased but within ~40 s (for 0.6 μM) or ~5 s (for 6 μM) it began to decrease. Soon after the protrusion length began to decrease, aggregates appeared on the surface of the GUV (Fig. 5.5). After the protrusion length decreased to zero, the changes in the GUV surface area were no longer detectable (indicated by horizontal data points in ΔA/A vs. time (Fig. 5.4)).

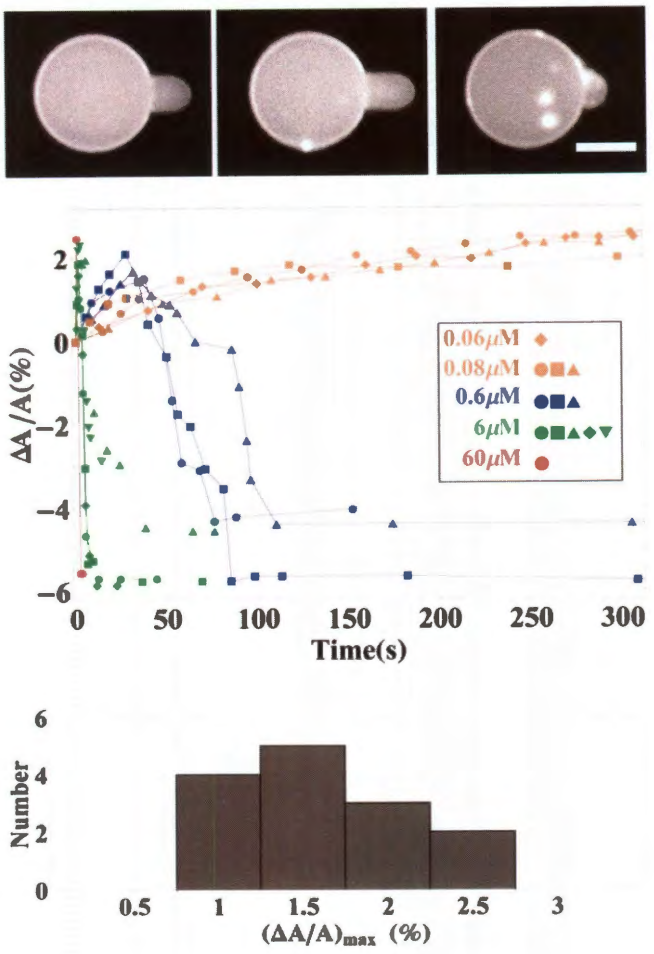

Figure 5-4 (Top) Fluorescence images of a GUV exposed to penetration concentration 0.6 μM in time sequence: Left t = 0, the protrusion length was caused by aspiration; thereafter the pressure inside the micropipette was held constant. Middle t = 68 s, the protrusion length reached the maximum. Right t = 112 s, the protrusion length decreased and aggregates appeared on the GUV surface. (Middle) The measured protrusion length was converted to the fractional area change $\Delta A/A$ plotted vs. time for representative runs at penetratin concentrations ≥ 0.6 μM or ≤ 0.08 μM. (Bottom) Histogram for the maximum values of $\Delta A/A$ among 14 high concentration runs (≥ 0.6 μM). Each column represents the number of runs with the maximum value of $\Delta A/A$ falling in the range indicated by the x axis. The scale bar = 20 μm.

For intermediate penetratin concentrations 0.1-0.3 μM, the GUV responses could be either of the low-concentration type or the high-concentration type, and sometimes a combination of the two, namely, the protrusion length increased, decreased and increased again (not shown). Whenever the protrusion length decreased, concurrently aggregations appeared.

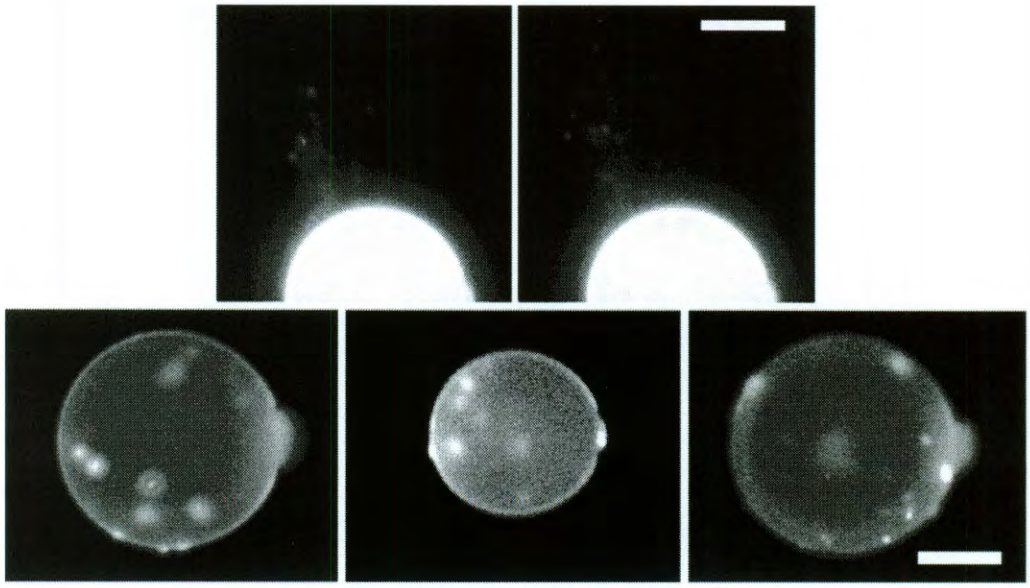

Figure 5-5 Images of aggregates. (Top) Two fluorescence images showing aggregates coming off the GUV. The right image was 5 s after the left image. (Bottom) Fluorescence images of aggregations appeared in three different GUVs. Since the aggregates move around, from the time sequences of the images, one could tell they were all on the GUV surfaces. On the equators (the focal plane), one could tell they were on the outside surface. The scale bar = 20 μm.

The aggregates moved around the surface of the GUV. Whenever the aggregates appeared on the equator of the GUV (where the microscopic focal plane was set), they could be seen clearly that they were on the outer surface, never on the

inner surface (Fig. 5.5 bottom). This was most clear if seen in time-sequence as the aggregates moved around. Occasionally the aggregates came off the GUV and they always came off outside the GUV, never into the interior of the GUV (Fig 5 top).

5.4. DISCUSSION

5.4.1. Neutral lipid vs. Anionic lipids

In our previous equilibrium experiment on penetratin-lipid interactions [4], we investigated four different neutral lipids, DOPC, OSPC, OMPC, and DMPC. It would be desirable to study the corresponding kinetics of penetratin against these neutral lipids. Unfortunately, the binding of penetratin to neutral lipids was simply too slow for kinetic observation. Fig. 5.6 compared the response of GUVs made of DOPC to the response of GUVs made of DOPC/DOPG 7:3. Even at a peptide concentration 10^3 times higher, the response of DOPC is still several times smaller than the response of the charged lipid within the experimental time of ~ 5mins.

Isothermal titration calorimetry measurement by Persson et al. [92] showed that anionic headgroups served the function of attracting the cationic peptides to the vicinity of the GUV. However, the subsequent binding to the bilayer interface was essentially independent of whether the lipid was charged or neutral [92, 100, 101]. We now compare the behavior of penetratin in DOPC and in DOPC/DOPG 7:3 after they bound to the bilayers. The CD and X-ray diffraction results show that the basic phenomenon was the same in both cases.

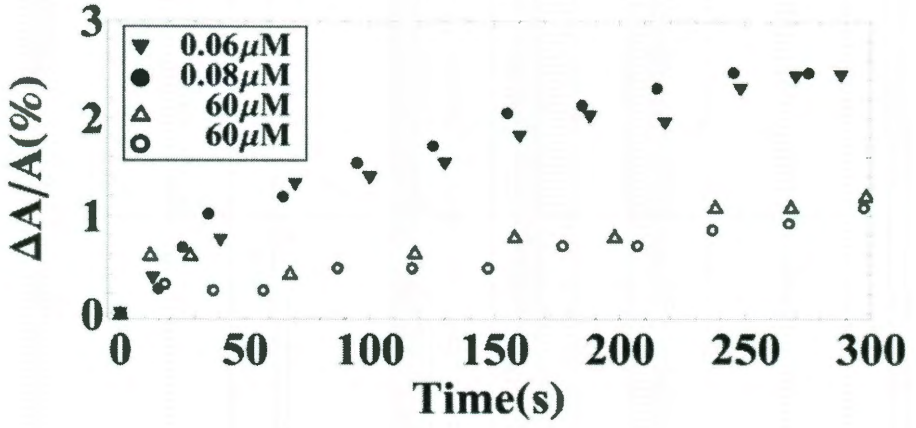

Figure 5-6 Comparison of the responses by neutral lipid (DOPC) GUVs (open symbols) and by charged lipid (DOPC/DOPG 7:3) GUVs (solid symbols) exposed to various penetratin concentrations. Note that the penetratin concentrations used for neutral lipid are 10^3 higher.

First, the initial binding thinned the membrane linearly with *P/L* and in this region the peptide was in the α-helical conformation (Figs. 2 and 3). There are small quantitative differences. The slope of *PtP* vs. *P/L* or the degree of thinning per peptide is slightly larger in neutral lipid than in the charged lipid (Fig. 5.3). For neutral lipids, we found that the maximum thinning coincidental with the critical *P/L** above which β-aggregates began to appear. This is also the case for charged lipids. The points of maximum thinning were not determined precisely because only finite numbers of *P/L* values were measured. However, it is clear that the *P/L** for both cases are above but close to 1/20. Above *P/L**, the fraction of peptide remained in the α-helical form as a function of *P/L* (Fig. 5.2) is also similar between the neutral and anionic lipids.

The most interesting difference between neutral and charged lipids is in the formation of β-aggregations. In neutral lipids, we could detect the change of peptide conformation from α to β, but aggregates were not visible. In contrast, anionic lipids apparently became part of the aggregate. They were attracted to the cationic peptide aggregates. In doing so, neutral lipids also become part of the aggregates, since lipid dye (0.5% in the lipid composition for GUV) was clearly accumulated in the aggregates (Figs. 4 and 5). As a result, the aggregates in anionic lipid bilayers grew to micron size.

From the similarity of CD and X-ray results between neutral and anionic lipids, we reach an important conclusion that after the initial binding, the peptide-lipid interaction is largely independent of the charge on the headgroup. In all the lipids we have studied, whether neutral or anionic, penetratin was bound to the bilayer interface and was in the α-helical form until *P/L* reached a lipid-dependent critical value *P/L**. This interfacial interaction facilitates the formation of β-amyloid [4].

5.4.2. Peptide aggregates in lipid multilayers

According to the concept of β-amyloid [34], once the peptides form a nucleus it is thermodynamically favorable for the peptide monomers to bind to the nucleus and subsequent aggregates. The larger the aggregates are, the lower the binding energy becomes, due to the larger numbers of binding contacts. Thus theoretically once *P/L* exceeds the critical *P/L**, we should expect all peptides turned into β-

aggregates (with the exception of a small number of monomers due to the entropic effect.) However, in lipid multilayers, the β-aggregation proceeded rather slowly due to the restricted mobility of the peptide molecules. The progress of aggregation in a *P/L*=1/10 sample (of DOPC/DOPG 7:3) was monitored by its CD spectra shown in Fig. 5.1. (We found that the rate of aggregation varied with samples; the times shown in Fig. 5.1 could vary by a factor as much as 2 in different samples.) Right after the sample preparation, the peptides were all still in the α-helical state. But within a few hours, the spectrum became β-like (or α–β mixture but strongly β-like; we do not believe that a standard CD spectral decomposition analysis is meaningful for short peptides [4]). At this point, no aggregates were visible under microscope. The intensity of this β-like spectrum decreased with time. This corresponded to the appearance of visible aggregates first in small size and grew larger with time. Apparently large aggregates absorbed or scattered UV light and therefore did not contribute to the CD spectrum. Finally after 2 days or so, the spectrum became α-helical with a much smaller intensity. Under microscope, the sample showed evenly spaced large aggregates (Fig. 5.1top). Thereafter, both the spectrum and the appearance of aggregates were stable.

This observation indicates that all penetratin molecules bound to lipid bilayers initially in the α-helical conformation, irrespectively of the concentration. But if *P/L* was greater than *P/L**, the peptides then aggregated into the β-form. The aggregates apparently incorporated the lipid mixtures as pointed out in the Result section. At first aggregates were small. But as they accumulated more monomers

and coalesced with each other, the aggregates finally separated by distances greater than their range of mobility. Therefore the final aggregation size is determined by the local peptide concentration or P/L as seen in the example of Fig. 5.1.

5.4.3. Kinetics of membrane-mediated β-aggregation

The GUV aspiration experiment was designed to measure the change of the area-to-volume ratio of the GUV [57]. It is important to know that one of the two variables, area or volume, is constant during the change so that the other variable can be measured. We used a sucrose solution inside the GUV and an isotonic glucose solution outside to provide a refractive index contrast, and monitored the phase contrast for a possible change of the GUV content. In all the cases we have examined we did not detect a change of phase contract during the experiment. We also performed the same experiment with isotonic sucrose solutions both inside and outside. If there were any leakage in the GUV, for instance by small pores, the effect of glucose-sucrose exchange must be stronger than the effect of sucrose-sucrose exchange due to the difference in the molecular weights of the two sugars [31]. We found no difference in the GUV responses between these two experiments. We therefore concluded that there was no volume change in the GUVs during our kinetic experiments. This is consistent with previous studies [92, 102, 103] finding that penetratin did not cause leakage or form pores in membranes.

From the image of GUV we measured the protrusion length L_p inside the micropipette, the GUV radius R_v, and the pipette radius R_p. From the geometry of the

GUV one finds the change of membrane area A by $\Delta A = 2\pi R_p \Delta L_p + 8\pi R_v \Delta R_v$, and the change of the GUV volume *V[57]* by

$$\Delta V = \pi R_p^2 \Delta L_p + 4\pi R_v^2 \Delta R_v .$$

Under the condition $\Delta V = 0$, ΔL_p is directly proportional to ΔA:

$$\Delta A = 2\pi R_p (1 - L_p/R_v)\Delta L_p.$$

When a GUV is exposed to a penetratin solution at t = 0, the bound peptide-to-lipid ratio P/L will increase with time from the initial condition of P/L = 0. We found the responses of GUVs fell into two different types in high and low penetratin concentrations, as described in the Result section. We first discuss the high concentration case ($\geq$ 0.6 μM) in which aggregations occurred. Generally speaking the kinetic behavior of GUVs was consistent with what we would expect from the equilibrium experiments. As P/L increased, L_p also increased that implied an area increase. Since

$$\Delta A/A \approx -\Delta h/h$$

as mentioned in the Result section, the area increase corresponded to the membrane thinning measured by X-ray in the low P/L region (Fig. 5.3). Then L_p increase reached the maximum, corresponding to the maximum thinning at P/L*. Further increase in P/L caused a decrease of L_p, corresponding to the decrease in membrane thinning, which was measured in neutral lipids [Fig. 5.6 of [4]] but could not be measured for charged lipids. Concurrently aggregates appeared on the GUV

surface, corresponding to β-aggregate formation as observed in multilayers when P/L exceeded P/L^* (Fig. 5.1). The aggregates appeared on the outer surface of the GUV (Fig. 5.5); most stayed on the outer surface, but some came off the GUV outer surface (Fig. 5.5 top). This explained why the L_p, decreased to a value shorter than its initial length at t = 0 (shown as $\Delta A/A$ in Fig. 5.4), because GUV lost some lipids to the aggregates.

On the other hand, when the penetratin concentrations were low (≤ 0.08 μM), L_p simply increased to a plateau value. Consistently, no subsequent L_p decrease was observed, nor did aggregation occur. Between the high and low concentration regions, the GUV response could be of either type, most likely due to the probabilistic nature of the actual P/L values on the GUV. Thus in all cases the kinetic behavior of the penetratin-GUV interaction was driven by the variable P/L, consistent with the changes of equilibrium state as a function of P/L.

Since the aggregates appeared on the outer surface or came off the outer surface of the GUVs, penetratin appeared not to have translocated across the bilayer. The maximum of the protrusion length increase corresponded to

$$\Delta A/A = 1.64\% \pm 0.49\%,$$

averaged over 14 runs with penetratin concentrations ≥ 0.6 μM (Fig. 5.4). This $\Delta A/A$ value is smaller than the corresponding value at the maximum membrane thinning,

$$\Delta A/A = -\Delta h/h = 4.68\% \pm 0.50\%,$$

measured at P/L^* in equilibrium (Fig. 5.3). This discrepancy is contrary to the experiments of melittin which formed pores at a lipid-dependent critical concentration P/L^* [31, 65]. In this case the values of $\Delta A/A$ when melittin formed pores in GUVs were consistent with the value of $\Delta h/h$ at P/L^* measured in equilibrium [31]. Also the behavior of GUVs with melittin was consistent with the assumption that melittin translocated across the bilayers and distributed symmetrically on both sides of the GUV bilayers [31]. Thus the asymmetric distribution of penetratin on the GUV might have caused an extra stress on the membrane that accelerated the β-formation at a value of $\Delta A/A$ smaller than the corresponding value $\Delta A/A$ for β-formation in equilibrium.

We now try to understand why the kinetic threshold of $\Delta A/A$ for α to β transition is smaller than its corresponding value in equilibrium. In our previous equilibrium studies [4], we analyzed the peptide transition from the α state to the β state by their respective chemical potentials:

$$\mu_\alpha = -\epsilon_\alpha^o + (K_a/2)A_S\Delta A/A + k_BTlnX_\alpha$$

and

$$\mu_{\beta n} = -n\epsilon_\beta^o + k_BTlnX_n,$$

where $-\epsilon_\alpha^o$ and $-n\epsilon_\beta^o$ are, respectively, the binding energy of the α state and the formation energy of the minimum β aggregate consisting of n monomers; the last term in each chemical potential is the entropic term with

$$X_\alpha = N_\alpha/L \text{ and } X_n = N_{\beta n}/L;$$

$N_{\beta n}$ is the number of n-meric β-states. What makes the membrane-mediated β nucleation different from the β nucleation in solution [34] is the additional second term in μ_α in the membrane-mediated process, i.e.,

$$(K_a/2)A_S\Delta A/A.$$

This is the elastic energy of expanding the monolayer area A_S per peptide when the monolayer area A has already been stretched by ΔA. $K_a/2$ is the monolayer stretch coefficient. (K_a is the bilayer stretch coefficient; its value is about 240 mN/m for most common phophatidylcholines [15]). The monolayer expansion per peptide, A_S = 68.3 Å^2 for DOPC/DOPG 7:3, can be measured from the slope of $\Delta h/h$ vs. P/L. ($A_S = dA/dP = A_L\ (dA/A))/d(P/L) = -A_L\ (dh/h))/d(P/L)$; A_L is the cross section area per lipid.)

In the equilibrium analysis, we found that the α to β transition occurred when this term $(K_a/2)A_S\Delta A/A$ reached a critical value at P/L^*. In the equilibrium measurements, the peptides were symmetrically bound to both sides of bilayers, so the peptide bindings were viewed as stretching the monolayer to which the peptides were bound. But in the kinetic experiment, the peptides were bound to the

outer monolayer only, yet both leaflets were stretched. Therefore for the GUV experiment, the stretch coefficient should be twice as large as the value used in equilibrium. That would imply that in the GUV experiment the α to β transition should occur at a $\Delta A/A$ value one-half of the critical value measured in equilibrium. This theoretical prediction is in marginal agreement with the experimental values given above.

On the other hand at low penetratin concentrations, the protrusion length L_p increased to plateau values corresponding to $\Delta A/A = 2.35 \pm 0.43\%$ (averaged over 6 runs), larger than the critical $\Delta A/A = 1.64\% \pm 0.49\%$ at high penetratin concentrations. Such GUV responses at low peptide concentrations were also found in melittin experiments [31]; the $\Delta A/A$ values of GUVs could grow slowly past the critical value without pore formation. In our case, the $\Delta A/A$ values of GUVs grew slowly past the critical value without β-aggregations. We suspect that there might be rate-dependent potential barriers in the kinetics of peptide-membrane interactions. We recall that the rupture tension of GUVs was also found to be rate-dependent by Evens et al. [84]. The origin of rate-dependent potential barriers is still poorly understood.

Chapter 6

Adhesion and Merging of Lipid Bilayers: method of measuring the free energy of adhesion and hemifusion

6.1. Introduction

Lipid bilayers can be induced to adhere to each other by molecular mediators and, depending on the lipid composition, the adhesion could lead to merging of the contacting monolayers, which is called hemifusion in the study of membrane fusion. Such bilayer-bilayer reactions have never been systematically studied. In the course of our studies of membrane-active molecules, we encountered such reactions. We believe that they need to be understood whenever bilayer-bilayer interactions take place, such as during membrane fusion. Our purpose here is to use three examples

to illustrate such mediator induced bilayer-bilayer interactions, and more importantly describe methods for characterizing such interactions. In particular we have devised a general method for measuring the free energy of adhesion or hemifusion. One possible application of the method is to analyze the multi-step lipid transformations during membrane fusion. Potentially the method can determine the energy of transition for each step.

In the first example, we discovered a phenomenon of spontaneous adhesion between phospholipid bilayers induced by low pH. Examples of viral fusion proteins activated by low pH are well known [104, 105]. Much less known are the pH dependence of bilayer properties [106]. In the second example, we injected a small amount of polyethylene glycol (PEG) solution between two bilayers that induced an attraction between them and developed a temporary contact zone. This osmotic depletion attraction between two surfaces is understood [17, 35]. What's interesting was that for some lipid compositions, the process led to hemifusion at low pH [38-43]. In the third example, the mediator of bilayer interaction is the multi-cationic peptide HIV-1 TAT48-60 (TAT). TAT is a prototype cell-penetrating peptide [107-109]. Recently it was suggested that TAT enters cells by causing leaky fusion of liposomes [110]. When we injected a small amount of TAT solution between two anionic lipid bilayers, it caused the bilayers to develop a cross-bridged contact zone. Like the case of PEG, for some lipid compositions the contact zone led to hemifusion. The implications of these findings will be explored further in future

experiments. This paper will concentrate on the methodology of characterizing these mediator-induced bilayer interactions.

We used two different methods to measure the adhesion energies depending on the strength of interaction. To measure weak adhesion energies, we used the experimental method invented by Evans and collaborators [14, 16-18, 111, 112] in which one flaccid GUV was released to adhere to one tensed GUV. For strong adhesion including hemifusion, we positioned two tensed GUVs next to each other. We then injected a small amount of mediators toward the GUVs. The induced interactions were sufficiently strong that a contact zone developed between two tensed GUVs. We introduced a general method of data analysis to obtain the free energy of adhesion. The method is based on the variation principle of equilibrium state. Therefore it is independent of how the adhesion or hemifusion state was reached. The same principle applies to both weak and strong interactions.

6.2. Material and Methods

6.2.1. Materials

1-stearoyl-2-oleoyl-*sn*-glycero-3-phosphocholine (SOPC), 1-stearoyl-2-oleoyl-*sn*-glycero-3-phosphoethanolamine (SOPE), 1,2-dioleoyl-*sn*-glycero-3-phosphocholine (DOPC), 1,2-dioleoyl-sn-glycero-3-phosphoethanolamine (DOPE), 1,2-di-(9Z-octadecenoyl)-*sn*-glycero-3-phospho-(1'-*rac*-glycerol) (DOPG), 1,2-dioleoyl-sn-glycero-3-phosphoethanolamine-N-(lissamine rhodamine B sulfonyl)

(abbreviated as Rh-DOPE), 1-oleoyl-2-[12-[(7-nitro-2-1,3-benzoxadiazol-4-yl)amino]lauroyl]-*sn*-glycero-3-phosphocholine (abbreviated as NBD-PC) and cholesterol were purchased from Avanti Polar Lipids (Alabaster, AL). HIV-1 TAT48-60 (acetyl-GRKKRRQRRRPPQ-amide) was custom synthesized and purified to >95% HPLC by GenScript (Piscataway, NJ). Calcein was purchased from Invitrogen (Carlsbad, CA). Polyethylene glycol of molecular weight 8000 Da (PEG8000) was purchased from Sigma-Aldrich (St. Louis, MO). All materials were used as delivered.

6.2.2. Giant unilamellar vesicles (GUVs) and micropipettes

The experiments were performed as described in chapter 1.5. For GUVs with dyes, lipids of a selected composition and 0.5% molar ratio of NBD-PC or Rh-DOPE were co-dissolved in1:1 (v/v) TFE and chloroform. For GUVs without dyes, the same lipid composition without the dye lipid was used.

For the second and third examples of mediator-induced lipid interactions a third pipette (diameter ~15 μm) was used to inject a PEG or TAT solution. The injection micropipette was connected to an electrical microinjector, Narishige IM-31 (East Meadow, NY), which was driven by a compressed gas. A small negative pressure was maintained before and after injection so as to ensure that no solution in the injection pipette was leaked. The injection was triggered by a foot switch connected electrical microinjector set at ~ 1 kPa. The injection rate was calculated to be 0.015μL per sec.

6.2.2.1. Weak Adhesion experiment

This experimental method was first developed by Evans and collaborators [14, 16-18, 111, 112], using a flaccid GUV against a tensed GUV, but we will use a slightly different data analysis. In order to clearly determine the contours of the lipid vesicles, we used GUVs containing a lipid dye. 10 μL of the SOPC GUV suspension (at 200 mM osmolality) from the production chamber was transferred to an observation chamber (500 μL) that contained 220 mM glucose at a pH controlled by a 10 mM buffer: pH 7 by HEPES; pH 6 by KH_2PO_4-NaOH; pH 5 by citrate. The GUVs rapidly deflated to new, smaller equilibrium volumes. One GUV was aspirated by a micropipette and held with sufficient suction to form a rigid spherical segment outside the pipette. During the adhesion experiment, this tensed GUV was held at the constant suction pressure. A second GUV was aspirated by another micropipette with an initial suction pressure equivalent to ~20 mm water. The GUV was then maneuvered into close proximity of the tensed GUV, and the adhesion process was allowed to proceed in discrete steps by lowering the suction pressure in the second pipette (Figure 6.1). In reversal, the adhered GUV was dissociated from the tensed GUV by stepwise increases in suction pressure, so the reversibility of the adhesion process could be evaluated. The entire process was recorded by fluorescence image using a Nikon coolSNAP HQ2 camera.

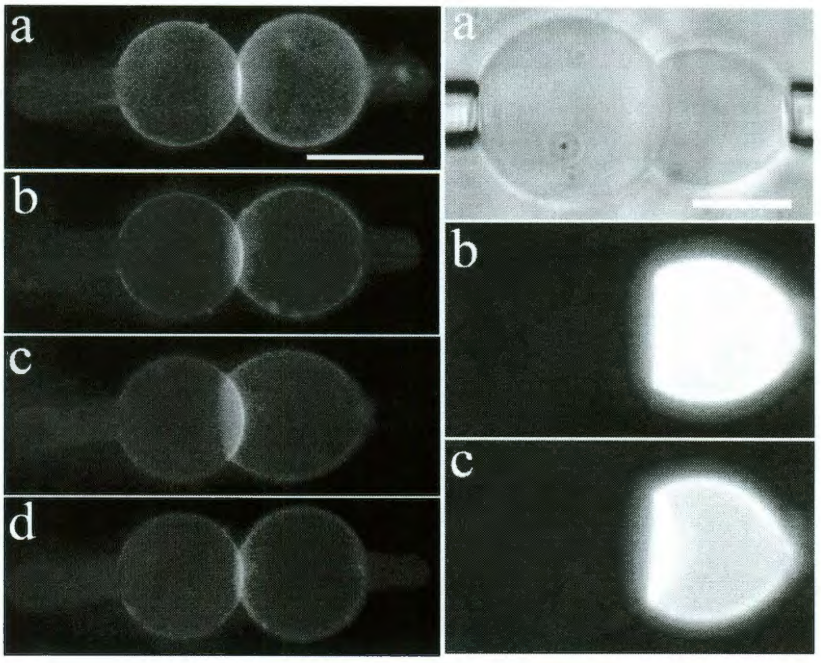

Figure 6-1 (Left column) Fluorescence images of an adhesion process, SOPC GUVs at pH 5. The right-hand GUV was initially held at a suction pressure ~20 mm water and positioned to contact the tensed GUV on the left-hand side. (a) The suction pressure for the right GUV was lowered to ~3.2 mm to allow adhesion. (b and c) The suction was lowered further to allow more adhesion. (d) The suction pressure was increased to the pressure of (a). Scale bar = 50 μm. (Right column) Lipid dye transfer. (a) White light image of adhered GUVs. (b and c) Lipid dye transfer images at time 66 s and 476 s. Scale bar = 25 μm.

6.2.2.2. Adhesion induced by a transient presence of mediators

We studied induced adhesion by injecting, within a short time interval, a small amount of mediators between two tensed GUVs. After the injection, those mediator molecules which were not bound to the GUVs would disperse in the observation chamber to such a low concentration that no further interaction with the GUVs was detectable.

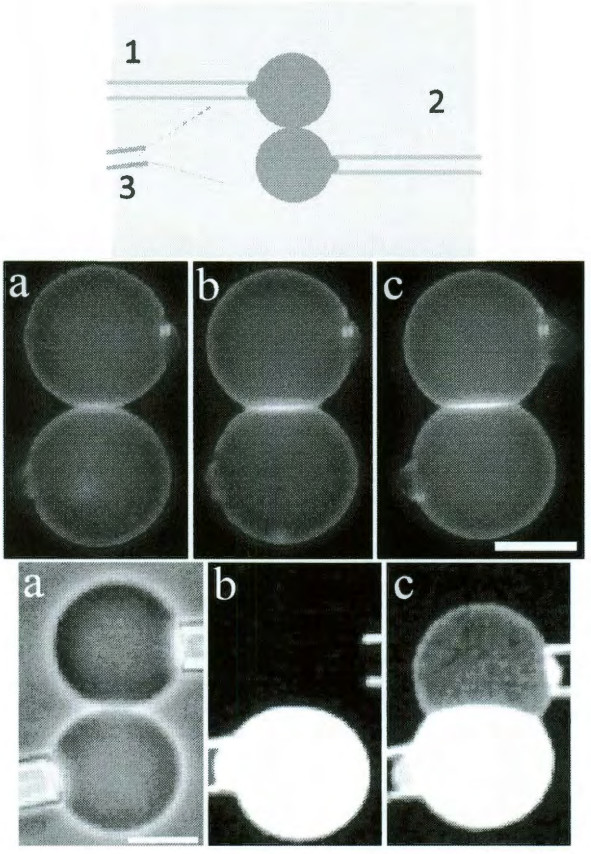

Figure 6-2 (Top) Schematic of GUV adhesion induced by a transient injection of mediators. Two GUVs were aspirated by micropipette 1 and 2. The mediators were injected from the pipette 3, about 200 μm away. (Middle) Fluorescence images of GUVs of DOPC/DOPE/cholesterol (2:2:1) induced to hemifusion by PEG at pH 4. (a) Before injection; (b) a contact zone was developed upon the injection; (c) another equilibrium adhesion state at a higher suction pressure. (Bottom) Lipid dye transfer. (a) White light image before injection; (b and c) lipid dye transfer images at time 0 s and 237 s). Both scale bars = 25 μm.

For this experiment the osmolality of the glucose solution in the observation chamber was kept the same as the sucrose solution in the production chamber. Two GUVs were aspirated by two separate micropipettes, each to a membrane tension

about 0.7 dyn/cm, and were then positioned to slightly in contact with each other. From a distance ~200 μm, a small amount of mediator in isotonic solution was injected toward the vicinity of the two contacting GUVs (Figure 6.2).

(2.1) PEG as the mediator

PEG of high molecular weight (e.g., PEG8000) in solution has been shown to induce osmotic depletion attraction between two surfaces in close distance [17, 35]. A small amount of 5 wt % PEG8000 solution at pH 7, 6, 5, or 4 (by citrate), adjusted to 200 mM osmolality by glucose and buffer, was injected toward the vicinity of the two contacting GUVs. The injection apparently produced an attractive force between the two GUVs, as a flat contact zone developed between them (Figure 6.2). In most cases, once the injection stopped, the GUVs bounced back from the contact and separated. However, for certain lipid compositions, for example DOPC/DOPE/cholesterol (2:2:1), if the injected PEG solution was at pH ~ 4, the two GUVs remained adhered to each other, and would not separate by increasing the suction pressure or by manipulating the micropipettes. Subsequent dye transfer tests showed that the contact zone developed to hemifusion. Hemifusion would not occur if the injected PEG solution was at pH higher than 4 or if the injected solution contained no PEG. For lipid composition like pure DOPC, no hemifusion occurred in any case. Note that for the pH effect to work, the observation chamber did not contain buffers, so that during the injection the two GUVs were temporarily surrounded by low pH. If the observation chamber solution was buffered at pH 4,

GUVs were too fragile (had a tendency to rupture upon small disturbance) to perform this experiment.

It is important to make clear that the effect of PEG occurred only during the injection. Once the injection stopped, the PEG molecules were dispersed and the bulk effect was negligible. The same experiment was repeated many times. The maximum amount of PEG injected into the observation chamber was equivalent to a concentration of 0.038 wt % PEG. The PEG induced osmotic depletion attraction between lipid bilayers has been measured by Kuhl et al. [35]. Below 1 wt % PEG concentration, there was no detectable effect of osmotic depletion attraction. Indeed we found that there was no attraction between two GUVs after the injection stopped. Therefore in our experiment the attractive force between the two GUVs was a transient effect during the injection.

(2.2) TAT as mediators

The experimental setup was the same as the PEG experiment, except that the injected solution was 20 μM TAT in 10mM HEPES (pH 7) and 190 mM glucose (total osmolality 200mM). The maximum amount of TAT injected was equivalent to 6 nM when dispersed to the entire observation chamber. At such TAT concentration, no effect on GUVs was detected.

As long as the GUV composition included anionic lipids, for example DOPC/DOPG (7:3) or DOPC/DOPE/DOPG/cholesterol (2:2:1:1), an injection of TAT solution produced a stable contact zone between two GUVs (Figure 6.3). The contact

zone developed into hemifusion in the case of DOPC/DOPE/DOPG/cholesterol (2:2:1:1), but not in the case of DOPC/DOPG (7:3).

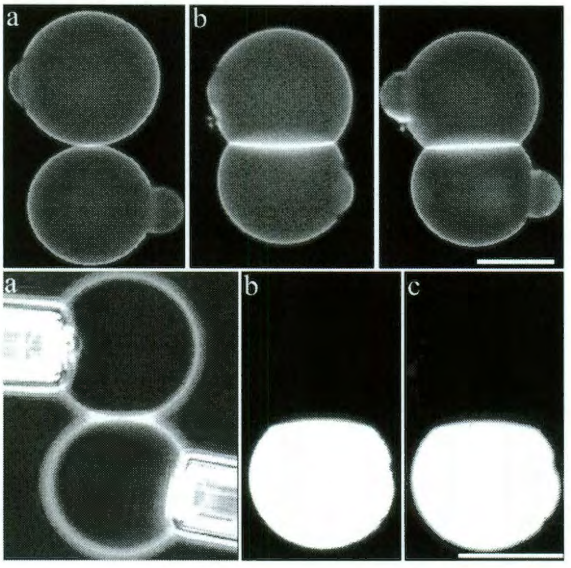

Figure 6-3 GUVs of DOPC/DOPG (7:3) induced to adhere by TAT. (Top) Fluorescence images. (a) Before injection; (b) after injection; (c) another equilibrium adhesion state at a higher suction pressure. (Bottom) Lipid dye transfer. (a) White light image before injection; (b and c) lipid dye transfer images at time 51 s and 552 s). Both scale bars = 25 μm.

(2.3) lipid dye transfer and content mixing experiments

The occurrence of hemifusion was established by a test that showed transfer of lipid dye from one GUV to another and a second test that showed no transfer of aqueous contents between the two GUVs [113]. The dye transfer was monitored by the fluorescence images recorded throughout the experiment (Figure 6.1, 6.2, 6.3).

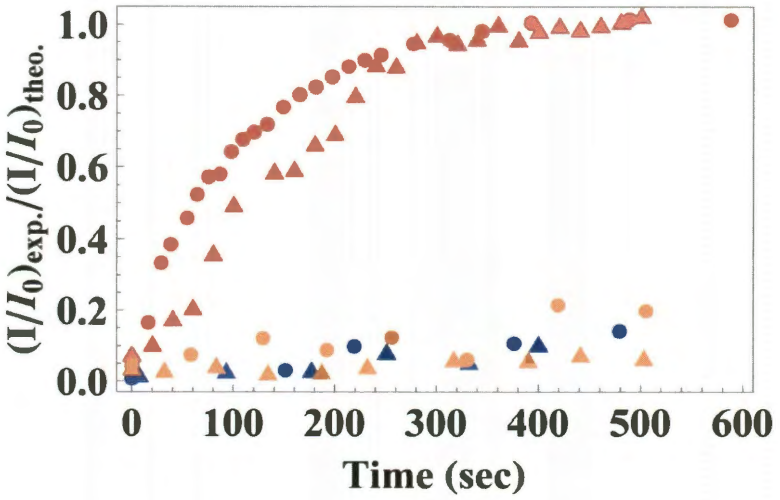

Figure 6-4 Lipid dye transfer between two adhered GUVs: the transferred fluorescence intensity I divided by the remaining fluorescence intensity I_o as a function of time. The ordinate is the ratio of the experimental value $(I/I_o)_{expt}$ over the theoretical value $(I/I_o)_{theo} = 1/[2+(A_2/A_1)]$. For clarity, only two examples are shown for each of three cases. Red symbols: GUVs of DOPC/DOPE/cholesterol (2:2:1) induced to hemifuse by PEG at pH 4. Blue symbols: SOPC GUVs adhered at pH 5. Brown symbols: GUVs of DOPC/DOPG (7:3) induced to adhere by TAT.

One GUV contained lipid dye and one without dye were used as a pair. Let I_o and I be the fluorescence intensity per unit area through the originally dyed GUV and the originally undyed GUV, respectively. Assuming that the dye transfer occurred between the outer leaflets of the two hemifused bilayers, one could predict the saturation value of I/I_o to be $1/[2+(A_2/A_1)]$, where A_1 and A_2 are, respectively, the membrane areas of the originally dyed GUV and undyed GUV [80, 114]. The dye transfer curves were plotted as the ratio of the experimental $(I/I_o)_{expt}$ over the theoretical value $(I/I_o)_{theo} = 1/[2+(A_2/A_1)]$, as shown in Figure 6.4. For example, when GUVs of composition DOPC/DOPE/cholesterol (2:2:1) were induced to adhere

by PEG at pH 4, the experimental value of $(I/I_o)_{expt}$ reached the theoretical value (Figure 6.4) indicating a dye transfer between the outer leaflets only. In contrast, there were only very small amounts of dye transfer if two GUVs adhered but not hemifused (Figure 6.4).

To test if there was content mixing between the aqueous compartments of the two contacting GUVs, we included 8 μM calcein (which is below the quenching concentration) in the content of one GUV (with lipid dye). In all cases, we detected no transfer of dye between the vesicle contents (not shown). Both the content dye leakage experiment and the GUV phase contrast (sucrose inside vs. glucose outside) inspection showed that none of the GUVs was permeabilized during the experiments. Two lipid vesicles are in a hemifusion state when the outer leaflets of the two bilayers merge but the inner leaflets and aqueous compartments remain separated [113].

6.3. Data analysis

Measurement of the free energy of adhesion

For the free energy measurement, we let both GUVs contain a lipid dye. As will be seen in the following, the contours of the GUVs need to be clearly imaged for the purpose of analysis. After a stable contact zone was established, the suction pressure was increased stepwise to reach a series of new stable or metastable states

of adhesion, so that each adhesion state was measured multiple times at different suction pressures.

6.3.1. Data Analysis for weak adhesion

We use the thermodynamic principle that when a system is in equilibrium, its free energy is minimum with respect to perturbations. This method is applicable to any equilibrium state, independent of how the state is reached. Although our method and the method used previously by Evans and Metcalfe [16] are both based on the principle of work and energy, we believe that our method has the advantage of conceptual simplicity. For example, it is straightforward to apply our method to two different adhesion experiments, as we will demonstrate below.

The system under consideration is the flaccid GUV which spontaneously adhered to a stationary tensed GUV (Figure 6.1). Note that the free energy associated with the membrane tension τ is $\int \tau dA$, where A represents the area of the membrane and $\tau = K_a \Delta A/A_o$; K_a is the membrane stretch constant [15], A_o is the area of unstretched membrane, and $\Delta A + A_o$ is the area of the stretched membrane. The energy change due to a small increase of area δA is $\frac{1}{2}K_a(\Delta A + \delta A)^2/A_o - \frac{1}{2}K_a(\Delta A)^2/A_o = \tau \delta A$.

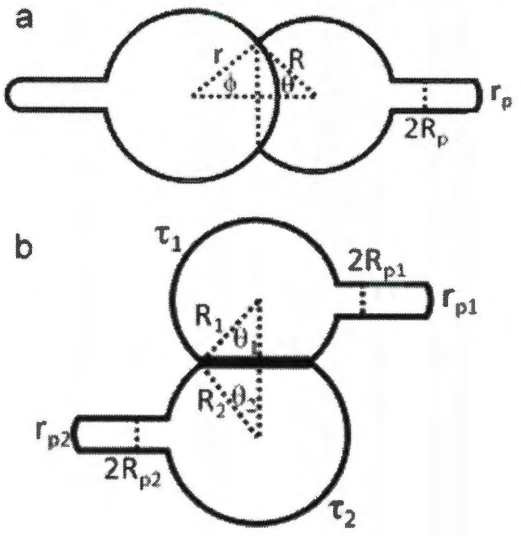

Figure 6-5 Geometry of two adhered GUVs. (a) Weak adhesion between a flaccid GUV (right) and a tensed GUV (left). (b) Strong adhesion between two tensed GUVs.

We assume that the adhered GUV consists of (1) the adhered area on the surface of the stationary tensed GUV of radius *r*; (2) a cylindrical part inside the micropipette of radius R_p; and (3) the unadhered part, or the area between the parts (1) and (2), which is spherical with a radius *R* (Figure 6.5a). Note that the sphericalness of the unadhered part is not a condition of equilibrium. Rather, we simply selected those equilibrium states in which the unadhered area appeared to be spherical. This is for the purpose of data analysis, for which the area of the GUV needs to be measured. We realized that this was not exact. The uncertainty of this area estimate is the main source of error for this method.

The energy variation δF due to a perturbation consists of three terms and the total is zero at equilibrium:

$$\delta F = \tau \delta A + \gamma 2\pi r^2 sin\phi \delta\phi - (\Delta P)\pi R_p^2 \delta L = 0 \quad (6.1)$$

The first term is the tension term due the area change δA by perturbation. The second term is due to the change of the adhesion area by perturbation, with γ defined as the adhesion energy per unit area. The third term is the work done by the suction pressure ΔP defined as the atmospheric pressure minus the pressure inside the micropipette, with δL defined as the increase of the protrusion length inside the micropipette due to the perturbation. We did not include the bending energy because it is orders of magnitude smaller than the tension energy [15, 17]. τ is obtained from the Laplace equations [57]: $2\tau\left(\frac{1}{r_p} - \frac{1}{R}\right) = \Delta P$, where r_p is the radius of the curvature of the protrusion cap inside the micropipette. The value of r_p was measured, which was not necessarily equal to R_p.

A perturbation causes variations in six variables, i.e., δR, δθ, δφ, δL, δA and δτ, (where the angles θ and φ are defined in Figure 6.5a) subject to the following five constraints. (We have not included the variable r_p which has small contributions to the volume and area variations. We found that the inclusion of the variable r_p changed the free energy γ by <3% which is insignificant in view of the larger errors in measurements.)

(i) The volume within the GUV remains constant, or there is no influx or outflux of water. This is a condition well established in the GUV aspiration experiment [15, 32, 57, 115, 116]:

$$\pi R^3\left[\frac{2}{3}+cos\theta-\frac{1}{3}cos^3\theta\right]-\pi r^3\left[\frac{2}{3}-cos\phi+\frac{1}{3}cos^3\phi\right]+\pi R_p^2 L=const \quad (6.2)$$

(ii) The total area of the GUV consists of three parts as stated above:

$$\delta A=\delta\left[2\pi R^2(1+cos\theta)+2\pi r^2(1-cos\phi)+2\pi R_p L\right] \quad (6.3)$$

(iii) The contact areas of the two GUVs are the same:

$$Rsin\theta=rsin\phi$$

(iv) The tension-area relation:

$$\delta\tau=K_a\frac{\delta A}{A} \quad (6.5)$$

(v) The Laplace equation $P_{GUV}-P_{atm}=2\tau/R=const.$ Because there is no change in the pressure, we have $\frac{\delta\tau}{\tau}=\frac{\delta R}{R}$ (6.6)

We used conditions Eqs. 6.2-6.6 to reduce the number independent variation variables from 6 to 1. Thus Eq. (6.1) is soluble for the unknown quantity γ, the adhesion free energy per unit area.

Our method allows variations of all the variables of the system under consideration, except for the constant volume in each GUV. The constant volume of a GUV is a well established condition during the aspiration process. It has been demonstrated by the inventors of the aspiration method [14] and also by our own experiments [32, 115, 116] that as long as the osmotic balance is maintained between the inside and outside of a GUV, the volume of the GUV remains constant.

For comparison, the previous method of Evans and Metcalfe [112] presumed that the area, the tension, as well as the volume do not change during perturbation. In addition, we chose only those equilibrium states in which the unattached part of the GUV was spherical so as to simplify the calculation for the geometric factor. The main source of errors for using a GUV to calculate the energy is always the geometric factor [112].

6.3.2. Data analysis for strong adhesion

The equilibrium states of a strong adhesion are shown in Figures 2 and 3, i.e., two spherical GUVs, labeled 1 and 2, with a flat contact zone in between (Figure 6.5b). The sphericalness of the unattached parts of the GUVs and the flatness of the contact zone are not the condition of equilibrium. We selected pairs of GUVs of approximately the same size, aspirated each pair by the same suction pressure, and selected the cases that had flat contact zones. We adjusted the positions of the micropipettes until the unattached parts of both GUVs appeared to be spherical. This is strictly for the purpose of measuring the membrane area. Upon perturbation, the free energy variation δF consists of the tension terms, the adhesion terms and the work terms by suction for both GUVs:

$$\delta F = \tau_1 \delta A_1 + \tau_2 \delta A_2 + \gamma \cdot \delta(\pi R_1^2 sin^2\theta_1) - (\Delta P_1)\pi R_{p1}^2 \delta L_1 - (\Delta P_2)\pi R_{p2}^2 \delta L_2 = 0 \quad (6.7)$$

with $2\tau_1\left(\frac{1}{r_{p1}} - \frac{1}{R_1}\right) = \Delta P_1$, and $2\tau_2\left(\frac{1}{r_{p2}} - \frac{1}{R_2}\right) = \Delta P_2$.

A perturbation causes variations in 10 variables δR_1, δR_2, $\delta\theta_1$, $\delta\theta_2$, δL_1, δL_2, δA_1, δA_2, $\delta\tau_1$, and $\delta\tau_2$, (Figure 6.5b), subject to 9 constraints. (Again, we did not include δr_{p1} and δr_{p2} for the reasons noted above.)

(i) The volume of each GUV remains constant:

$$\pi R_1^3\left[\frac{2}{3}+cos\theta_1-\frac{1}{3}cos^3\theta_1\right]+\pi R_{p1}^2 L_1 = const \tag{6.8}$$

$$\pi R_2^3\left[\frac{2}{3}+cos\theta_2-\frac{1}{3}cos^3\theta_2\right]+\pi R_{p2}^2 L_2 = const \tag{6.9}$$

(ii) The total area of each GUV consists of the spherical part, the contact zone and the protrusion inside the micropipette:

$$\delta A_1 = \delta\left[2\pi R_1^2(1+cos\theta_1)+\pi R_1^2 sin^2\theta_1+2\pi R_{p1}L_1\right] \tag{6.10}$$

$$\delta A_2 = \delta\left[2\pi R_2^2(1+cos\theta_2)+\pi R_2^2 sin^2\theta_2+2\pi R_{p2}L_2\right] \tag{6.11}$$

(iii) The contact areas of the two GUVs are the same:

$$R_1 sin\theta_1 = R_2 sin\theta_2 \tag{6.12}$$

(iv) The tension-area relations:

$$\delta\tau_1 = K_a\frac{\delta A_1}{A_1} \tag{6.13}$$

$$\delta\tau_2 = K_a\frac{\delta A_2}{A_2} \tag{6.14}$$

(v) The Laplace equation $P_{GUV}-P_{atm}=2\tau/R=const$. Because there is no change in the pressures, we have

$$\frac{\delta\tau_1}{\tau_1} = \frac{\delta R_1}{R_1} \qquad (6.15)$$

$$\frac{\delta\tau_2}{\tau_2} = \frac{\delta R_2}{R_2}.$$

6.4. Results

6.4.1. Weak Adhesion experiment

For lipid vesicle experiments, it is a standard practice to coat the glass surface with bovine serum albumin (BSA) to neutralize the surface charge [117]. Since BSA in solution could induce osmotic depletion attraction between lipid bilayers [18], we were concerned about the possibility that the coated BSA might, perhaps in a pH-dependent manner, re-dissolve into the solution. Thus we measured the BSA spectrum [118] of the solution taken from the observation chamber at different pH. In all cases, we did not find the glass coated BSA re-dissolved into the solution.

Spontaneous adhesion between lipid vesicles can be seen in the vesicle suspension. For SOPC vesicles, we did not detect spontaneous adhesion at pH values 6 and 7 (Figure 6.6). But at pH 5 or lower, vesicles spontaneously adhere to each other in pairs or in multiples (Figure 6.6). The same adhesion phenomena were seen by adding acid to achieve pH 5 without buffers. Very importantly, the adhesion was reversible. As shown in Figure 6.1, the adhesion of the flaccid GUV took place as the suction pressure was decreased. At any step, if the suction pressure was increased, the GUV reversibly detached and recovered the previous states. Since the system

was in equilibrium at each suction pressure, the energies measured at different suction pressures were very close (Figure 6.7).

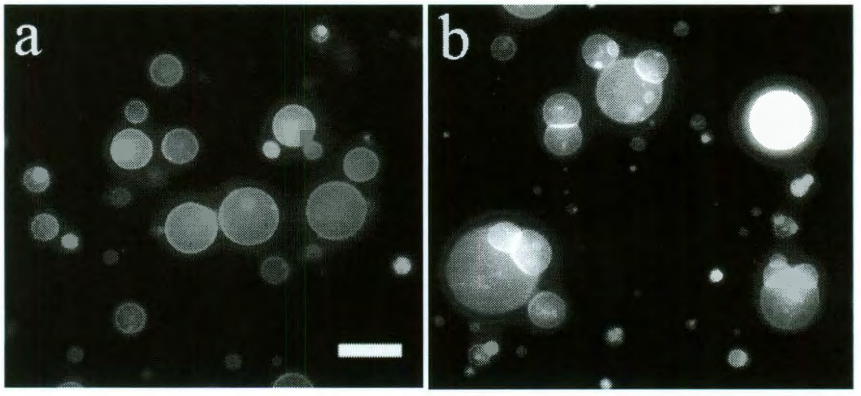

Figure 6-6 GUVs of SOPC spontaneously aggregated at pH 5 (right), but did not aggregate at pH 7 (left). Scale bar = 50 μm

pH induced adhesion did not produce hemifusion in all the lipid compositions we tested, including pure SOPC, SOPC/SOPE (4:1) and SOPC/cholesterol (4:1). The energies of adhesion for these lipid compositions at pH 5 are shown in Figure 6.7 and Table 6.1. There are small variations of adhesion energy with lipid compositions. The very large standard deviations (~50%) were due to very small suction pressures used (~ 0.5-2.5 mm water). The stability of the water manometer is ~ 0.2 mm.

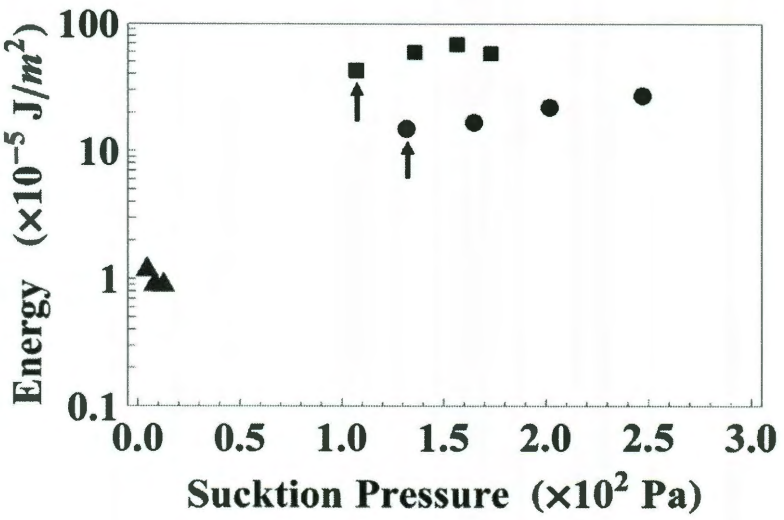

Figure 6-7 The energy of adhesion measured at different suction pressures. For clarity only one example is shown for each of three types of adhesion. For each stable adhesion, a series of equilibrium states were created at different suction pressures. The free energy of adhesion was calculated for each equilibrium state. Squares: GUVs of DOPC/DOPG (7:3) induced to adhere by TAT. Circles: GUVs of DOPC/DOPE/cholesterol (2:2:1) induced to hemifuse by PEG at pH 4. Triangles: SOPC GUVs adhered at pH 5.

6.4.2. Strong adhesion experiment

The strong adhesion was induced by introducing the mediators between two GUVs for a short period of time: less than 200 s for PEG and about 5 s for TAT. The mediator molecules that did not bind to the GUVs during that time were all dispersed to negligible concentrations. The PEG induced attraction created a temporary contact zone between two GUVs. As soon as the PEG injection stopped, the two GUVs detached from each other unless a hemifusion occurred. Hemifusion never occurred to GUVs of pure DOPC. For composition DOPC/DOPE/cholesterol

(2:2:1), hemifusion occurred at a random time during the injection of PEG solution, indicating a stochastic process. That cone-shaped lipids, such as PE and cholesterol, promoted hemifusion was expected [119]. However, hemifusion occurred only if the injected PEG solution was pH 4, not in any higher pH.

Table 1 Free energy of adhesion

	Average ($\times 10^{-5}$ J/m^2)	Standard deviation	Number of runs
Adhesion at pH 5			
SOPC	−1.72	0.90	6
SOPC/SOPE 4:1	−1.04	0.47	6
SOPC/Chol 4:1	−1.81	0.72	7
Hemifusion by PEG at pH 4			
DOPC/DOPE/Chol 2:2:1	−13.20	1.47	3
Adhesion by TAT at pH 7			
DOPC/DOPG 7:3	−50.08	8.32	5
Hemifusion by TAT at pH 7			
DOPC/DOPE/Chol/DOPG 2:2:1:1	−51.77	7.87	3

The TAT injection to anionic GUVs always created a stable contact zone. There is no hemifusion in the case of DOPC/DOPG (7:3). In the case of DOPC/DOPE/DOPG/cholesterol (2:2:1:1), the contact zone developed into hemifusion. We measured the energy of adhesion at the initial equilibrium state and also at a series of stable or metastable states created by increasing the suction pressure (Figure 6.7). For the cases of strong adhesion by TAT and the cases of hemifusion, increasing suction pressure would reduce the contact zone, which would require a small area of strongly adhered bilayers or hemifused bilayers

reversed to two separate bilayers. It is possible that the small dependence of γ on the suction pressure (Figure 6.7) reflected the incomplete reversibility during the experimental time. The average values given in Table 1 included only the measurements on the initial equilibrium states.

6.5. Discussion

It is clear from these examples that there are many molecular mediators that can cause interactions between lipid bilayers. The adhesion of SOPC vesicles was readily observable at pH lower than 5 (Figure 6.6). The low pH could be achieved by a buffer or by adding acid to the solution; the same adhesion phenomenon was observed. Previously Evans and Needham [17] measured the adhesion between two SOPC GUVs in 0.1 M NaCl (pH 7.0 buffer) and obtained an adhesion energy of $-1.3 \times 10^{-5}\, J/m^2$ comparable to our $\gamma = -(1.72 \pm 0.90)\, 10^{-5}\, J/m^2$. Perhaps H^+ and Na^+ ions have the same effect on SOPC, however the exact mechanism that causes the bilayer adhesion is not clear.

On the other hand, adhesion between anionic bilayers crossbridged by multivalent cations, such as La^{+3} [120] and Eu^{+3} [121], is known. We tested several cationic peptides for this effect: magainin which has +6 (including the N-terminus) and −1 charges in 23 amino acids, melittin which has +6 charges in 26 amino acids, and TAT which has +8 charges in 13 amino acids. Only TAT could induce adhesion between anionic lipids. Lastly, although PEG was expected to produce osmotic

depletion attraction between bilayers, it was a surprise to find that PEG at pH 4 (but not at any higher pH) induced hemifusion in PE/cholesterol containing lipids.

How to characterize each of such adhesions? We suggest that the most important characteristic is the free energy of adhesion and we have proposed methods that have successfully measured this property for all the examples discussed above. Our method can measure the adhesion energy as small as$-1 \times 10^{-5}\, J/m^2$ although subject to considerable errors due to the low pressure limit of the water manometer. We do not expect an upper limit on adhesion energy. It is clear that cross-bridging by TAT dominated the adhesion energy whether hemifusion or not. Thus TAT induced adhesion or hemifusion had a γ about $-50 \times 10^{-5}\, J/m^2$ whereas γ for hemifusion induced by PEG is about$-13 \times 10^{-5}\, J/m^2$. These values are to be compared with SOPC adhesion $\gamma = -12 \times 10^{-5}\, J/m^2$ under the effect of constant osmotic depletion force induced by 9.3g/100 cm^3 dextran (Mw 36500) measured by Evans and Needham [17]

Chapter 7

Conclusion

Our study combined three independent methods including x-ray diffraction, circular dichroism and micropipette aspiration method to investigate the peptide-membrane and drug-membrane interactions. X-ray diffraction and circular dichroism measured the systems in the equilibrium state while the GUV aspiration method provided the kinetic information during the interaction process. The results of the kinetic experiments are usually complex. In the literature there are often superficial inconsistencies between kinetic and equilibrium measurements, perhaps due to the fact that the potential barriers of the kinetic process obscure the energy levels seen in equilibrium. However, if the experiments are carefully done, and with the reference to the equilibrium studies, the complex behavior can be made

comprehensible. Here are the summaries of what we have learned by the combination of kinetic and equilibrium experiment.

7.1. Interaction of Curcumin with lipid bilayers

Curcumin binding to lipid bilayers follows the same binding pattern of amphipathic peptides[65]. Both curcumin and peptides initially bind to the interface and then at higher concentrations gradually partition to a state inserted into the hydrocarbon region. The main difference is that curcumin binds in both states as monomers. On the other hand, amphipathic peptides bind to the interface as monomers but insert into the hydrocarbon region to form pores, each composed of multiple peptides[73]. Although curcumin and antimicrobial peptides are both amphipathic molecules, curcumin is far more hydrophobic than the peptides (for example magainin, 23 amino-acids, carries +5 charges). Yet their binding behaviors to lipid bilayers are basically the same. This suggests that the two-state binding to lipid bilayers is typical of amphipathic molecules.

The combination of the X-ray experiment for membrane thickness changes and the GUV experiment for membrane area changes allows us to determine the numerical values for the relative binding energy $\varepsilon_S^o - \varepsilon_I^o$, and area expansions per molecule A_S and A_I. These values are important for quantitative understanding of interactions with membranes, such as molecular dynamics simulations. Also, the validity of both experimental results is reinforced by the mutual agreement.

Drug binding alters the physical properties of the lipid bilayer, including a decrease of the hydrocarbon thickness and softening of its elastic rigidity[1, 33]. Functions of some membrane proteins have been shown to depend on such physical properties of their host lipid bilayers, for example mechanosensitive channels[122] and gramicidin channels[1]. The result reported here suggests the possibility that drugs might influence functions of membrane proteins via their interactions with lipid bilayers.

7.2. Interaction of Tea catechin (-)-Epigallocatechin gallate with lipid bilayers

Experiments with antimicrobial peptides, curcumin, EGCg and Triton X100 showed that there are many types of membrane-active molecules. Their different characteristics are clarified most effectively by comparative studies. The combination of GUV kinetic experiment with X-ray measurement of the binding effect on membrane thickness has been very successful in revealing the molecular mechanism of membrane-active molecules [31, 32]. Antimicrobial peptides bind to the interface of membranes, but they make a transition to form stable finite-sized pores in membranes when the concentration exceeds a critical value [31]. Curcumin binds to the membranes in two states, first on the interface and then in the hydrocarbon region [32]. Triton X100 strongly solubilizes lipid bilayers when its concentration is above its CMC; but below CMC it incorporates into the lipid bilayers. EGCg binds only to the interface of membranes but also solubilizes the lipid

molecules. Its effect of membrane area expansion is one order of magnitude smaller than the similar size curcumin, and its solubilization effect is mild compared with Triton.

EGCg is known to inhibit growth of both Gram-positive and Gram-negative bacteria when added into the bacterial culture medium, and these antibacterial effects were correlated with some measured effects of EGCg on lipid bilayers [21-23, 25-28, 30]. These effects included binding coefficients [25-27], leakage from vesicles [21, 22], ^{31}P chemical shift and ^{2}H quadrupole splitting by NMR [28] and spin probe parameter by electron paramagnetic resonance [30]. Recently Tamba et al. [29] suggested that the bursting of GUVs by EGCg is a possible mechanism for catchins' antibacterial activity. However, the GUV bursting was observed only at high EGCg concentrations (>30 μM). The results presented here helps clarifying the molecular effect of EGCg on lipid bilayers. We hope that the understanding of the molecular effect of EGCg on lipid bilayers will help clarifying the molecular mechanism of its antibacterial effect.

7.3. Kinetic process of β-Amyloid formation via membrane binding

One important question about membrane-active peptides is how their interactions depend on the lipid properties, such as the lipid charge. Typical membrane-active peptides, e.g., antimicrobial peptides and cell-penetrating

peptides, are cationic, whereas the charge on cell membranes are either neutral or anionic. Accumulated evidence has now clarified the role of the charge on the lipid headgroup. The charge on the lipid headgroup could increases the apparent partition coefficients to anionic lipids by three to five orders of magnitude over that to neutral lipids [100, 123] (note that the apparent partition coefficients to anionic lipids are not constant of peptide concentration . [100, 123]) Persson et al. [92], Beschiaschvili and Seelig [100], and Wieprecht and Seelig [123] have shown that if one excludes the effect of the electrostatic attraction, the surface partition constants (i.e., that measured from the peptide concentration in the vicinity of the vesicle surface) to neutral and anionic lipids are almost the same. The next question is how the peptide interaction after binding depends on the lipid charge. Tamba and Yamazaki [124] have shown that the rate of pore formation by antimicrobial peptide magainin is the same on neutral or anionic lipids, if the peptide concentrations on the surface of the vesicles are the same. Our study here showed that penetratin interactions with DOPC and DOPC/DOPG, both inducing β-amyloid formation via membrane thinning, are closely similar. Peptide-lipid interactions after the interfacial binding typically manifest in membrane thinning and a transition of peptide from its interfacial binding state, to pore formation in the case of antimicrobial peptides or to β-aggregates in the case of penetratin. These after-binding peptide-lipid interactions are largely independent of the charge on the lipid headgroups.

Kinetic processes are often dominated by potential barriers that are absent in equilibrium measurements. Therefore superficial comparison of kinetic and equilibrium results could lead to contradictions. Here we show that kinetic experiments with GUVs can be directly correlated to equilibrium measurements of peptide-lipid mixtures through the variable $\Delta A/A$. The same correlated studies were previously performed with melittin. The comparison of these two cases revealed a striking difference between these two peptides. In the case of melittin, the critical value of $\Delta A/A$ when melittin formed pores in GUVs was the same as measured in the peptide-lipid mixtures [31]. In the case of penetratin, the critical value of $\Delta A/A$ when penetratin changed from α monomers to β aggregates in GUVs is roughly one-half of the critical value measured in peptide-lipid mixtures. The crucial difference seems to be whether the peptide translocates across the bilayer after binding. Melittin seemed to have translocated and distributed symmetrically across the bilayer of the GUV. In contrast, penetratin appeared to have bound to the outer leaflet of the bilayer without translocation. As a result, the elastic energy of membrane expansion per peptide incurred by penetratin in asymmetric binding is twice as large as the value for symmetrically bound penetratin. Superficially penetratin and melittin are similar except for their charge densities: 7+ out of 16 amino acids for penetratin and 6+ out of 26 for melittin. Melittin is a pore forming peptide, penetratin is not [92, 102, 103]. Whether the charge density is the key parameter that makes the properties of these two peptides so drastically different in their interactions with membranes is an intriguing question.

7.4. On free energy of adhesion and hemifusion

We modified the aspiration method to measure the adhesion and hemifusion energy of lipid bilayers. The methods we discussed here are relevant to some crucial questions in the field of membrane fusion research. Membrane fusion is a complicated yet ubiquitous process constantly occurring in eukaryotic cells. Very active research on this subject in the last two decades has clarified the roles of various fusion proteins [125-131]. There is now a converging view that the formation of fusion protein complexes [104, 126, 129, 132] exerts a force to pull two membranes to close proximity. The fusion proteins are anchored to the fusing membranes via a transmembrane domain or a fusion peptide. However, exactly how the proteins manipulate the two lipid bilayers to merge remains unclear. Three questions relevant to our discussion are: 1) How do the two lipid bilayers come into contact? 2) What causes the transition to hemifusion? 3) Is the hemifusion intermediate state a free energy barrier, as often suggested ?

Despite the fact that cell membranes are generally covered by carbohydrates glycosylated to lipids and proteins, it is commonly believed that one of the key steps during membrane fusion involves the creation of a protein-denuded contact zone in each of the two fusing membranes so as to allow bilayer-bilayer contact and merger [129]. However, since the bulky fusion-protein complexes are between the two membranes, what causes the bilayer-bilayer contact has been a major puzzle [129, 132]. Could it be that fusion proteins simply need to pin two bilayers together long enough and the bilayers would do the rest spontaneously [132]? Or, the fusion

proteins play an active role directing the contact and merger between two bilayers [132]? Thus mediated adhesion between bilayers discussed here could be a factor for membrane fusion, particularly at low pH.

It is now believed that most, if not all, biological membrane fusion proceeds through a hemifusion intermediate [113]. The structure of this fusion intermediate called a stalk has been confirmed by X-ray diffraction [133]. In fact the stalk structure was theoretically predicted [38] almost twenty years before the confirmation by experiment [133]. However, there is wide theoretical disagreement about the free energy level of hemifusion [38-43]. This is not merely a theoretical curiosity. Knowing the energy levels of the intermediate states is a helpful guide to understand the actions of fusion proteins. The methods demonstrated here suggest a way for systematic measurements to resolve the energy issue for the intermediate states of lipid transformation during membrane fusion.

References

1. Ingolfsson, H.I., R.E. Koeppe, 2nd, and O.S. Andersen, *Curcumin is a modulator of bilayer material properties.* Biochemistry, 2007. 46(36): p. 10384-91.
2. Wiggins, P. and R. Phillips, *Analytic models for mechanotransduction: gating a mechanosensitive channel.* Proc Natl Acad Sci U S A, 2004. 101(12): p. 4071-6.
3. Zhou, Y. and R.M. Raphael, *Effect of salicylate on the elasticity, bending stiffness, and strength of SOPC membranes.* Biophys J, 2005. 89(3): p. 1789-801.
4. Lee, C.C., Y. Sun, and H.W. Huang, *Membrane-mediated peptide conformation change from alpha-monomers to beta-aggregates.* Biophys J, 2010. 98(10): p. 2236-45.
5. Wu, Y., H.W. Huang, and G.A. Olah, *Method of oriented circular dichroism.* Biophys J, 1990. 57: p. 797-806.
6. Ludtke, S., K. He, and H. Huang, *Membrane thinning caused by magainin 2.* Biochemistry, 1995. 34(51): p. 16764-9.
7. Yang, L., et al., *Barrel-stave model or toroidal model? a case study on melittin pores.* Biophys J, 2001. 81: p. 1475-1485.
8. Heller, W.T., et al., *Multiple states of beta-sheet peptide protegrin in lipid bilayers.* Biochemistry, 1998. 37(49): p. 17331-8.
9. Weiss, T.M., et al., *Two states of cyclic antimicrobial peptide RTD-1 in lipid bilayers.* Biochemistry, 2002. 41(31): p. 10070-6.
10. Wu, Y., et al., *X-ray Diffraction Study of Lipid Bilayer Membrane Interacting with Amphiphilic Helical Peptides: Diphytanoyl Phosphatidylcholine with Alamethicin at Low Concentrations.* Biophys J, 1995. 68: p. 2361-2369.
11. Ludtke, S.J., et al., *Membrane pores induced by magainin.* Biochemistry, 1996. 35(43): p. 13723-8.
12. Heller, W.T., et al., *Membrane thinning effect of the beta-sheet antimicrobial protegrin.* Biochemistry, 2000. 39(1): p. 139-45.
13. Chen, F.Y., M.T. Lee, and H.W. Huang, *Evidence for membrane thinning effect as the mechanism for peptide-induced pore formation.* Biophys J, 2003. 84(6): p. 3751-8.
14. Evans, E. and D. Needham, *Physical properties of surfactant bilayer membranes: thermal transitions, elasticity, rigidity, cohesion, and colloidal interactions.* Journal of Physical Chemistry, 1987. 91: p. 4219-4228.
15. Rawicz, W., et al., *Effect of chain length and unsaturation on elasticity of lipid bilayers.* Biophys J, 2000. 79(1): p. 328-39.

16. Evans, E. and M. Metcalfe, *Free energy potential for aggregation of giant, neutral lipid bilayer vesicles by Van der Waals attraction.* Biophys J, 1984. 46(3): p. 423-6.
17. Evans, E. and D. Needham, *Attraction between lipid bilayer membranes in concentrated solutions of nonadsorbing polymers: comparison of mean-field theory with measurements of adhesion energy.* Macromolecules, 1988. 21: p. 1822-1831.
18. Evans, E., D. Needham, and J. Janzen, *Nonspecific adhesion of phospholipid bilayer membranes in solutions of plasma proteins: Measurement of free energy potentials and theoretical concepts.*, in *In Proteins at Interfaces*, J. Brash and T. Horbett, Editors. 1987, American Chemical Society: Washington DC. p. 88-102.
19. Jaruga, E., et al., *Apoptosis-independent alterations in membrane dynamics induced by curcumin.* Exp Cell Res, 1998. 245(2): p. 303-12.
20. Khajavi, M., et al., *Oral curcumin mitigates the clinical and neuropathologic phenotype of the Trembler-J mouse: a potential therapy for inherited neuropathy.* Am J Hum Genet, 2007. 81(3): p. 438-53.
21. Caturla, N., et al., *The relationship between the antioxidant and the antibacterial properties of galloylated catechins and the structure of phospholipid model membranes.* Free Radic Biol Med, 2003. 34(6): p. 648-62.
22. Ikigai, H., et al., *Bactericidal catechins damage the lipid bilayer.* Biochim Biophys Acta, 1993. 1147(1): p. 132-6.
23. Kitano, K., et al., *Sealing effects of (-)-epigallocatechin gallate on protein kinase C and protein phosphatase 2A.* Biophys Chem, 1997. 65(2-3): p. 157-64.
24. Tsuchiya, H., *Effects of green tea catechins on membrane fluidity.* Pharmacology, 1999. 59(1): p. 34-44.
25. Hashimoto, T., et al., *Interaction of tea catechins with lipid bilayers investigated with liposome systems.* Biosci Biotechnol Biochem, 1999. 63(12): p. 2252-5.
26. Kajiya, K., S. Kumazawa, and T. Nakayama, *Steric effects on interaction of tea catechins with lipid bilayers.* Biosci Biotechnol Biochem, 2001. 65(12): p. 2638-43.
27. Kajiya, K., et al., *Relationship between antibacterial activity of (+)-catechin derivatives and their interaction with a model membrane.* J Agric Food Chem, 2004. 52(6): p. 1514-9.
28. Kumazawa, S., et al., *Direct evidence of interaction of a green tea polyphenol, epigallocatechin gallate, with lipid bilayers by solid-state Nuclear Magnetic Resonance.* Biosci Biotechnol Biochem, 2004. 68(8): p. 1743-7.
29. Tamba, Y., et al., *Single GUV method reveals interaction of tea catechin (-)-epigallocatechin gallate with lipid membranes.* Biophys J, 2007. 92(9): p. 3178-94.

30. Yoshioka, H., et al., *Interaction of (+)-catechin with a lipid bilayer studied by the spin probe method.* Biosci Biotechnol Biochem, 2006. 70(2): p. 395-400.
31. Lee, M.T., et al., *Mechanism and kinetics of pore formation in membranes by water-soluble amphipathic peptides.* Proc Natl Acad Sci U S A, 2008. 105(13): p. 5087-92.
32. Sun, Y., et al., *The bound states of amphipathic drugs in lipid bilayers: study of curcumin.* Biophys J, 2008. 95(5): p. 2318-24.
33. Hung, W.C., et al., *Membrane-thinning effect of curcumin.* Biophys J, 2008. 94(11): p. 4331-8.
34. Jarrett, J.T. and P.T. Lansbury, Jr., *Seeding "one-dimensional crystallization" of amyloid: a pathogenic mechanism in Alzheimer's disease and scrapie?* Cell, 1993. 73(6): p. 1055-8.
35. Kuhl, T., et al., *Direct measurement of polyethylene glycol induced depletion attraction between lipid bilayers.* Langmuir, 1996. 12: p. 3003-3014.
36. Rand, R.P. and V.A. Parsegian, *Hydration forces between phospholipid bilayers.* Biochim Biophys Acta, 1989. 988: p. 351-376.
37. Helfrich, W., *Steric interaction of fluid membranes in multilayer systems.* Z. Naturforsch, 1978. 33a: p. 305-315.
38. Markin, V.S., M.M. Kozlov, and V.L. Borovjagin, *On the theory of membrane fusion: The stalk mechanism.* Gen. Physiol. Biophys., 1984. 3: p. 361-377.
39. Siegel, D.P., *Energetics of intermediates in membrane fusion: comparison of stalk and inverted micellar intermediate mechanisms.* Biophys J, 1993. 65(5): p. 2124-40.
40. Kuzmin, P.I., et al., *A quantitative model for membrane fusion based on low-energy intermediates.* Proc Natl Acad Sci U S A, 2001. 98(13): p. 7235-40.
41. Kozlovsky, Y. and M.M. Kozlov, *Stalk model of membrane fusion: solution of energy crisis.* Biophys J, 2002. 82(2): p. 882-95.
42. Markin, V.S. and J.P. Albanesi, *Membrane fusion: stalk model revisited.* Biophys J, 2002. 82(2): p. 693-712.
43. Lentz, B.R., D.P. Siegel, and V. Malinin, *Filling potholes on the path to fusion pores.* Biophys J, 2002. 82(2): p. 555-7.
44. Bagatolli, L.A., *To see or not to see: Lateral organization of biological membranes and fluorescence microscopy.* Biochimica Et Biophysica Acta-Biomembranes, 2006. 1758(10): p. 1541-1556.
45. Angelova, M.I., *Liposome Electroformation*, in *Giant Vesicles*, P.L. Luisi and P. Walde, Editors. 2000, John Wiley & Sons: Chichester. p. pp. 27-36.
46. Fygenson, D.K., et al., *Microtubules and vesicles under controlled tension.* Phys. Rev. E, 1997. 55: p. 850-859.

47. Joe, B., M. Vijaykumar, and B.R. Lokesh, *Biological properties of curcumin-cellular and molecular mechanisms of action.* Crit Rev Food Sci Nutr, 2004. 44(2): p. 97-111.
48. Harroun, T.A., et al., *Experimental evidence for hydrophobic matching and membrane-mediated interactions in lipid bilayers containing gramicidin.* Biophys J, 1999. 76(2): p. 937-45.
49. Blaurock, A.E., *Structure of the nerve myelin membrane: proof of the low-resolution profile.* J Mol Biol, 1971. 56(1): p. 35-52.
50. Olah, G.A., et al., *Location of ion-binding sites in the gramicidin channel by X-ray diffraction.* J Mol Biol, 1991. 218(4): p. 847-58.
51. Sheetz, M.P. and S.J. Singer, *Biological membranes as bilayer couples. A molecular mechanism of drug-erythrocyte interactions.* Proc Natl Acad Sci U S A, 1974. 71(11): p. 4457-61.
52. Maheshwari, R.K., et al., *Multiple biological activities of curcumin: a short review.* Life Sciences, 2005. 78: p. 2081-2087.
53. Mall, M. and K. Kunzelmann, *Correction of the CF defect by curcumin: hypes and disappointments.* Bioessays, 2005. 27(1): p. 9-13.
54. Oetari, S., et al., *Effects of curcumin on cytochrome P450 and glutathione S-transferase activities in rat liver.* Biochem Pharmacol, 1996. 51(1): p. 39-45.
55. Longo, M.L., et al., *Area expansion and permeation of phospholipid membrane bilayer by influenza fusion peptides and melittin.* Langmuir, 1998. 14: p. 2385-2395.
56. Tennesen, H.H., *Solubility, chemical and photochemical stability of curcumin in surfactant solutions. Studies of curcumin and curcuminoids, XXVIII.* Pharmazie, 2002. 57: p. 820-824.
57. Kwok, R. and E. Evans, *Thermoelasticity of large lecithin bilayer vesicles.* Biophys J, 1981. 35(3): p. 637-52.
58. Hwang, T.C., R.E. Koeppe, 2nd, and O.S. Andersen, *Genistein can modulate channel function by a phosphorylation-independent mechanism: importance of hydrophobic mismatch and bilayer mechanics.* Biochemistry, 2003. 42(46): p. 13646-58.
59. Seemann, H. and R. Winter, *Volumetric properties, compressibilities, and volume flucturations in phospholipid-cholesterol bilayers.* Z. Phys. Chem., 2003. 217: p. 831-846.
60. Zasloff, M., *Antimicrobial peptides of multicellular organisms.* Nature, 2002. 415(6870): p. 389-95.
61. Banerjee, U., et al., *Interaction of alamethicin with lecithin bilayers: a 31P and 2H NMR study.* Biochemistry, 1985. 24(26): p. 7621-7.
62. Huang, H.W. and Y. Wu, *Lipid-alamethicin interactions influence alamethicin orientation.* Biophys J, 1991. 60: p. 1079-1087.
63. Ludtke, S.J., et al., *Cooperative membrane insertion of magainin correlated with its cytolytic activity.* Biochim Biophys Acta, 1994. 1190(1): p. 181-4.

64. Israelachvili, J., *Intermolecular & Surface Forces*. 2nd Edition ed. 1991, London: Academic Press.
65. Lee, M.T., F.Y. Chen, and H.W. Huang, *Energetics of pore formation induced by membrane active peptides.* Biochemistry, 2004. 43(12): p. 3590-9.
66. Armen, R.S., O.D. Uitto, and S.E. Feller, *Phospholipid component volumes: determination and application to bilayer structure calculations.* Biophys J, 1998. 75(2): p. 734-44.
67. Tonnesen, H.H., J. Karlsen, and A. Mostad, *Structural studies of curcuminoids. I. The crystal structure of curcumin.* Acta Chemica Scandinavica, 1982. B36: p. 475-479.
68. Chung, J.Y., et al., *Inhibition of activator protein 1 activity and cell growth by purified green tea and black tea polyphenols in H-ras-transformed cells: structure-activity relationship and mechanisms involved.* Cancer Res, 1999. 59(18): p. 4610-7.
69. Tamba, Y. and M. Yamazaki, *Single giant unilamellar vesicle method reveals effect of antimicrobial peptide magainin 2 on membrane permeability.* Biochemistry, 2005. 44(48): p. 15823-33.
70. Nomura, F., et al., *Capabilities of liposomes for topological transformation.* Proc Natl Acad Sci U S A, 2001. 98(5): p. 2340-5.
71. Urbaneja, M.A., F.M. Goni, and A. Alonso, *Structural changes induced by Triton X-100 on sonicated phosphatidylcholine liposomes.* Eur J Biochem, 1988. 173(3): p. 585-8.
72. Zasloff, M., *Magainins, a class of antimicrobial peptides from Xenopus skin: isolation, characterization of two active forms, and partial cDNA sequence of a precursor.* Proc Natl Acad Sci U S A, 1987. 84(15): p. 5449-53.
73. Huang, H.W., *Action of antimicrobial peptides: two-state model.* Biochemistry, 2000. 39(29): p. 8347-52.
74. Huang, H.W., *Molecular mechanism of antimicrobial peptides: the origin of cooperativity.* Biochim Biophys Acta, 2006. 1758(9): p. 1292-302.
75. Nagle, J.F. and S. Tristram-Nagle, *Structure of lipid bilayers.* Biochim Biophys Acta, 2000. 1469(3): p. 159-95.
76. Simon, S., T.J. McIntosh, and R. Lattore, *Influence of cholesterol on water penetration into bilayers.* Science, 1982. 216: p. 65-68.
77. Lee, M.T., et al., *Many-body effect of antimicrobial peptides: on the correlation between lipid's spontaneous curvature and pore formation.* Biophys J, 2005. 89(6): p. 4006-16.
78. Heinrich, V., S. Svetina, and B. Zeks, *Nonaxisymmetric Vesicle Shapes in a Generalized Bilayer-Couple Model and the Transition between Oblate and Prolate Axisymmetrical Shapes.* Physical Review E, 1993. 48(4): p. 3112-3123.
79. Miao, L., et al., *Budding Transitions of Fluid-Bilayer Vesicles - the Effect of Area-Difference Elasticity.* Physical Review E, 1994. 49(6): p. 5389-5407.

80. Rodriguez, N., et al., *Indirect evidence of submicroscopic pores in giant unilamellar [correction of unilamelar] vesicles.* Biochim Biophys Acta, 2005. 1724(3): p. 281-7.
81. Miao, L., et al., *Equilibrium Budding and Vesiculation in the Curvature Model of Fluid Lipid Vesicles.* Physical Review A, 1991. 43(12): p. 6843-6856.
82. Seifert, U., K. Berndl, and R. Lipowsky, *Shape Transformations of Vesicles - Phase-Diagram for Spontaneous-Curvature and Bilayer-Coupling Models.* Physical Review A, 1991. 44(2): p. 1182-1202.
83. Brochard-Wyart, F., P.G. de Gennes, and O. Sander, *Transient pores in stretched vesicles: role of leak-0ut.* Physica, 2000. A 278: p. 32-51.
84. Evans, E., et al., *Dynamic tension spectroscopy and strength of biomembranes.* Biophys J, 2003. 85(4): p. 2342-50.
85. Derossi, D., et al., *The third helix of the Antennapedia homeodomain translocates through biological membranes.* J Biol Chem, 1994. 269(14): p. 10444-50.
86. Terzi, E., G. Holzemann, and J. Seelig, *Self-association of beta-amyloid peptide (1-40) in solution and binding to lipid membranes.* J Mol Biol, 1995. 252(5): p. 633-42.
87. Terzi, E., G. Holzemann, and J. Seelig, *Interaction of Alzheimer beta-amyloid peptide(1-40) with lipid membranes.* Biochemistry, 1997. 36(48): p. 14845-52.
88. Magzoub, M., L.E. Eriksson, and A. Graslund, *Conformational states of the cell-penetrating peptide penetratin when interacting with phospholipid vesicles: effects of surface charge and peptide concentration.* Biochim Biophys Acta, 2002. 1563(1-2): p. 53-63.
89. Magzoub, M., L.E. Eriksson, and A. Graslund, *Comparison of the interaction, positioning, structure induction and membrane perturbation of cell-penetrating peptides and non-translocating variants with phospholipid vesicles.* Biophys Chem, 2003. 103(3): p. 271-88.
90. Lindberg, M., et al., *Structure and positioning comparison of two variants of penetratin in two different membrane mimicking systems by NMR.* Eur J Biochem, 2003. 270(14): p. 3055-63.
91. Wong, P.T., et al., *Amyloid-beta membrane binding and permeabilization are distinct processes influenced separately by membrane charge and fluidity.* J Mol Biol, 2009. 386(1): p. 81-96.
92. Persson, D., et al., *Application of a novel analysis to measure the binding of the membrane-translocating peptide penetratin to negatively charged liposomes.* Biochemistry, 2003. 42(2): p. 421-9.
93. Qian, Y.Q., et al., *The structure of the Antennapedia homeodomain determined by NMR spectroscopy in solution: comparison with prokaryotic repressors.* Cell, 1989. 59(3): p. 573-80.

94. Melikov, K. and L.V. Chernomordik, *Arginine-rich cell penetrating peptides: from endosomal uptake to nuclear delivery.* Cell Mol Life Sci, 2005. 62(23): p. 2739-49.
95. Fischer, R., et al., *Break on through to the other side-biophyiscs and cell biology shet light on cell-penetrating peptides.* Chembiochem, 2006. 6: p. 2126-2142.
96. Duchardt, F., et al., *A comprehensive model for the cellular uptake of cationic cell-penetrating peptides.* Traffic, 2007. 8(7): p. 848-66.
97. Chen, F.Y., W.C. Hung, and H.W. Huang, *Critical swelling of phospholipid bilayers.* Phys. Rev. Lett., 1997. 79: p. 4026-4029.
98. Warren, B.E., *X-ray Diffraction.* 1990, Mineola, N.Y.; pp. 41-47, 51-54.: Dover Publications,. pp. 41-47, 51-54.
99. Huang, H.W., *Free energies of molecular bound states in lipid bilayers: lethal concentrations of antimicrobial peptides.* Biophys J, 2009. 96(8): p. 3263-72.
100. Beschiaschvili, G. and J. Seelig, *Melittin binding to mixed phosphatidylglycerol/phosphatidylcholine membranes.* Biochemistry, 1990. 29(1): p. 52-8.
101. Wenk, M.R. and J. Seelig, *Magainin 2 amide interaction with lipid membranes: calorimetric detection of peptide binding and pore formation.* Biochemistry, 1998. 37(11): p. 3909-16.
102. Drin, G., et al., *Translocation of the pAntp peptide and its amphipathic analogue AP-2AL.* Biochemistry, 2001. 40(6): p. 1824-34.
103. Thoren, P.E., et al., *The antennapedia peptide penetratin translocates across lipid bilayers - the first direct observation.* FEBS Lett, 2000. 482(3): p. 265-8.
104. Hernandez, L.D., et al., *Virus-cell and cell-cell fusion.* Annu Rev Cell Dev Biol, 1996. 12: p. 627-61.
105. Chernomordik, L.V., et al., *An early stage of membrane fusion mediated by the low pH conformation of influenza hemagglutinin depends upon membrane lipids.* J Cell Biol, 1997. 136(1): p. 81-93.
106. Zhou, Y. and R.M. Raphael, *Solution pH alters mechanical and electrical properties of phosphatidylcholine membranes: relation between interfacial electrostatics, intramembrane potential, and bending elasticity.* Biophys J, 2007. 92(7): p. 2451-62.
107. Console, S., et al., *Antennapedia and HIV transactivator of transcription (TAT) "protein transduction domains" promote endocytosis of high molecular weight cargo upon binding to cell surface glycosaminoglycans.* J Biol Chem, 2003. 278(37): p. 35109-14.
108. Richard, J.P., et al., *Cellular uptake of unconjugated TAT peptide involves clathrin-dependent endocytosis and heparan sulfate receptors.* J Biol Chem, 2005. 280(15): p. 15300-6.

109. Wadia, J.S., R.V. Stan, and S.F. Dowdy, *Transducible TAT-HA fusogenic peptide enhances escape of TAT-fusion proteins after lipid raft macropinocytosis.* Nat Med, 2004. 10(3): p. 310-5.
110. Yang, S.T., et al., *Cell-penetrating peptide induces leaky fusion of liposomes containing late endosome-specific anionic lipid.* Biophys. J., 2010. 99: p. 2525-2533.
111. Evans, E.A., *Analysis of adhesion of large vesicles to surfaces.* Biophys J, 1980. 31(3): p. 425-31.
112. Evans, E. and M. Metcalfe, *Free energy potential for aggregation of mixed phosphatidylcholine/phosphatidylserine lipid vesicles in glucose polymer (dextran) solutions.* Biophys J, 1984. 45(4): p. 715-20.
113. Chernomordik, L.V. and M.M. Kozlov, *Mechanics of membrane fusion.* Nat Struct Mol Biol, 2008. 15(7): p. 675-83.
114. Heuvingh, J., F. Pincet, and S. Cribier, *Hemifusion and fusion of giant vesicles induced by reduction of inter-membrane distance.* Eur Phys J E Soft Matter, 2004. 14(3): p. 269-76.
115. Sun, Y., et al., *Interaction of tea catechin (-)-epigallocatechin gallate with lipid bilayers.* Biophys J, 2009. 96(3): p. 1026-35.
116. Sun, Y., et al., *Kinetic Process of beta-Amyloid Formation via Membrane Binding.* Biophys J, 2010. 99(2): p. 544-552.
117. Zhelev, D.V. and D. Needham, *Tension-stabilized pores in giant vesicles: determination of pore size and pore line tension.* Biochim Biophys Acta, 1993. 1147(1): p. 89-104.
118. Glazer, A.N. and K.H. Mc, *The denaturation of proteins. IV. Conalbumin and iron(III)-conalbumin in urea solution.* Biochim Biophys Acta, 1963. 71: p. 109-23.
119. Chernomordik, L., et al., *The hemifusion intermediate and its conversion to complete fusion: regulation by membrane composition.* Biophys J, 1995. 69(3): p. 922-9.
120. Tanaka, T. and M. Yamazaki, *Membrane fusion of giant unilamellar vesicles of neutral phospholipid membranes induced by La3+.* Langmuir, 2004. 20(13): p. 5160-4.
121. Haluska, C.K., et al., *Time scales of membrane fusion revealed by direct imaging of vesicle fusion with high temporal resolution.* Proc Natl Acad Sci U S A, 2006. 103(43): p. 15841-6.
122. Sukharev, S., et al., *The gating mechanism of the large mechanosensitive channel MscL.* Nature, 2001. 409(6821): p. 720-4.
123. Wieprecht, T. and J. Seelig, *Isothermal titration calorimetry for studying interactions between peptides and lipid membranes.* Current Topics in Membranes, 2002. 52: p. 31-56.
124. Tamba, Y. and M. Yamazaki, *Magainin 2-induced pore formation in the lipid membranes depends on its concentration in the membrane surface.* J. Phys. Chem. B, 2009. 113: p. 4846-4852.

125. Sollner, T., et al., *SNAP receptors implicated in vesicle targeting and fusion.* Nature, 1993. 362(6418): p. 318-24.
126. Sudhof, T.C. and J.E. Rothman, *Membrane fusion: grappling with SNARE and SM proteins.* Science, 2009. 323(5913): p. 474-7.
127. Rizo, J. and C. Rosenmund, *Synaptic vesicle fusion.* Nat Struct Mol Biol, 2008. 15(7): p. 665-74.
128. Wickner, W. and R. Schekman, *Membrane fusion.* Nat Struct Mol Biol, 2008. 15(n7): p. 658-664.
129. Martens, S. and H.T. McMahon, *Mechanisms of membrane fusion: disparate players and common principles.* Nat Rev Mol Cell Biol, 2008. 9(7): p. 543-56.
130. Giraudo, C.G., et al., *Alternative zippering as an on-off switch for SNARE-mediated fusion.* Science, 2009. 323(5913): p. 512-6.
131. Maximov, A., et al., *Complexin controls the force transfer from SNARE complexes to membranes in fusion.* Science, 2009. 323(5913): p. 516-21.
132. McNew, J.A., et al., *Close is not enough: SNARE-dependent membrane fusion requires an active mechanism that transduces force to membrane anchors.* J Cell Biol, 2000. 150(1): p. 105-17.
133. Yang, L. and H.W. Huang, *Observation of a membrane fusion intermediate structure.* Science, 2002. 297: p. 1877-1879.

Appendix A

Experiments with pore-forming proteins BAX and diphtheria toxin

The BCL-2 family controls the cell death by governing mitochondrial outer membrane permeabilization. The BCL-2 family proteins are central regulators of apoptosis and can be either pro-apoptotic (BAX, BAD, BCL-X_S, BAK, BIK, BID) or anti-apoptotic (BCL-2, BCL- X_l, MCL-1, A1). The BCL-2 family has a common structure that consists of a hydrophobic helix surrounded by amphipathic helices. They possess one or more conserved BCL-2 homology (BH) domains designated BH1, BH2, BH3, and BH4, which correspond to α-helical segments. BAX is a pro-apoptotic member in the Bcl-2 family containing BH1, BH2 and BH3 domains. In a healthy cell, inactive BAX is located in the cytoplasm. During the process of programmed cell death, BAX is activated and translocates to the outer mitochondrial membrane and inserts as a monomer. After undergoing oligmerization, BAX forms pores in the outer mitochondrial membrane to release cytochrome c and other apoptotic factors into the cytoplasm. In the cytoplasm, the caspases will be activated by those apoptotic factors and then execute the cell death process. However, the mechanism of pore forming and the interaction of BAX proteins in the membrane are still unclear.

Here, we want to study how BAX protein interacts with membrane and also the mechanism of pore forming. We have proven that antimicrobial peptides, such as magainin, alamethicin and melittin, can form pores in the membranes requiring

only four (or more) helices in the pore. Peptide monomers binding at the bilayer interface incur an elastic energy of stretching the membrane area; therefore the chemical potential of the monomers on the interface includes an elastic energy term depending on peptide-lipid ratio P/L. Similar to those antimicrobial peptides, BAX composed by nine α helices. We can imagine BAX as a string of amphipathic helical segments connected by flexible joints. We believe that the protein binds to a bilayer with each segment adsorbs at the bilayer interface. Then the difference between antimicrobial peptides and BAX could be that: the critical concentration for peptides is P/L for the entire membrane (or a membrane domain), whereas BAX can achieve the critical P/L locally by a few BAXs. We would like to verify this hypothesis by measuring the critical P/L when BAX interacts with membrane and compare the results with antimicrobial peptides.

Two methods were used to look for the clue of how BAX forms pores. In the first method, we used content dye inside the GUVs and transferred them into another chamber containing 0.5 μM BAX protein, 10mM pH7 HEPES, 50mM NaCl and 100mM glucose. The GUVs then sank to the bottom of the chamber due to the sucrose solution inside the GUVs being denser than the glucose solution outside. We observed the leakage of the content dye from the GUVs in real time (figure A1). We proved that BAXs formed stable pores in GUVs and the pores were formed stochastically. By the stable leakage of the content dye from the GUV, we also proved that the BAX has been properly activated. The BAX used in this experiment was supplied by our collaborator Dr. Paul H. Schlesinger of Washington University.

Before each experimen, we activated BAX by 2% Octyl Glucoside(OG) for two hours and then diluted for 100 times in buffer solution. The final concentration of OG was about 0.7mM which is much lower than the critical micelle concentration (CMC) of OG (~20-25mM). Studies found no bilayer solubilization at OG concentrations below its critical micelle concentration.

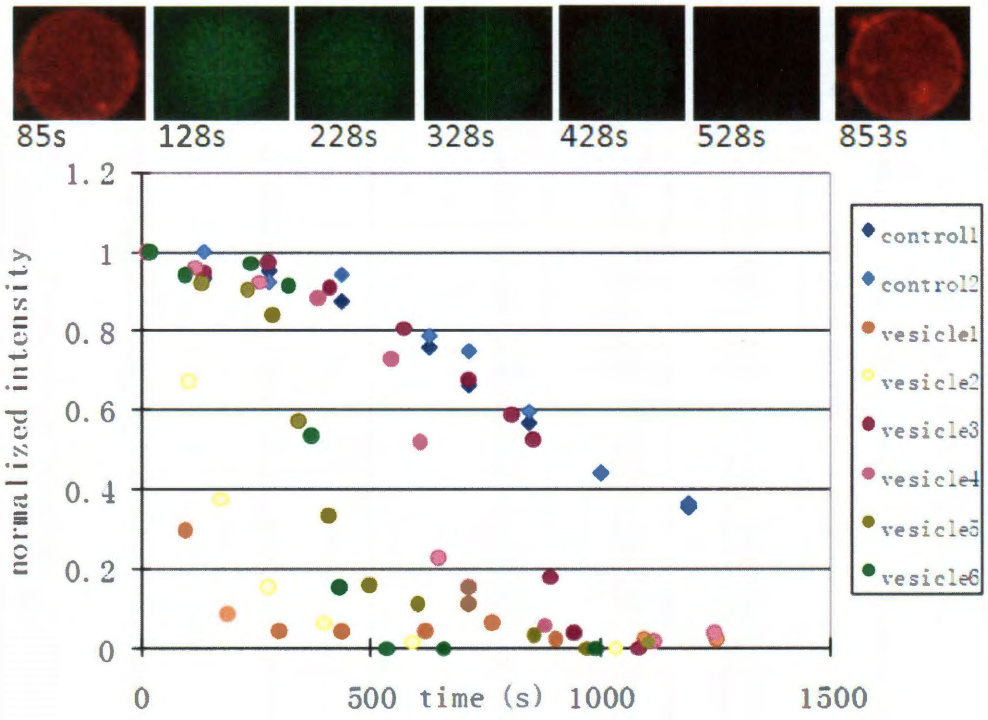

Figure A 1 (up) A GUV with calcein (green) in its interior content and Rh-DOPE on its surface (red) was exposed to 0.5 μM BAX. Leakage occurred stochastically. (below) Time course of the content dye leakage.

In the second method, we used two chamber aspiration method as described in this thesis. A chosen GUV were aspirated by a micropipette at a constant pressure and then transferred to another chamber containing 0.5 μM BAX protein (with 0.68mM OG), 10mM pH7 HEPES, 50mM NaCl and 100mM glucose. The corresponding area or volume change was measured as a function of time after the GUV was exposed to the BAX solution (figure A2). The surface area of the GUV first increased due to the binding of BAXs on the bilayer interface. The area increase ΔA was calculated from the increase of the protrusion length ΔL_P at constant vesicle volume: $\Delta A = 2\pi R_P(1\ R_P/R_V)\Delta L_P$. Then after reaching the critical P/L, the pores were formed on the GUV and the volume of the vesicle increased thereafter. This is supposing that the pores had a finite size that allowed permeation of small molecules like glucose more than for large molecules like sucrose, which result in the vesicle volume increase. The decrease in the protrusion length ΔL_P was due to the volume increase at constant area: $\Delta V = \pi R_P(R_V\ R_P)\Delta L_P$. To keep the figure A2 simple, the same relation was used to indicate a decrease in ΔL_P by a decrease in ΔA. In fact, a negative ΔL_P is due to volume increase at constant area.

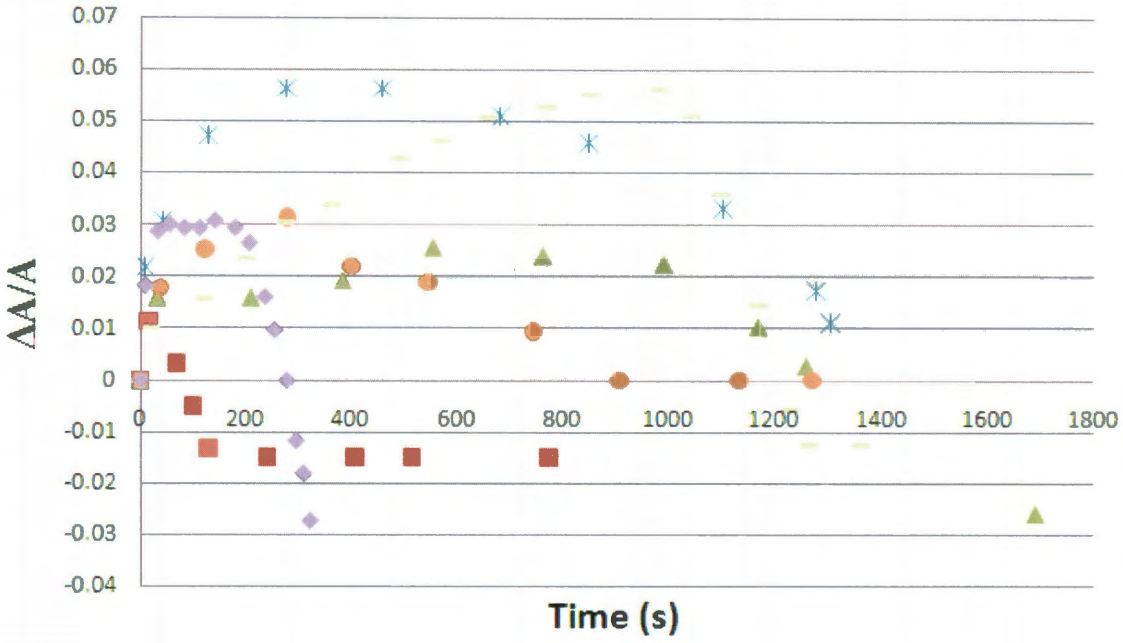

Figure A 2 Fractional area increase of GUV in time at 0.5μM BAX. To keep the figure simple, the same relation was used to indicate a decrease in ΔL_P by a decrease in ΔA.

Here, we should notice that without dialysis, the OG about 0.68mM was still in the BAX solution. OG below the CMC will not solubilize lipid bilayers but it will incorporate into the lipid bilayers. For this reason, the initial area increase of GUV was not only due to the binding of BAXs on bilayer interface but also due to the incorporation of OG into lipid bilayer. In order to calculate the real area change due to the binding of BAXs only, we did a control experiment. We used the same two chamber aspiration method, but there was no BAX protein in the observation chamber. We calculated the area change as a function of time when OG incorporated into the GUV (figure A3). We averaged over six independent experiment runs, and

calculate the average normalized area change as the function of time and named it $(\Delta A/A)_{background,t}$.

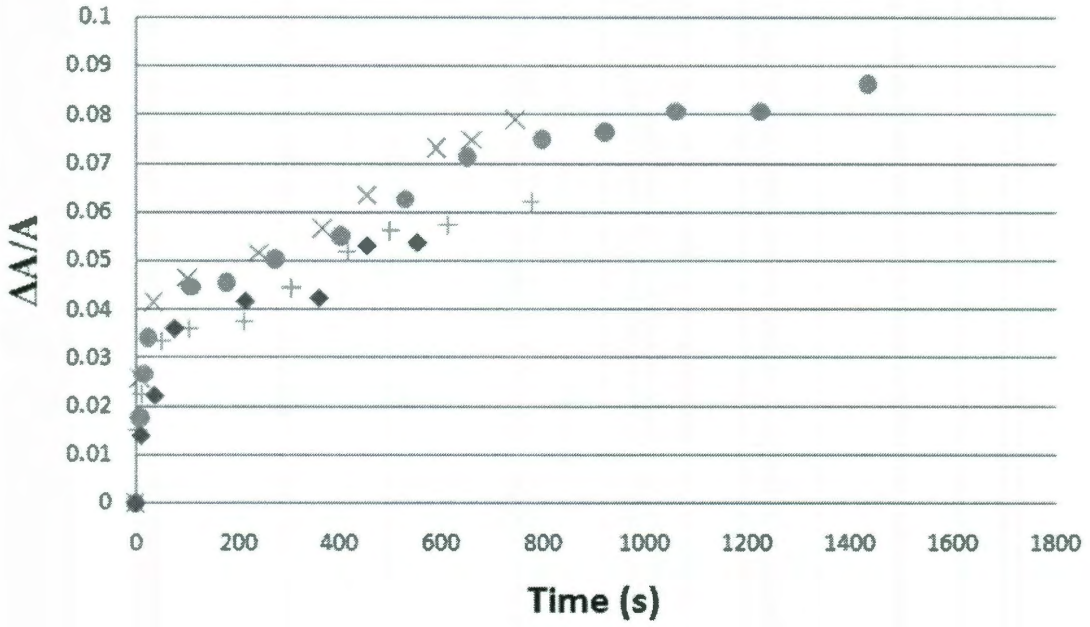

Figure A 3 Fractional area increase of GUV in time at 0.68mM

We were mainly interested in the $(\Delta A/A)_{max}$ when the concentration reached the critical P/L. So the last step was to calculate the $(\Delta A/A)_{max}$ in figure A2 and subtracted the $(\Delta A/A)_{background,t}$. The final result was shown in figure A4 were the effect of OG has been already taken out. The ΔA/A in this figure indicated the maximum area change due to the binding of BAXs on the bilayer interface before pore forming. For antimicrobial peptides the maximum fractional area expansion $(\Delta A/A)_{max}$ is typically ~4%. If our hypothesis were correct, pores by BAX should occur at much smaller $(\Delta A/A)_{max}$. Indeed, the values in figure A4 was much smaller

than 4% and the average of $(\Delta A/A)_{max}$ for ten independent runs gave the value ~-0.17%. However, the was no physical meaning for $(\Delta A/A)_{max}$ <0. Our explanation was that this negative value might be due to the large error of $(\Delta A/A)_{background,t}$. We estimate that there is a ~1-2% error in $\Delta A/A$ in typical GUV experiments. We believed that our result is consistent with the hypothesis that BAX proteins locally thinned the membrane and formed the pores in a relatively low P/L.

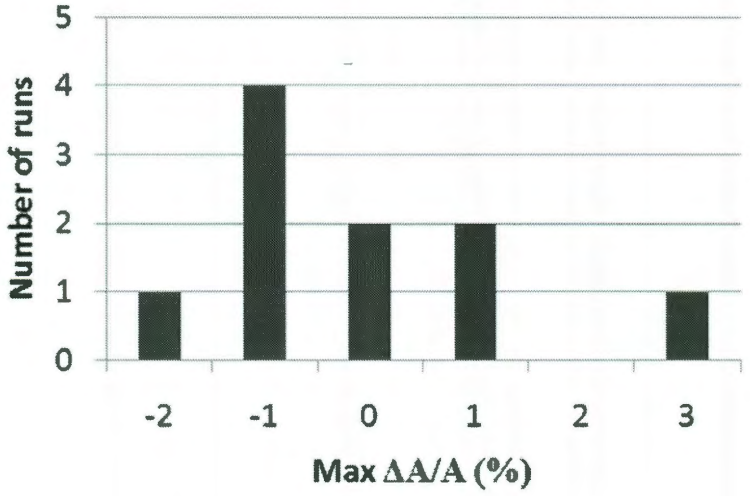

Figure A 4 Histograms for the maximum values of ΔA/A after taking out the influence of OG.

We believed that in order to measure $(\Delta A/A)_{max}$ accurately, OG should be removed from BAX solution after BAX being activated. We tried to dialyze the OG/BAX solution against the buffer solution overnight; however, after dialysis the BAXs didn't form pores anymore. Another tricky part in this experiment was that in order to keep the BAX activated, 50mM NaCl was needed in the buffer solution. However, when the finite size pore was formed on the GUV, the presence of small

size NaCl outside the GUV would cause a fast influx of water and ruptured the vesicle. For this reason, the success rate of GUV aspiration method was relatively low.

We found out that the activation of BAX was too hard to control so we suspended this project. However, we still wanted to prove our hypothesis about pore-forming proteins, so we tried another protein, i.e., Diphtheria Toxin Transmembrane domain. Diphtheria toxin (DT) is a 58-kDa protein secreted by Corynebacterium diphtheriae, the pathogen bacterium that causes diphtheria. The toxin, a single 535-residue polypeptides, can be split into two chains, N-terminal fragment (DTA, 21kDa) and C-terminal fragment (DTB, 37kDa), joined by a disulfide bond. The crystal structure of diphtheria toxin shows a Y-shaped molecule of three domains. The DTA chain is the catalytic (C) domain. The DTB chain contains the receptor biding (R) domain and tranmembrane (T) domain. The T domain (DTT) composed by nine α-helices, several of which are hydrophobic and play the role of membrane insertion and translocation. The innermost layer of DTT is a buried hydrophobic pair of helices, TH8 and TH9, which are most likely to form a transmembrane structure upon insertion into a bilayer. Alexandre Chenal et al. showed the pH-dependent membrane insertion of DTT domain in lipid bilayers. They showed that at pH 6 the native tertiary structure of the T domain unfolds and binds to the membrane. At pH 4, the N-terminal helices penetrate the headgroup region while C-terminal helices penetrate deeper into the acyl-chain region of the

bilayer, as shown in figure A5. We wish to understand the mechanism by which the DTT forms the transmembrane pore.

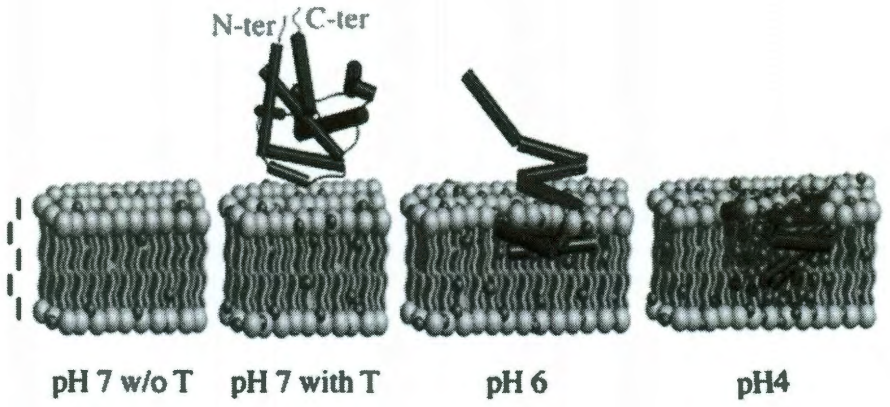

Figure A 5 Scheme of the pH-dependentmembrane-insertion process of the DT T domain. From left to right: membrane at pH 7 in the absence of T, membrane at the same pH in the presence of T, themembrane-bound state of T at pH 6, and the membrane-inserted state of T at pH 4. (from Chenal et al. 2009, *J. Mol. Biol.* 391, 872–883)

In order to activate the DTT domain, we designed a three chamber aspiration method based on the idea of the previous Alexandre Chenal et al. study. The DTT used in this experiment was supplied by our collaborator Dr. John Collier of Harvard Medical School. The GUV suspension was injected into the first chamber which contained pH 7 buffer solution. A chosen GUV was aspirated by a micropipette and was transferred into the second chamber which contained 0.8 μM DTT protein in pH 6 buffer. The GUV was exposed to this solution for about 3 mins to allow DTT to bind onto the bilayer and then was transferred into a third chamber. The pH was lower to

4 in the third chamber so that the DTT could penetrate into the bilayer. The experiment setup is shown in figure A6.

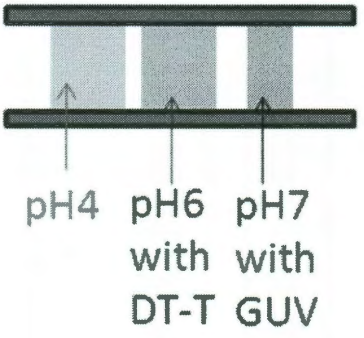

Figure A 6 Schematic of the three chamber GUV experiment. The first chamber contained GUV suspension in pH 7 HEPES buffer. The second chamber contained activated DTT in pH6 buffer. The third chamber contained pH 4 buffer.

Our result showed that in the second chamber (pH=6) the DTT indeed bound onto the interface of the lipid bilayer and cause the area increase (figure A7). Upon exposing to the pH 4 buffer in the third chamber, the DTT penetrated deeper into the bilayer and caused a further increase in membrane area. After reaching the maximum ($\Delta A/A$), the pores were formed and then the volume of the GUV increased. However, about 90% of the GUVs ruptured within several seconds after transferring into the pH 4 buffer chamber. Thus, the success rate was very low. In order to understand what caused the GUV rupture, we did the control experiment in low pH buffer without any protein. We found that even without protein, the GUV ruptured in pH 4 buffer. The GUV adhered onto each other when pH was lower than 5. This phenomenon inspired us to measure the adhesion energy induced by low pH (result